**Scuola Internazionale Superiore di Studi Avanzati**

# The spontaneous activity of organotypic and dissociated neuronal networks

Neuroscience area

Ph. D. course in Neurobiology

September 2018

Author

Diletta Pozzi

Supervisor

Prof. Vincent Torre

SISSA – via Bonomea 265 – 34136 Trieste (TS) - Italy

*I do not think there is any thrill that can go through the human heart like that felt by the inventor as he sees some creation of the brain unfolding to success... such emotions make a man forget food, sleep, friends, love, everything.*

Nikola Tesla

**Acknowledgements**

I would like to thank my supervisor, Prof. Vincent Torre, who inspired me to think beyond the limits and encouraged me to follow my dreams.
Thanks to all my lab members, the ones who already left and the ones who just arrived, for the fruitful discussions we had and the moral support. In particular, thanks to Francesco, Ulisse, Fiamma, Nicola, Simone, Miao, Qin, Renza, Xiaoyun, Fabio. A special thanks to Dr. Jelena Ban for the work we did together and the mentoring. Thanks to Manuela Schipizza for the language editing on my manuscripts and useful advices.
A special thanks to Prof. Yong Chen for giving me the opportunity to work in his team - and experience the magic of Paris - for two months.
Then I would like to thank the technicians and administrative assistants of SISSA, who often gave me practical help and have always been friendly: you contributed to make my experience in SISSA so great and productive! Thanks to Beatrice, Tullio, Jessica and Micaela.
To all the friends I met in SISSA during these years: I will always remember the experiences we shared. You and our beloved Trieste now occupy a special place in my hearth. Thanks especially to Nora, Xuan, Katarina, Kevin, Tiago, Abraham and other members of our international “family”.
Finally, thanks to my weird but lovely family: your constant presence along the years gave me the strength to move on no matter the difficulties and emotional cost of pursuing science, which can be at the same time the best and the worst job in the word. But for today, let’s assume it is the best…and I believe it!

**Table of Contents**

# 1. Abstract

In the absence of external stimuli, the nervous system exhibits a spontaneous electrical activity whose functions are not fully understood, and that represents the background noise of brain operations. *In vitro* models have long represented a simple and useful tool for studying the basic properties of neurons and networks. This study provides a detailed characterization of spontaneous activity of neuronal networks in different *in vitro* models. In particular, it clarifies the role of the extra-cellular environment and of the intrinsic architecture in shaping the spontaneous activity of networks by means of calcium imaging techniques. The results presented within this study come from three experimental works, each one addressing a particular feature of the network model:

- Chemical composition of the extra-cellular environment: a comparison of dissociated hippocampal cultures grown in three different culturing media revealed that the use of an astrocyte-conditioned medium improves significantly the frequency and synchronization of neuronal signaling.
- Mechanical and topographical properties of the extra-cellular environment: the design of a hybrid micro-nano substrate for dissociated hippocampal cultures revealed that nano-scaled patterns provide an improved artificial extra-cellular matrix for obtaining neuronal networks with a frequent spontaneous signaling.
- Network architecture: synchronized events called Global Up states - involving the totality of neurons in the network - are observed in both organotypic and dissociated neurons; the duration of Global Up states increases by increasing the complexity of the network, while their frequency decreases. Simulations with simplified models of single- and multilayered networks confirm the experimental data.

Taken together, these results show that the spontaneous synchronous activity of neurons is a result of their intrinsic biophysical properties, arising also after disruption of the original network architecture. However, dissociated neurons show different levels of synchrony depending on the chemical and topographical composition of the surrounding artificial extra-cellular matrix. Moreover, the specific architecture of the network and its single- or multilayered composition has an influence on the frequency and duration of spontaneous events, suggesting a potential explanation for the diversity of oscillatory rhythms observed in the brain.

# 2. Introduction

The first part of this introduction presents the main patterns of spontaneous activity observed *in vivo* in cortical and hippocampal networks, together with the current hypotheses on its functional role(s) during development and adulthood. Next, a summary of the main types of *in vitro* models and of the spontaneous activity that they exhibit is presented. The effectiveness of any cellular *in vitro* model is given by its ability to reproduce an *in vivo* – like phenotype, both at the morphological and at the functional level. Neuronal cell types, in particular, need a substrate where to attach in order to grow and survive. The substrate represents then a crucial factor interacting with neurons at the level of membrane structures, aimed at mimicking the extra-cellular matrix of the brain. For this purpose, several approaches have been adopted, from traditional two-dimensional substrates to the more advanced three-dimensional neuroscaffolds. Another type of three-dimensional *in vitro* model is represented by explanted brain slices, which maintain the original cyto-architectural organization of the tissues. The similarity of these models with the corresponding spontaneous brain rhythms is

discussed within each section. Finally, an overview of the results obtained within my doctoral studies using different types of *in vitro* models is presented.

### *2.1 Spontaneous activity of neuronal networks – Current hypotheses and in vivo studies*

Even though the phenomenon had previously been observed, a first characterization of neuronal spontaneous activity was provided by Steriade et al. in a series of three works published in 1993[1]. Measuring the electrical activity of cortical and thalamic neurons in anesthetized cats, they observed the occurrence of some periodic oscillations. These oscillations were composed of a slow (0.8 – 1.5 s) depolarizing phase followed by a long-lasting hyperpolarization, and had a low frequency (less than 1 Hz). The duration of the depolarizing phase was reduced by administration of the NMDA blocker ketamine.

Subsequent studies confirmed and deepened the characterization of spontaneous cortical slow oscillations, and named Up and Down states the depolarizing and hyperpolarizing phase of the oscillation, respectively. Constantinople and Bruno (2011)[2] showed that this dynamical switch between a depolarized and a hyperpolarized membrane potential state, visible in the barrel cortex of rats under anesthesia, was eliminated during wakefulness when a persistent depolarization was instead observed (**Fig. 1**). In addition, they showed that the dynamics of the awake state and under anesthesia were unaltered even after elimination of afferent thalamic input, suggesting an internal cortical neuromodulation. In fact, the large majority of excitatory synapses onto cortical excitatory neurons come from other cortical excitatory neurons[3], giving the cortex a vast recurrent connectivity.

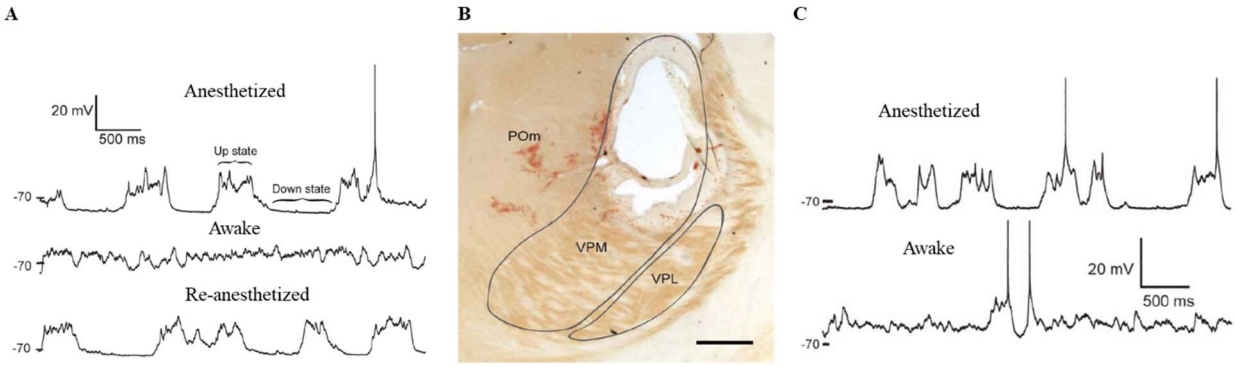


**Fig. 1**. **Spontaneous slow oscillations in the cortex of anesthetized and awake rats. (A)** *In vivo* whole-cell recording of a L2/3 pyramidal neuron while the rat was anesthetized (top), awake (middle) and re-anesthetized (bottom). In the first case, the membrane potential oscillates between Up and Down states, while during wakefulness the periods of synaptic quiescence are abolished. **(B)** Coronal section showing a lesion in the ventroposterior medial nucleus (VPM) of the thalamus, centered on the C2 barreloid projecting to the cortex. POm, posterior medial nucleus; VPL, ventrolateral nucleus. Scale bar, 500 µm. **(C)** Whole-cell recording of a pyramidal neuron in L4 following the lesion shown in (B): the thalamus is not required for producing slow oscillations nor an awake membrane potential. From Ref. 2.

Slow oscillations in the cortex exist also at the network level, in the form of synchronized alternations between Up and Down states. In this case, they are referred to as slow waves and have been observed at multiple scales: from human EEG data[4] to *in vitro* brain slices isolated from the rest of the brain (see section 2.4 on explanted cultures). Since they arise in such different systems, Up and Down states have been proposed to be a default activity pattern resulting from the basic architecture of the network. Nevertheless, they may still have a functional role. From experimental observations of their pathways, Up and Down states are supposed to transfer information across structures and to consolidate memories. A current hypothesis is that cortical Up states travel through the enthorinal cortex to the hippocampus phasing the hippocampal rhythm, which in turn transfers its activity pattern

- acquired during learning - back to the cortical networks for memory consolidation[5]. Down states, on the other side, are thought as a period necessary for metabolic restoration (see for review[53]).
Spontaneous oscillations in developing neuronal networks have been observed as well. An example is represented by synchronous plateau assemblies (SPAs) and giant depolarizing potentials (GDPs) in the immature hippocampus. Driven by a network of synchronized, GABAergic neurons, GDPs are thought to shape synaptic currents in the immature network[6,7].
Neuronal oscillations in the mature hippocampus instead have been observed mainly in the theta-frequency range (i.e. 4-8 Hz). Hippocampal theta waves are generated mainly by the entorhinal input and by CA3 collaterals, through the activation of voltage-dependent $Ca^{2+}$ currents in pyramidal cells. GABAergic and cholinergic neurons contribute as well to the generation of theta waves by feed-forward disinhibition of CA1 pyramidal cells by the interneurons, and cholinergic activation of CA3. The theta rhythm is believed to be critical for temporal coding/decoding of active neuronal ensembles and the modification of synaptic weights[8].
The rhythmic inhibitory activity of interneurons, in particular, plays a key role in the maintenance of brain oscillations: interneurons were proven to synchronize the spiking of hippocampal pyramidal cells, thus maintaining homeostatic levels of activity in the brain[9]. Moreover, local field potentials measured in human and monkey were proven to be composed by inhibitory neurons for the largest part, suggesting that the onset of Up states is more driven by a decrease in inhibition rather than an increase in excitation[10].

### *2.2 "Traditional" dissociated cultures – Methods, applications and spontaneous activity*

Neurons preserve the ability to generate spontaneous electrical pulses even when disrupted from their original connectivity and cultured *in vitro*. In fact, primary dissociated cultures, obtained from embryonic or postnatal rodent brain regions such as the hippocampus or the cortex, represent a well-established *in vitro* model for studying neuronal networks, both on a short (network formation) and a long term (differentiation, maturation) scales[11,12]. When cells are enzymatically dissociated, plated on suitable substrates and cultured in appropriate media, they grow processes and form *ex-novo* a functional network. Dissociated cell cultures are traditionally plated on glass-made flat surfaces, allowing a fine single-cell resolution and a detailed morphological investigation of small cellular structures like growth cones. Neurons attach to surfaces through their anionic phospholipids (e.g. phosphatidylserine)[13], therefore the surface needs to be positively charged. Previous coating with polyaminoacids such as polylysine and polyornithine have since long been used for this purpose, together with the addition of components (i.e. Matrigel®[14]) mimicking the extracellular matrix *in situ*. The morphology and development of individual dissociated neurons as well as their network activity are strongly influenced by the culturing conditions and, in particular, the culturing medium used[15,16]. Different chemical composition have been tested and are commercially available for neuronal cell cultures, all based on a physiological solution added with a particular supplier of nutrients and growth factors. Fetal Bovine Serum (FBS), for example, provides neurons with sufficient factors for short-term cultures. As any animal-derived product, however, it is prone to batch-to-batch variability[17] and, most of all, it results in a low differentiation of neuronal types[18]. For this reason, serum-free media were tested with different additives. A very commonly used one is B27 Supplement ®, aimed at obtaining almost pure neuronal cultures[19]. Another option is to use glial cells, specifically astrocytes, as intrinsic source of growth factor in the neuronal culture. In fact, it is possible to plate neurons on a glial feeder layer[20] or, in order to avoid the spatial interference of astrocytes while maintaining the soluble factors released by them, to grow neurons in an astrocyte-conditioned medium (ACM)[15]. ACM is supposed to contain lipids, thrombospondins and Brain Derived Neurotrophic Factor (BDNF), that are essential components for neuronal growth and

survival[21]. A detailed comparison of these three methods for growing neurons is provided in the **Results** part (Pozzi et al. 2017).

Once established the optimal plating and growing conditions for the specific experimental purposes, it is possible to explore the properties of dissociated networks with a fine, single cell resolution. A common application is to analyze different neuronal populations transgenically labeled with fluorescent proteins. In the GAD67-GFP mouse line, for example, the main class of inhibitory neurons (i.e. GABAergic neurons) is labeled in green by use of the Green Fluorescent protein (GFP)[22]. A comparison of spike parameters between GABAergic and glutamatergic neurons has been possible, in fact, because of the optical identification of these cells[23] (**Fig. 2D**).

Network (i.e. synchronized) activity in dissociated networks emerges at 3-7 days in-vitro (DIV) and matures over the following several weeks in culture, as shown by electrophysiological and imaging measurements[20,24]. Synchronized neuronal activity has been proven to be mediated by the NMDA-R, by serotonin and acetylcholine[25]. Network activity is also strongly dependent on the initial plating density of neurons: neurons plated at high density present higher rates of less synchronized activity comparing to sparse networks[20,26]. In fact, there is an inverse relationship between the density of the network and its synaptic strength, such as sparse neurons establish less but stronger synaptic connections, as shown also by the longer duration of their bursts (see **Fig. 2A-C**).

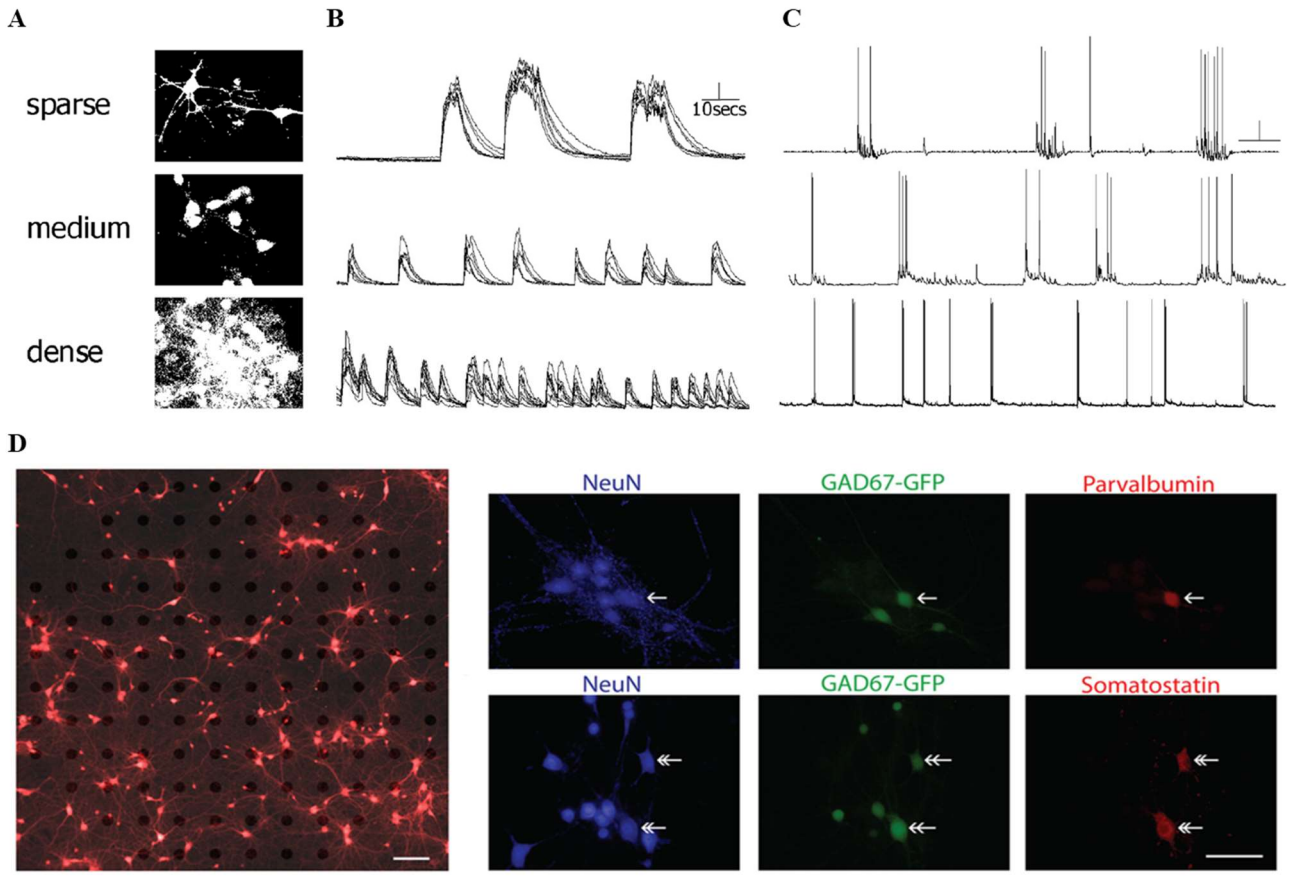


**Figure 2. Spontaneous activity in dissociated neuronal cultures. (A)** Dissociated neurons plated at different densities loaded with the calcium-sensitive indicator Fluo-4. **(B)** Corresponding optical traces. Sparse cultures exhibit less frequent but longer synchronous bursts. Scale bar: 1 arbitrary fluorescence unit. **(C)** Corresponding current-clump recordings in the three culture conditions. Scale bar: 20 mV, 5 s. **(D)** Overlay of bright field and fluorescence images of neurons plated on a 120-channel MEA and recorded at DIV14. Staining: calcein red-orange. Scale bar: 100 µm. **(E)** Immunocytochemistry using the neuronal marker NeuN (blue) and the markers for interneurons Parvalbumin and Somatostatin (red) confirms that the genetically labeled GAD67-GFP cells (green) are inhibitory interneurons. Scale bar, 50 µm. From Ref. 20, 23.

*2.3 Dissociated cultures on neuroscaffolds – Methods, applications and spontaneous activity*

Neurons cultured on traditional glass coverslips are prone to artifacts due to the two-dimensional, flat condition in which they grow. In fact, glass coverslips are distant from the physiological extra-cellular environment of the brain, which is three-dimensional and soft (less than 1 kPa in Young modulus, while the stiffness of the glass is in the order of GPa). Specifically, neurites forced to grow in a planar region present abnormal excitability[27]. Moreover, the differentiation of stem cells can be directed towards bone, muscle and neuronal cell types by progressively decreasing the stiffness of the substrate[28]. For these reasons, three-dimensional (3D) substrates with appropriate stiffness were developed for neuronal cultures, and called neuroscaffolds. An interesting example is represented by carbon based neuroscaffolds, engineered for interfacing the cell membrane structures. Carbon based materials have since long raised the interest of neuroscientists because of the electrical conductivity of the material, that might find its most obvious application in restoring/improving neuronal connectivity[29,30]. These materials can be assembled in the form of wrapped graphite sheets, and therefore called carbon nanotubes (CNTs), or in the form of graphene foams. Both cases were proven to be biocompatible and conductive scaffolds not only for culturing primary neurons, but also for neural stem cells differentiation[31,32] (**Fig. 3A-D**).

Moreover, primary hippocampal neurons plated on 3D graphene showed a more frequent and synchronized spontaneous activity comparing to both 2D graphene and traditional 2D glass substrates (**Fig. 3E-F**), revealing a specific role of dimensionality in the network dynamics[33].

CNTs as well were proven to boost the synaptic activity of dissociated neurons[34]. Moreover, when implanted in rodent models of spinal cord injury in order to bridge the segregated spinal segments, they showed a good biocompatibility as demonstrated by measurements of glia reactivity around the implanted material[35] (**Fig. 3G**).

Polydimethylsiloxane (PDMS) and other plastic materials represent another interesting category for neuronal studies: while not electrically conductive, these materials have the advantage of being highly ductile and with a Young modulus closer to the one of brain tissues. The fabrication of these type of scaffolds usually requires photolithography techniques combined with micro/nano-patterning[36,37]. Plastic micropillars have often been used as substrates for cell cultures in order to decrease the stiffness of the original material: while a flat surface of PDMS has a Young modulus of around 1 MPa, PDMS micropillars have a stiffness of 5-20 kPa depending on their diameter and height[38]. For these reasons, micropillars are useful for determining the mechanical responses and forces exerted by cells[39]. Plastic materials can also be molded at the nanoscale: the use of nanopillars with different dimensions and stiffness has been proven to control the adhesion and differentiation of neuronal precursors[40]. Moreover, PDMS-based microchannel electrodes have successfully been implanted in rodents for monitoring neural activity over time and for providing a mechanical support for peripheral nerve regeneration[41] (**Fig. 3H-L**).

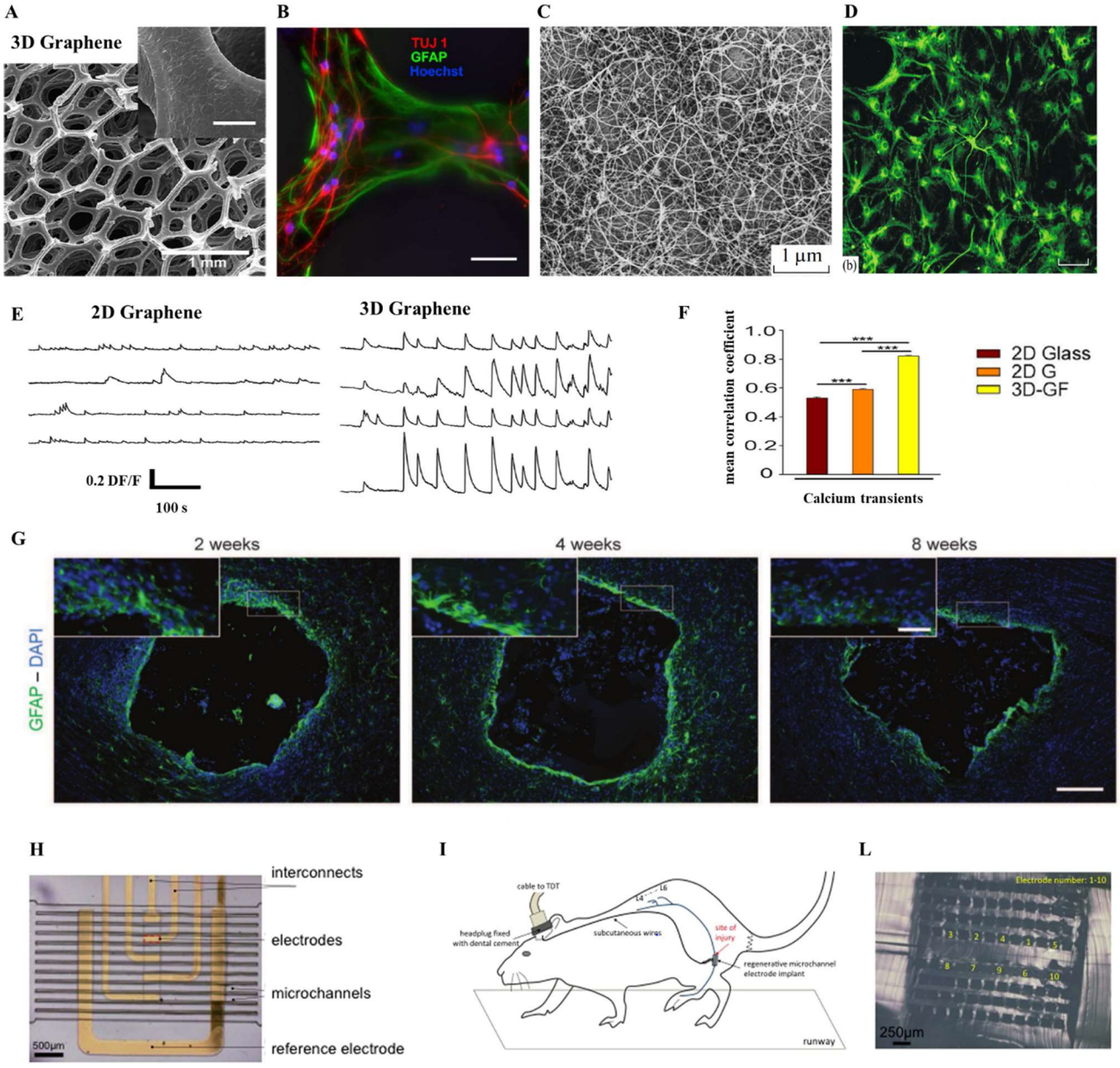


**Figure 3. Neuroscaffolds for culturing mature neurons, differentiating neuronal precursors and for *in vivo* implants. (A)** SEM image of a scaffold consisting of a porous graphene foam synthesized by chemical vapor deposition method using a metallic template. Enlarged image in the inset (scale bar, 50 µm). **(B)** Fluorescent image of the scaffold in (A), with primary hippocampal neurons and astrocytes after 7 days in culture stained with the neuronal marker β-tubulin III (TUJ1, red), the astrocytic marker glial fibrillary acidic protein (GFAP, green) and Hoechst nuclear staining (blue). Scale bar, 50 µm. **(C)** SEM image of carbon nanotubes (CNTs) films coated on quartz glasses. **(D)** Mouse neural stem cells plated on the CNTs films shown in (C), stained with TUJ1 (green). Sacle bar, 100 µm. **(E)** Calcium transients from selected neurons plated on 2D (right) and 3D (left) graphene substrates. **(F)** Mean correlation coefficient of the calcium transients shown in (E) compared with the one measured on neurons plated on traditional 2D-glass (***$p < 0.001$ ANOVA on ranks, Domm's post-hoc test). **(G)** GFAP – positive astrocytes (green) stained in the cortex surrounding the CNTs implants at 2, 4 and 8 weeks post – implantation (DAPI for nuclei is in blue). Levels of glial reactivity decrease over time. Sacle bar, 200 and 50 µm (inset). **(H)** Matrix of PDMS microchannels with integrated gold thin-film electrodes for *in vivo* sciatic implant and neuronal recordings. **(I)** Schematic of the experimental setup with the regenerative microchannel electrode implant shown in (E). The sciatic nerve was previously sectioned. The electrode implant was then placed between the nerve stumps to support axon regeneration, and connected to wires leading to a headplug for the recording of neural activity. **(L)** Cross-sectional photograph of the regenerative PDMS microchannel array highlighting the ten channels hosting the electrodes. From Ref. 32, 33, 35, 41.

*2.4 Explanted brain slices – Methods, applications and spontaneous activity*

Intact tissues from the central and peripheral nervous system can be isolated and either freshly used or cultured *in vitro*. These preparations represent a 3D *in vitro* model aimed at retaining the native cyto-architecture of the original tissues. Slices of brain or spinal cord can be isolated from the region of interest and directly used for electrophysiological and imaging measurements[42,43]: in this case, they are referred to as acute slices. Acute slices underwent the cutting of several neurites during the preparation, resulting in an altered network activity comparing to the native conditions. However, acute cortical slices are able to reproduce the most characteristic feature of the cerebral cortex, i.e. slow oscillations between Up and Down states, as shown by the work of Sanchez-Vives starting from the 2000s[44–46]. In this work, intracellular recordings from ferret visual and prefrontal cortical slices were performed. While no spontaneous activity was recorded in the "traditional" slice bathing medium (2 mM $Ca^{++}$, 1 mM $Mg^{++}$, 2.5 mM $K^{++}$), some rythmic oscillations were observed after changing the bath solution to a composition more similar to the brain interstitial fluid (1.0 or 1.2 mM $Ca^{2+}$, 1 mM $Mg^{2+}$ and 3.5 mM $K^{+}$). These oscillations were initiated by pyramidal neurons of layer V, had a periodicity of once every 3.5 s and were stable for the life of the slice (12 h). The cortical slices were prepared from 3 to 8-months-old ferrets, i.e. adult stage, and showed a close similarity to those previously observed in adult, anesthetized cats[1] (**Fig. 4**). In fact, the spontaneous activity of slices was studied as the most likely *in vitro* equivalent of the activity of the brain in the absence of external stimuli, i.e. during quiescent sleep or under anesthesia.

Slices of tissue cultured *in vitro* for several days are instead referred to as organotypic slice cultures: they were proven to regrow synaptic processes and to restore the functions potentially impaired during the cutting procedure. Specifically, the firing rates and the excitatory synaptic activity in the *in vivo* hippocampus were found to be more similar to those in slice cultures compared to acute slices[47]. In fact, slice cultures were used as a robust model to chronically monitor the switch between subsequent developmental processes in the hippocampus, such as SPAs and GDPs[48].

Without the technical issues presented by in vivo measurements (i.e. background noise, the interference of anesthetics), experiments on slices have been useful to address questions like how inhibitory neurons coordinate synchrony: the hyperpolarizing effect of one individual GABAergic neuron in slices of isolated hippocampus was proven to tune the spontaneous firing of pyramidal neurons at theta frequencies[49]. Similarly, an electrophysiological and morphological characterization of layer V neurons in cortical slices showed that inhibitory, fast-spiking neurons coordinate the synchronous firing of excitatory pyramidal neurons through their dense electrical coupling[50]. These results are in line with subsequent studies in behaving mice, thanks to the advances in two-photon microscopy, characterizing the membrane potential dynamics of fast-spiking inhibitory neurons vs excitatory ones[51].

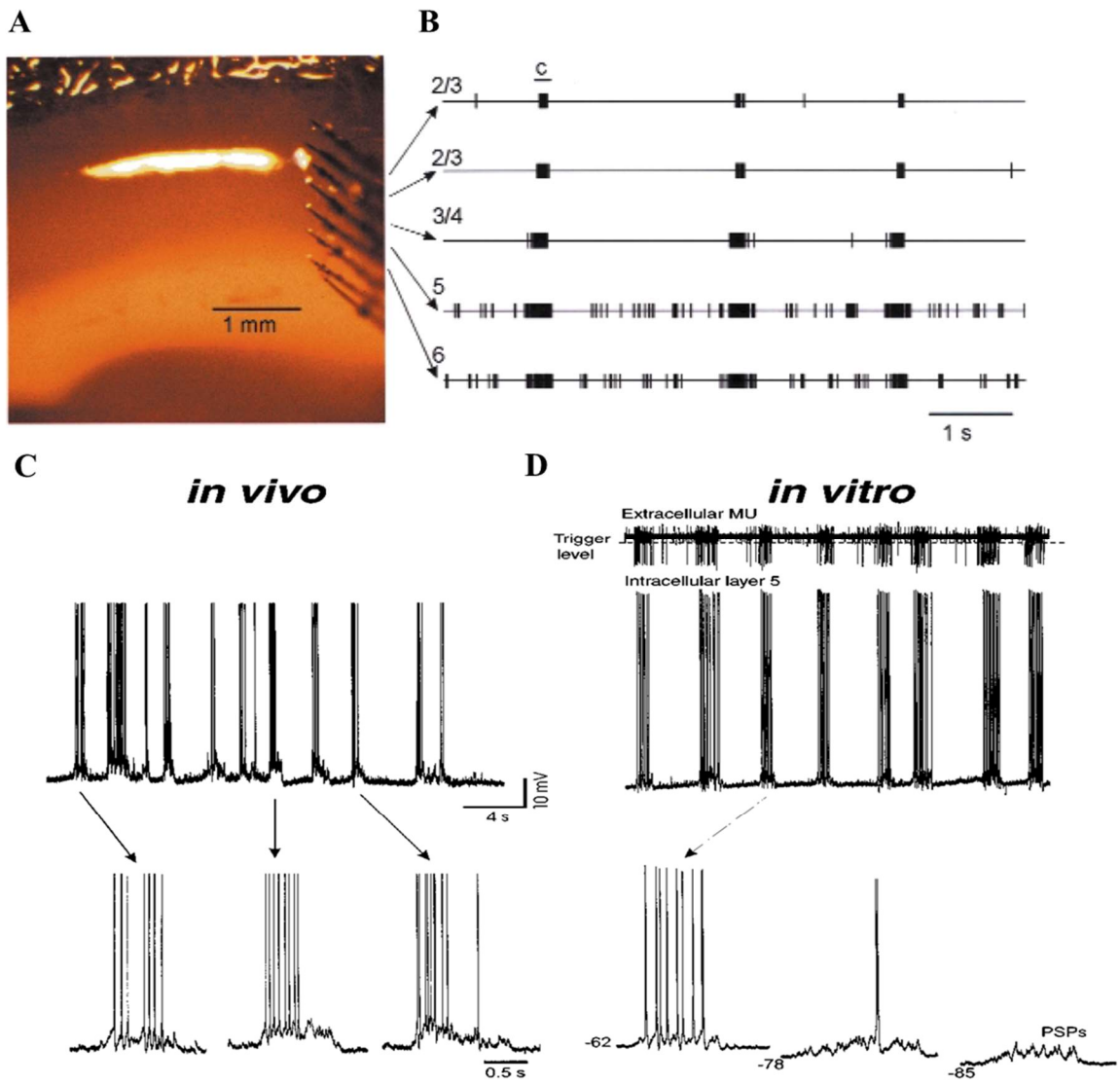


**Figure 4. Spontaneous slow oscillations in cortical slices. (A)** Extracellular recording microelectrode array placed vertically in a slice of ferret neocortex. **(B)** Simultaneous multiple-unit recording from cortical layer 2/3 to 6 reveals slow oscillations initiating from around layer 5, followed, on average, by activity in layers 6 and 3/4. **(C)** Intracellular recording from the visual cortex of an adult, anesthetized cat, revealing a rhythmic sequence of depolarized and hyperpolarized membrane potentials; three depolarizing sequences are shown in the expansion for clarity. **(D)** Simultaneous extracellular and intracellular recording of a visual cortical slice maintained *in vitro*. The intracellular recording is from a layer 5 intrinsically bursting neuron. The depolarized states at three different membrane potentials are shown in the expansion. Note the similarity between the recordings in (C) and (D). From Ref. 44.

### *2.5 Overview of the results obtained*

The first project presented within this dissertation (see **Results and Methods**, Pozzi et al. 2017) aims at obtaining a simple yet solid and reproducible *in vitro* model of dissociated neuronal network for both short-term and long-term experimental studies. This work demonstrates that the soluble factors used as growing media significantly affect the morphology and the network activity of dissociated hippocampal neurons. A detailed morphometric and functional comparison of neuronal cultures grown in three different conditions shows that a serum-free, astrocyte-conditioned medium (ACM) is the optimal protocol for obtaining viable neurons up to three months in culture. Neurons grown in ACM showed an increased area of axonal growth cones, together with a higher number of filopodia per growth cone and an increased neuronal arborization comparing to other two traditional protocols.

ACM supported the survival of a controlled percentage of astrocytes in the culture that were shown to have a more complex and *in vivo* - like morphology[52] comparing to the other two methods, especially with the serum-enriched medium (**Fig. 5**). Astrocytes grown in the presence of serum, in fact, develop an artefactual, fibroblast-like morphology[18,53]. Moreover, the network activity was found to be more frequent and synchronized in ACM comparing to both FBS and B27 – based media at all time points considered (i.e. after 7 and 14 days). The increased degree of synchronization observed in ACM was stable over the entire lifespan of the neuronal culture. Moreover, neurons grown in ACM showed the longest survival (i.e. three months, data not published). Therefore, traditional dissociated cultures grown in optimal conditions might reproduce a mature morphological phenotype and, if plated at sufficient density, a stable spontaneous activity pattern. For this reasons, these type of neuronal cultures might be useful for chronic electrophysiological recordings on microelectrode arrays, and for chronic pharmacological studies.

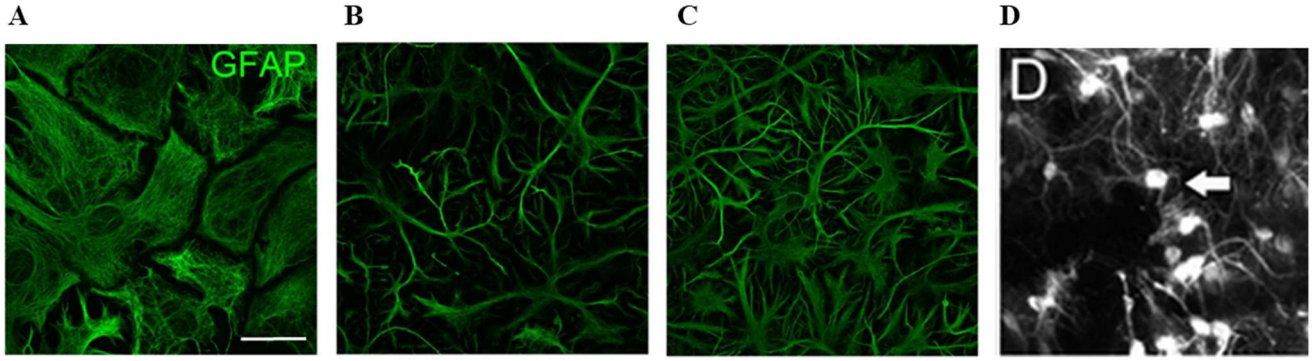


**Figure 5. Morphology of astrocytes in different conditions**. Cells are stained for the astrocytic marker Glial Fibrillar Acidic protein GFAP after 7 days in culture. **(A)** Astrocytes grown in a serum-enriched medium. **(B)** Astrocytes grown in a B27-supplemented medium. (C) Astrocytes grown in ACM. Scale bar, 50 µm . **(D)** Cortical astrocytes from *in vivo* two-photon imaging (from Ref. 52). Panels **A-C** represent the data from the work discussed within this section (Ref. 16).

The second work presented within this dissertation (see **Results and Methods**, Wei et al. 2017) investigates the effect of the substrate, which acts as an artificial extra-cellular matrix, in shaping the morphology and spontaneous activity of the neurons attached. In particular, some topographical cues at both the micro- and nanoscale order were added to the surface by means of microengineering techniques. The new hybrid micro/nanosubstrate was tested for neuronal cultures studies (i.e. imaging applications). In particular, the contribution of the nanofibers' coating of the substrate on neuronal growth and functionality was investigated by comparison with a similar substrate composed by the micro-patterned component only. The addition of a nanopatterned component on the substrate significantly improved neuronal attachment and increased the frequency of calcium transients. Moreover, astrocytes grown on nanofibers showed a more complex morphological phenotype comparing to the ones grown on micropillars only, in a way similar to astrocytes grown in different culturing media (compare **Fig. 5** and **6a, b**). Interestingly, neurons plated on micropillars only had more synchronized activity comparing to the ones plated on the micro/nanopattern after 14 days *in vitro*. In fact, different topologies of the substrate might affect synaptic densities and excitability of single neurons. The decreased synchrony observed in the micro/nanopattern is similar to the one observed in graphene 3D scaffolds when comparing 1 and 2 weeks *in vitro*[33]. This previous work interprets a decrease in synchronization over time as a similarity with the stages of development of *in vivo* networks[54]. The functional properties of neurons plated on the hybrid micro/nanopattern, together with the improved morphology of glial cells, suggest as well a more complex and developed neuro-glia network.

In conclusion, these results are in line with previous studies showing that nanopatterning of PDMS substrates improves the adhesion and differentiation of neuronal precursors comparing to flat PDMS

surfaces[40] (see **Fig. 6c, d**). Moreover, cell membranes present several molecular cues in the order of nanometers, therefore are more likely to interact with a substrate with a nanoscaled pattern.

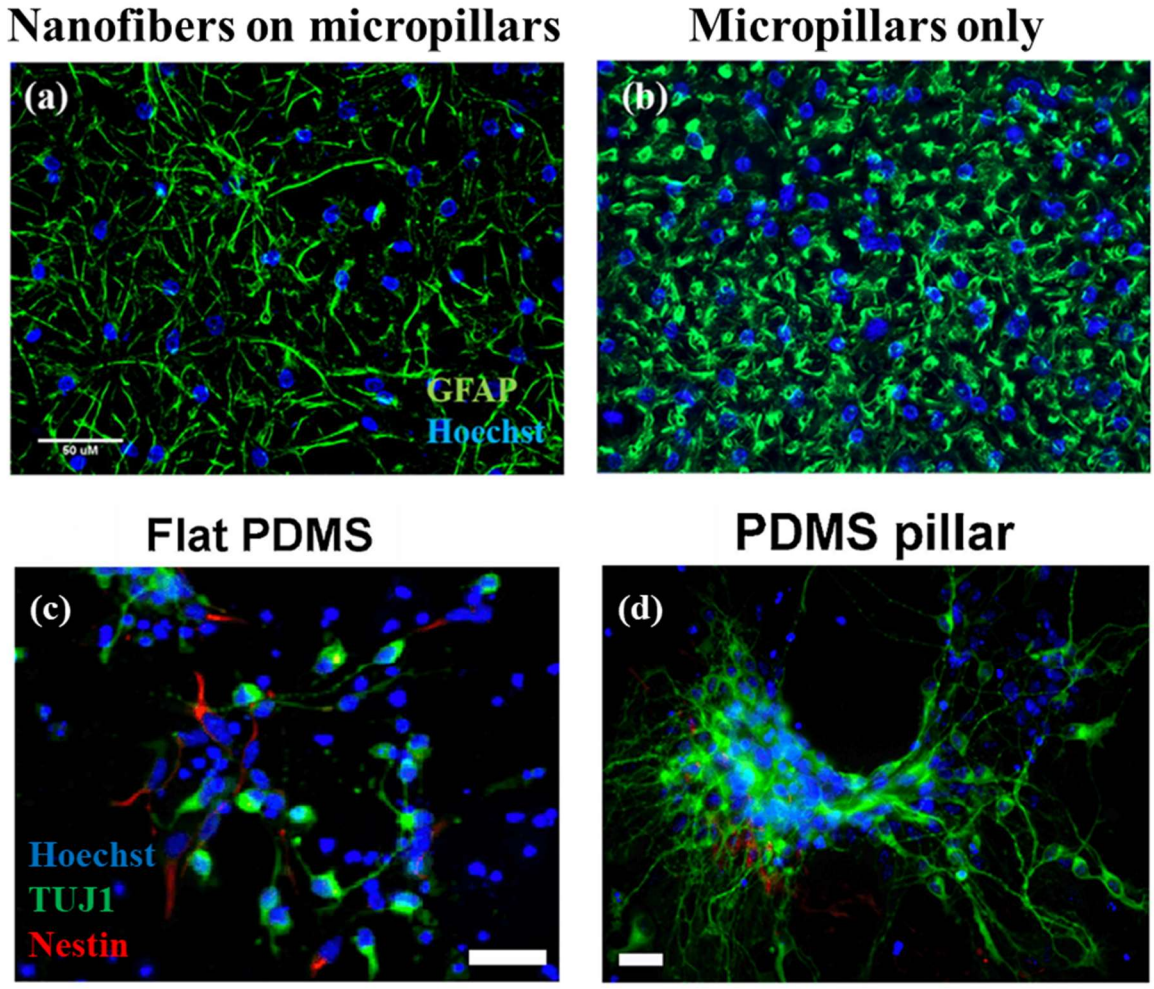


**Figure 6. Morphology of astrocytes and neurons in nanopatterned vs micropatterned and flat surfaces.** Astrocytes grown for 2 weeks on micropillar PDMS arrays, coated with nanofibers **(a)** and not coated **(b)**, stained with GFAP (green) and the nuclear marker Hoechst (blue). Neuronal precursors after 48 hours of differentiation on a flat PDMS surface **(c)** and on PDMS nanopillars **(d)**: TUJ1 (green) is a marker for differentiated neurons, while Nestin (red) is a marker for neuronal precursors. Scale bars, 20 µm. From Ref. 40 (c, d). Panels **a-b** represent data from the work discussed within this section (Ref. 37).

The last work presented within this dissertation (see **Results and Methods**, Pozzi et al. 2018, submitted) investigates the role of network architecture in shaping neuronal spontaneous activity. The architecture (or cyto-architecture) that this work refers to is the peculiar topology of different cell types and their connectivity in the network. Calcium imaging on cortical and hippocampal brain slices from GAD67-GFP mice revealed an intermittency between silent periods, periods of sparse and uncorrelated activity and periods of maximum synchronized activity. These three regimes of activity were called Down, Up and Global Up states within this work, as their duration and frequency coincided with the ones described from electrophysiological and imaging measurements *in vivo* and *in vitro*[1,42,44] (**Fig. 7A-C**). The size and duration of Up states in cortical and hippocampal slices followed a power law distribution with resonances coincident with Global Up states. The power law distribution of neuronal avalanches has been previously described as an expression of Self Organized

Criticality (SOC)[55]; however, this theory assumes that the events observed are rare. In my experiments, tens of events are simultaneously recorded; therefore, SOC does not explain their power law distributions.
The duration of Global Up states was measured from optical traces taking into account also the decay phase of the calcium transients; therefore, this measurement is overestimated to the same extent in all recordings. Global Up states showed a longer duration and a lower frequency in cortical slices comparing to hippocampal slices, suggesting a more complex anatomical multilayer organization in the cortex. Simulations with multilayered neuronal networks tested and confirmed this hypothesis. Three simplified models of neuronal networks were developed by my collaborators in order to reproduce the experimental data, each one consisting of very few (3/4) parameters. While the number of neurons in each layer of the network was fixed, the number of connecting neurons, the degree of dissipation (that is intended as a simplified form of inhibition), the firing threshold and the strength of connectivity followed long-tailed distributions in accordance with experimental evidence[56]. These models were able to reproduce the power law distribution of Up states and the resonances corresponding to Global Up states at different degrees (we obtained more visible resonances form Model 1, where the firing neuron distributes all its charge randomly among its NC neighbours).
The traditional, epifluorescence microscopy used for calcium imaging represents a limit of this study: in fact, given the thickness of brain slices, some out – of – focus light interfered with the detection of optical traces from single cells (**Fig. 7C**). However, since the aim of the study was to investigate the global properties of networks, this interference did not prevent to answer the question posed.
The same type of experiment was performed on dissociated cultures from the cortex and hippocampus of GAD67-GFP mice in order to analyze the pattern of spontaneous events after disruption of the original cyto-architectural organization. Spontaneous Up states followed a power law distribution with resonances in both cortical and dissociated cultures, suggesting that Global Up states are independent from network architecture. The duration of Global Up states, however, was decreased in the dissociated comparing to the organotypic tissue. These results suggest that Global Up states emerge because of the intrinsic biophysical properties of neurons, yet their duration and frequency are influenced by the specific network architecture.
As opposite to brain slices, dissociated cultures from GAD67-GFP mice allowed a fine, single-cell resolution for distinguishing calcium transients from GABAergic and non-GABAergic neurons. A previous study on dissociated neurons from the same mouse line, plated on MEAs, revealed no difference in firing properties, i.e. spike waveform and spike timing, between GABAergic and non-GABAergic neurons[23]. This work investigates instead the network properties of these two neuronal subtypes and shows that GABAergic neurons have more frequent and synchronized calcium transients. The identification of neuronal types was made by using the calcium sensitive dye Fura-Red and the intrinsic GFP-fluorescence of GABAergic neurons in the preparation: since an overlap exists between the emission spectra of calcium-free Fura-Red and GFP between 450-500 nm, a percentage of error might be present within this identification. However, no changes in fluorescence intensities were detected when recording in the green channel from Fura-Red loaded cells, meaning that the optical filter (FITC, 490-525 nm excitation/emission maximal wavelengths) effectively blocked the fluorescence from the calcium sensitive dye. This last result is in line with previous findings from *in vivo* experiments characterizing the membrane properties of fast spiking (FS) and non-fast spiking (NFS) cortical interneurons [51], which show an increased frequency of action potentials in FS comparing to both NFS and excitatory neurons (**Fig. 7D-E**).

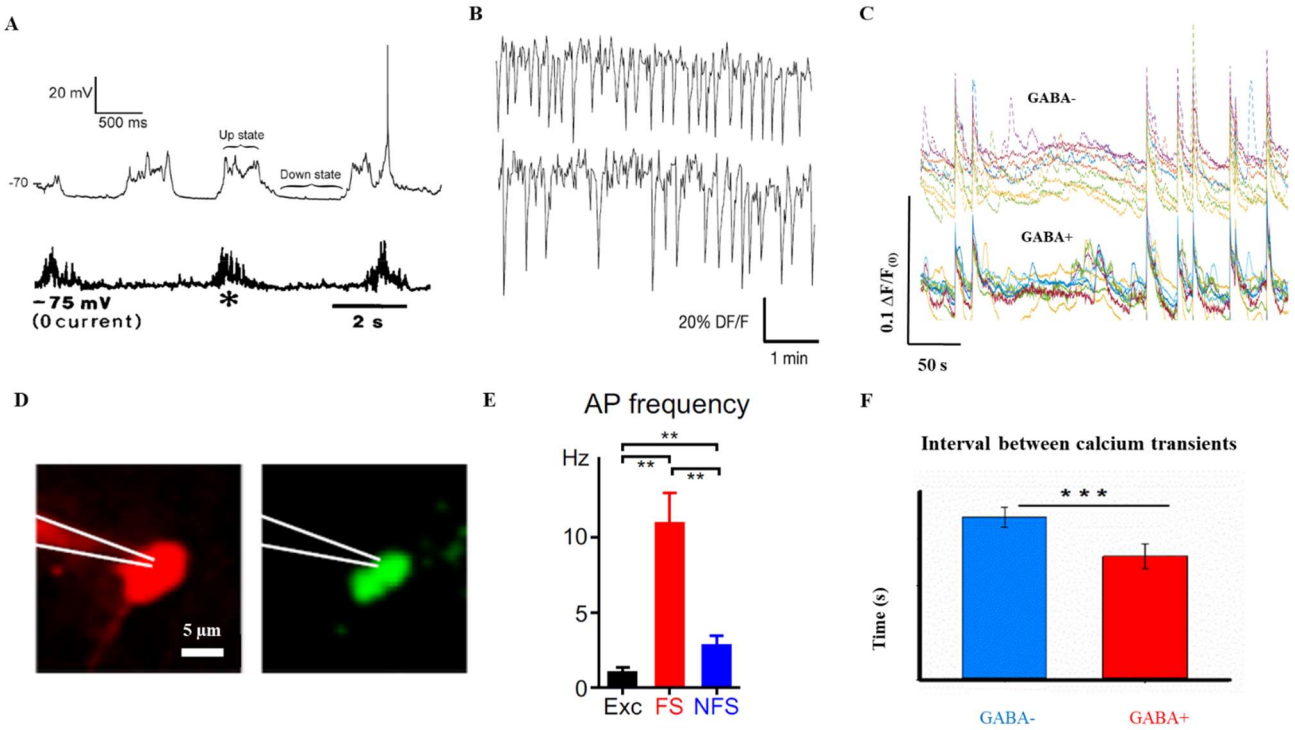


**Figure 7. Up and Down states emerge *in vivo* and *in vitro*, in different species and in different network architectures. (A)** Extracellular recordings from anesthetized rat (upper trace) and cat (lower trace) revealing oscillations between Up and Down states. **(B)** Up and Down states from two-photon calcium imaging in a cortical slice. **(C)** Up and Down states from GABAergic and non-GABAergic neurons of a cortical slice from GAD67-GFP mouse, in wide.field microscopy. **(D)** Representative GABAergic neuron from the barrel cortex of a behaving GAD67-GFP mouse, filled with a red fluorescent dye and identified by positive GFP staining (green). **(E)** Increased frequency of action potentials (AP) in Fast Spiking (FS) inhibitory neurons comparing to Excitatory (Exc) and non-Fast Spiking (NFS) inhibitory neurons, from the same mouse as in (D). **(F)** Frequency of calcium transients in GABAergic (red) and non-GABAergic (blue) dissociated cortical neurons, expressed as interval between consecutive signals. From Ref. 1, 42, 51 (A, B, D, E). Panels **C-F** represent data from the work discussed within this section.

## 3. Discussion and conclusions

A deeper understanding of which intrinsic/extrinsic properties of neuronal networks are necessary for the onset of spontaneous Up states - and influence their size and dynamical properties - might clarify some mechanisms underlying brain's dynamics. *In vitro* neuronal networks exhibit a spontaneous activity with properties similar to the one observed in the brain at rest. Therefore, they can be useful as, in addition to the reduced use of animals, they have the advantage of being more accessible and free from the interfering substances - such as anesthetics - used for *in vivo* experiments. This study provides a detailed characterization of the patterns of spontaneous activity in different *in vitro* models, discusses their level of similarity with the corresponding *in vivo* network and determines which factors in the network have an influence on its electrical rhythm.

The first and second work presented within this dissertation underline the effect of soluble factors and of the topography of the artificial extra-cellular matrix in the morphology and function of dissociated neuronal cultures. The methods used for producing dissociated cultures allowed the survival of about 30% of astrocytes, which were shown to develop a mature, stellate morphology in the presence of a more complex chemical composition or topographical patterns. This astrocytic phenotype, known to be more similar to the *in vivo* comparing to the flat, fibroblast-like morphology, might have an impact on the morphology of the connecting neurons as well. In fact, neurons co-cultured with the former astrocytic type and in the presence of astrocyte-released factors develop more elaborated growth cones, and increased neuronal arborization. Moreover, they present more

frequent and synchronous calcium transients comparing to neurons grown in different conditions (i.e. in animal-derived serum and in the presence of fibroblast-like astrocytes). This is in line with recent studies proving that a disrupted astrocytic morphology in the culture results in a loss of synchronization between neurons and in an abnormally increased synaptic density, as a result of impaired autophagy processes[57]. In fact, astrocytes were proven to modulate neuronal excitability by clearing $K^+$ ions from the extra-cellular environment[58]. Neurons grown on hybrid micro/nanopatterns are slightly less synchronous comparing to the ones grown on micropatterns only. However, they still maintain a high level of cross-correlation index between peaks of calcium transients ($0.76 \pm 0.01$). Moreover, they show a significant increase in frequency that might be due to an increased synaptic density driven by the nanotopography of the substrate (as in line with previous findings on dissociated neurons grown on carbon nanotubes). In addition, the presence of mature, stellate astrocytes on the micro/nanopattern might have a positive effect on the frequency of neuronal activity, resulting from a more complex calcium signaling between neurons and glia.

The third work presented within this dissertation investigates the effect of network architecture in the onset of the so-called Local and Global up states. This work demonstrates the occurrence of global events in both organotypic and dissociated neuronal cultures, but with different properties. Organotypic cultures are assumed as multilayered systems, while dissociated cultures as single-layered ones. Interestingly, I found that - increasing the complexity of the network - i.e. the number of layers - the duration of spontaneous events increases while their frequency decreases. Simulations with simplified neuronal networks confirmed the experimental data obtained. From these simulations, the most likely reason why complex multilayered networks have longer but less frequent "ringing" behaviour is that they are closer to criticality. When the number of layers in the network decreases, in fact, the probability that a local avalanche in a neighbouring layer perturbs a layer close to criticality is higher; the neurons in this model then would fire earlier (and would exit the criticality state) comparing to a system in which two randomly chosen layers have higher probability of being separated.

Taken together, these results show that the network architecture and the extra-cellular environment do not affect the intrinsic ability of neurons to develop a synchronous spontaneous activity - which is therefore a result of the connectivity and membrane biophysical properties such as synaptic densities, ionic conductances and neurotransmitter receptors. However, the chemical composition and the topography of the extra-cellular environment influence the size of Global Up states, i.e. the number of neurons participating in the avalanches and therefore the degree of synchrony of the network. On the other side, the network architecture modulates the duration and frequency of Global Up states.

In conclusion, this work provides a characterization of the emergent dynamical properties and their modulating factors in different neuronal network models. For these reasons, this study will be useful for choosing the appropriate model in order to investigate important biological questions. In fact, network disorders such as epilepsy are still investigated using *in vitro* preparations (e.g. patient-derived induced pluripotent stem cells): understanding the effect of intrinsic and extrinsic factors on a network's electrical activity is necessary in order to obtain a more realistic interpretation of the results obtained. In addition, this study provides some useful insights for comparison of experimental data with simplified neural networks models.

## 4. References


1. Steriade, M., Nuñez, A. & Amzica, F. A novel slow (< 1 Hz) oscillation of neocortical neurons in vivo: depolarizing and hyperpolarizing components. *J. Neurosci. Of. J. Soc. Neurosci.* **13,** 3252–3265 (1993).
2. Constantinople, C. M. & Bruno, R. M. Effects and Mechanisms of Wakefulness on Local Cortical Networks. *Neuron* **69,** 1061–1068 (2011).
3. Douglas, R. J. & Martin, K. A. C. Neuronal circuits of the neocortex. *Annu. Rev. Neurosci.* **27,** 419–451 (2004).
4. Massimini, M., Huber, R., Ferrarelli, F., Hill, S. & Tononi, G. The sleep slow oscillation as a traveling wave. *J. Neurosci. Of. J. Soc. Neurosci.* **24,** 6862–6870 (2004).
5. Sirota, A. & Buzsáki, G. Interaction between neocortical and hippocampal networks via slow oscillations. *Thalamus Relat. Syst.* **3,** 245 (2005).
6. Mohajerani, M. H. & Cherubini, E. Role of giant depolarizing potentials in shaping synaptic currents in the developing hippocampus. *Crit. Rev. Neurobiol.* **18,** 13–23 (2006).
7. Ben-Ari, Y., Cherubini, E., Corradetti, R. & Gaiarsa, J. L. Giant synaptic potentials in immature rat CA3 hippocampal neurones. *J. Physiol.* **416,** 303–325 (1989).
8. Buzsáki, G. Theta Oscillations in the Hippocampus. *Neuron* **33,** 325–340 (2002).
9. Somogyi, P. & Klausberger, T. Defined types of cortical interneurone structure space and spike timing in the hippocampus. *J. Physiol.* **562,** 9–26 (2005).
10. Teleńczuk, B. *et al.* Local field potentials primarily reflect inhibitory neuron activity in human and monkey cortex. *Sci. Rep.* **7,** 40211 (2017).
11. Dotti, C. G., Sullivan, C. A. & Banker, G. A. The establishment of polarity by hippocampal neurons in culture. *J. Neurosci. Of. J. Soc. Neurosci.* **8,** 1454–1468 (1988).
12. da Silva, J. S. & Dotti, C. G. Breaking the neuronal sphere: regulation of the actin cytoskeleton in neuritogenesis. *Nat. Rev. Neurosci.* **3,** 694–704 (2002).
13. Eichberg, J. & Hauser, G. The subcellular distribution of polyphosphoinositides in myelinated and unmyelinated rat brain. *Biochim. Biophys. Acta BBA - Lipids Lipid Metab.* **326,** 210–223 (1973).

14. Hughes, C. S., Postovit, L. M. & Lajoie, G. A. Matrigel: A complex protein mixture required for optimal growth of cell culture. *PROTEOMICS* **10,** 1886–1890

15. Todd, G. K. *et al.* Towards neuronal organoids: a method for long-term culturing of high-density hippocampal neurons. *PlOS ONE* **8,** e58996 (2013).

16. Pozzi, D., Ban, J., Iseppon, F. & Torre, V. An improved method for growing neurons: Comparison with standard protocols. *J. Neurosci. Methods* **280,** 1–10 (2017).

17. Lafon-Cazal, M. *et al.* Proteomic Analysis of Astrocytic Secretion in the Mouse: comparison with the cerebrospinal fluid proteome. *J. Biol. Chem.* **278,** 24438–24448 (2003).

18. Landis, D. M., Weinstein, L. A. & Skordeles, C. J. Serum influences the differentiation of membrane structure in cultured astrocytes. *Glia* **3,** 212–221 (1990).

19. Brewer, G. J., Torricelli, J. R., Evege, E. K. & Price, P. J. Optimized survival of hippocampal neurons in B27-supplemented Neurobasal, a new serum-free medium combination. *J. Neurosci. Res.* **35,** 567–576 (1993).

20. Ivenshitz, M. & Segal, M. Neuronal density determines network connectivity and spontaneous activity in cultured hippocampus. *J. Neurophysiol.* **104,** 1052–1060 (2010).

21. Ebrahimi, M. *et al.* Astrocyte-expressed FABP7 regulates dendritic morphology and excitatory synaptic function of cortical neurons. *Glia* **64,** 48–62 (2016).

22. Tamamaki, N. *et al.* Green fluorescent protein expression and colocalization with calretinin, parvalbumin, and somatostatin in the GAD67-GFP knock-in mouse. *J. Comp. Neurol.* **467,** 60–79 (2003).

23. Weir, K., Blanquie, O., Kilb, W., Luhmann, H. J. & Sinning, A. Comparison of spike parameters from optically identified GABAergic and glutamatergic neurons in sparse cortical cultures. *Front. Cell. Neurosci.* **8,** 460 (2014).

24. Murphy, T. H., Blatter, L. A., Wier, W. G. & Baraban, J. M. Spontaneous synchronous synaptic calcium transients in cultured cortical neurons. *J. Neurosci. Of. J. Soc. Neurosci.* **12,** 4834–4845 (1992).

25. Björklund, U., Persson, M., Rönnbäck, L. & Hansson, E. Primary Cultures From Cerebral Cortex and Hippocampus Enriched in Glutamatergic and GABAergic Neurons. *Neurochem. Res.* **35,** 1733–1742 (2010).

26. Biffi, E., Regalia, G., Menegon, A., Ferrigno, G. & Pedrocchi, A. The Influence of Neuronal Density and Maturation on Network Activity of Hippocampal Cell Cultures: A Methodological Study. *PLOS ONE* **8,** e83899 (2013).

27. Irons, H. R. *et al.* Three-dimensional neural constructs: a novel platform for neurophysiological investigation. *J. Neural Eng.* **5,** 333–341 (2008).

28. Engler, A. J., Sen, S., Sweeney, H. L. & Discher, D. E. Matrix Elasticity Directs Stem Cell Lineage Specification. *Cell* **126,** 677–689 (2006).

29. Lovat, V. *et al.* Carbon nanotube substrates boost neuronal electrical signaling. *Nano Lett.* **5,** 1107–1110 (2005).

30. Cellot, G. *et al.* Carbon nanotube scaffolds tune synaptic strength in cultured neural circuits: novel frontiers in nanomaterial-tissue interactions. *J. Neurosci. Of. J. Soc. Neurosci.* **31,** 12945–12953 (2011).

31. Li, N. *et al.* Three-dimensional graphene foam as a biocompatible and conductive scaffold for neural stem cells. *Sci. Rep.* **3,** 1604 (2013).

32. Posypanova, G. A., Gayduchenko, I. A., Moskaleva, E. Y. & Fedorov, G. E. Neuronal differentiation of PC12 cells and mouse neural stem cells on carbon nanotube films. *Cell Tissue Biol.* **10,** 194–201 (2016).

33. Ulloa Severino, F. P. *et al.* The role of dimensionality in neuronal network dynamics. *Sci. Rep.* **6,** 29640 (2016).

34. Bosi, S. *et al.* From 2D to 3D: novel nanostructured scaffolds to investigate signalling in reconstructed neuronal networks. *Sci. Rep.* **5,** 9562 (2015).

35. Aurand, E. R. *et al.* Nanostructures to Engineer 3D Neural-Interfaces: Directing Axonal Navigation toward Successful Bridging of Spinal Segments. *Adv. Funct. Mater.* **28,** 1700550

36. Li, S. *et al.* Improved neuron culture using scaffolds made of three-dimensional PDMS micro-lattices. *Biomed. Mater.* **13,** 034105 (2018).

37. Wei, J., Pozzi, D., Ulloa Severino, F. P., Torre, V. & Chen, Y. Fabrication of PLGA nanofibers on PDMS micropillars for neuron culture studies. *Microelectron. Eng.* **175,** 67–72 (2017).

38. Wei, J. *et al.* Fabrication of adjacent micropillar arrays with different heights for cell studies. *Microelectron. Eng.* **158,** 22–25 (2016).

39. Nagayama, K., Inoue, T., Hamada, Y. & Matsumoto, T. A novel patterned magnetic micropillar array substrate for analysis of cellular mechanical responses. *J. Biomech.* **65,** 194–202 (2017).

40. Migliorini, E. *et al.* Nanomechanics controls neuronal precursors adhesion and differentiation. *Biotechnol. Bioeng.* **110,** 2301–2310 (2013).

41. Musick, K. M. *et al.* Chronic multichannel neural recordings from soft regenerative microchannel electrodes during gait. *Sci. Rep.* **5,** 14363 (2015).

42. Cossart, R., Aronov, D. & Yuste, R. Attractor dynamics of network UP states in the neocortex. *Nature* **423,** 283–288 (2003).

43. Bonifazi, P. *et al.* GABAergic Hub Neurons Orchestrate Synchrony in Developing Hippocampal Networks. *Science* **326,** 1419–1424 (2009).

44. Sanchez-Vives, M. V. & McCormick, D. A. Cellular and network mechanisms of rhythmic recurrent activity in neocortex. *Nat. Neurosci.* **3,** 1027–1034 (2000).

45. Compte, A. *et al.* Spontaneous High-Frequency (10-80 Hz) Oscillations during Up States in the Cerebral Cortex In Vitro. *J. Neurosci.* **28,** 13828–13844 (2008).

46. Capone, C. *et al.* Slow Waves in Cortical Slices: How Spontaneous Activity is Shaped by Laminar Structure. *Cereb. Cortex* 1–17 doi:10.1093/cercor/bhx326

47. Okamoto, K. *et al.* Ex vivo cultured neuronal networks emit in vivo-like spontaneous activity. *J. Physiol. Sci. JPS* **64,** 421–431 (2014).

48. Allene, C. *et al.* Dynamic Changes in Interneuron Morphophysiological Properties Mark the Maturation of Hippocampal Network Activity. *J. Neurosci.* **32,** 6688–6698 (2012).

49. Cobb, S. R., Buhl, E. H., Halasy, K., Paulsen, O. & Somogyi, P. Synchronization of neuronal activity in hippocampus by individual GABAergic interneurons. *Nature* **378,** 75–78 (1995).

50. Galarreta, M. & Hestrin, S. A network of fast-spiking cells in the neocortex connected by electrical synapses. *Nature* **402,** 72–75 (1999).

51. Gentet, L. J., Avermann, M., Matyas, F., Staiger, J. F. & Petersen, C. C. H. Membrane Potential Dynamics of GABAergic Neurons in the Barrel Cortex of Behaving Mice. *Neuron* **65,** 422–435 (2010).

52. Guo, D., Zou, J., Rensing, N. & Wong, M. In Vivo Two-Photon Imaging of Astrocytes in GFAP-GFP Transgenic Mice. *PLOS ONE* **12,** e0170005 (2017).

53. Foo, L. C. *et al.* Development of a method for the purification and culture of rodent astrocytes. *Neuron* **71,** 799–811 (2011).

54. Golshani, P. *et al.* Internally mediated developmental desynchronization of neocortical network activity. *J. Neurosci. Of. J. Soc. Neurosci.* **29,** 10890–10899 (2009).

55. Beggs, J. M. & Plenz, D. Neuronal avalanches in neocortical circuits. *J. Neurosci. Of. J. Soc. Neurosci.* **23,** 11167–11177 (2003).

56. Schröter, M., Paulsen, O. & Bullmore, E. T. Micro-connectomics: probing the organization of neuronal networks at the cellular scale. *Nat. Rev. Neurosci.* **18,** 131–146 (2017).

57. Kanner, S. *et al.* Astrocytes restore connectivity and synchronization in dysfunctional cerebellar networks. *Proc. Natl. Acad. Sci.* **115,** 8025–8030 (2018).

58. Bellot-Saez, A., Kékesi, O., Morley, J. W. & Buskila, Y. Astrocytic modulation of neuronal excitability through K+ spatial buffering. *Neurosci. Biobehav. Rev.* **77,** 87–97 (2017).

## 5. Results and Methods

This section contains two published works and one that has recently been submitted to The Journal of Physiology. I designed and wrote all these works together with my co-first authors, when present, and with my supervisor. My specific contribution to each work was:

- Setting of the culturing protocol, calcium imaging experiments and data analysis for the first article.
- Production of the micro-engineered substrate, optimization of the electrospinning protocol, testing with neuronal cultures, calcium imaging experiments and data analysis for the second article.
- Setting of the brain slices preparation, calcium imaging experiments and part of the data analysis (excluding the image processing algorithms and the simulations) for the third article.

Journal of Neuroscience Methods 280 (2017) 1–10

Contents lists available at ScienceDirect

Journal of Neuroscience Methods

journal homepage: www.elsevier.com/locate/jneumeth

Research Paper

# An improved method for growing neurons: Comparison with standard protocols

Diletta Pozzi[a,1], Jelena Ban[a,b,1], Federico Iseppon[a], Vincent Torre[a,*]

[a] Neurobiology Sector, International School for Advanced Studies (SISSA), via Bonomea 265, 34136 Trieste, Italy
[b] Department of Biotechnology, University of Rijeka, Radmile Matejčić 2, 51000 Rijeka, Croatia

## HIGHLIGHTS

- An improved protocol for primary hippocampal cell cultures is proposed.
- The method relies on serum-free astrocytes conditioned medium (ACM).
- The ACM method is extensively compared with other two commonly used protocols.
- ACM improved morphology and function of both short- and long-term cultures.

## GRAPHICAL ABSTRACT

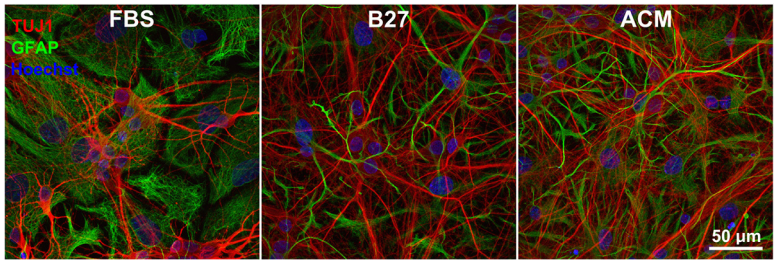


## ARTICLE INFO

*Article history:*
Received 30 November 2016
Received in revised form 17 January 2017
Accepted 22 January 2017
Available online 27 January 2017

*Keywords:*
Neuronal culture
Astrocyte
B27 Supplement
Fetal bovine serum
Neuronal branching
Calcium signaling

## ABSTRACT

*Background:* Since different culturing parameters – such as media composition or cell density – lead to different experimental results, it is important to define the protocol used for neuronal cultures. The vital role of astrocytes in maintaining homeostasis of neurons – both *in vivo* and *in vitro* – is well established: the majority of improved culturing conditions for primary dissociated neuronal cultures rely on astrocytes.
*New method:* Our culturing protocol is based on a novel serum-free preparation of astrocyte – conditioned medium (ACM). We compared the proposed ACM culturing method with other two commonly used methods Neurobasal/B27- and FBS- based media. We performed morphometric characterization by immunocytochemistry and functional analysis by calcium imaging for all three culture methods at 1, 7, 14 and 60 days in vitro (DIV).
*Results:* ACM-based cultures gave the best results for all tested criteria, *i.e.* growth cone's size and shape, neuronal outgrowth and branching, network activity and synchronization, maturation and long-term survival. The differences were more pronounced when compared with FBS-based medium. Neurobasal/B27 cultures were comparable to ACM for young cultures (DIV1), but not for culturing times longer than DIV7.
*Comparison with existing method(s):* ACM-based cultures showed more robust neuronal outgrowth at DIV1. At DIV7 and 60, the activity of neuronal network grown in ACM had a more vigorous spontaneous electrical activity and a higher degree of synchronization.
*Conclusions:* We propose our ACM-based culture protocol as an improved and more suitable method for both short- and long-term neuronal cultures.



## 1. Introduction

Primary dissociated neuronal cultures, obtained from embryonic or postnatal rodent brain regions such as the hippocampus or the cortex, represent a well-established *in vitro* model for studying neuronal networks, both on a short (network formation) and a long

* Corresponding author.
*E-mail address:* torre@sissa.it (V. Torre).
[1] These authors contributed equally to this work.

http://dx.doi.org/10.1016/j.jneumeth.2017.01.013
0165-0270/

term (differentiation, maturation) scales (Dotti et al., 1988; da Silva and Dotti, 2002). When cells are dissociated, plated on appropriate substrates and cultured in appropriate media, they grow processes and form *ex-novo* a functional network.

Several media (N2, DMEM/F12) supplemented with serum, most commonly from fetal bovine (FBS) or horse origin, are commonly used for neuronal cultures. However, the chemical composition of the animal serum is not fully defined and includes some factors not present in the brain; moreover, the production of commercial serum is prone to batch to batch variability (Zheng et al., 2006; Arigony et al., 2013). For these reasons, the use of a chemically defined, serum-free medium is recommended for studies in which a complete control of the environment in the culture medium is required (Kivell et al., 2000). Several attempts were made in order to find serum free – media for optimal neuronal growth. Currently, the most widely used is Neurobasal medium with B27 supplement (Brewer et al., 1993; Beaudoin et al., 2012). Moreover, several modifications to Neurobasal/B27 were proposed with the addition/modification of glycoproteins, lipid and hormone molecules (NbActiv4, NS21) (Chen et al., 2008; Roth et al., 2010; Brewer et al., 2008). Most of those protocols were designed to promote long-term neuronal survival in an almost pure neuronal culture: neurons of embryonic (E18) and postnatal (P0) origin were cultured in the presence of <1% and 6–8% of glial cells, respectively (Beaudoin et al., 2012; Cullen et al., 2010).

However, the role of astrocytes for maintaining the homeostasis of neuronal cells both *in vivo* and *in vitro* has been clear for a long time (Araque and Navarrete, 2010; Nedergaard et al., 2003; Barker and Ullian, 2008; Allen and Barres, 2009; Banker, 1980). Different options are now available for a successful hippocampal cell culture, all of them involving astrocytes: I- direct plating of dissociated neurons on a glial feeder layer (Ivenshitz and Segal, 2010), II- suspension of the coverslip with plated neurons above a glial feeder layer (Kaech and Banker, 2006) and III- culturing neurons in astrocyte-conditioned medium (ACM). This third method has an advantage: it does not require a feeder cell's layer while providing all the soluble factors released by astrocytes, such as growth factors, signaling molecules and lipids (Hassanpoor et al., 2013; Ebrahimi et al., 2016; Mauch et al., 2001).

ACM has been demonstrated to increase neuronal survival and stem cell differentiation (Yamashita et al., 1992; Nakayama et al., 2003; Todd et al., 2013). However, the use of ACM in cell culturing protocols is still uncommon and often limited to *in vitro* models of pathologies, where its protective effect on neurons following mechanical injury and hypoxia has been demonstrated (Yan et al., 2013). Standard neuronal culturing methods are mostly based on serum-enriched or serum-free, supplement-enriched media (Beaudoin et al., 2012), both of which rely on commercially available resources. ACM, instead, can be obtained by the researcher from the same animal species used for primary neuronal cell's cultures.

Our goal is to establish an optimal, easy to use and reproducible culturing protocol for obtaining viable, functionally connected and long – term surviving primary hippocampal cultures. For this purpose, we compared two traditional culturing protocols with a new method based on the use of ACM as a growing medium. Our method differs from other previously published protocols (Todd et al., 2013) because the medium is produced in house and it is totally serum – free, unlike the commercial ACM obtained by conditioning of traditional astrocyte medium (supplemented with 10% FBS).

Our comparison is based on a morphometric and functional characterization of neuronal networks grown in the three different media. Above all, we describe a serum – free culturing method for long – term neuronal cultures with preserved functionality and connectivity, reminiscent of that seen in the intact tissue. The three culturing protocols that we compared were: I- FBS based medium (traditionally used in our lab (Ulloa Severino et al., 2016) and by other research groups (Ivenshitz and Segal, 2010; Cohen et al., 2008; Hughes et al., 2010); II- Neurobasal/B27 medium as described in Beaudoin (Beaudoin et al., 2012); III- our serum – free ACM medium. The exact composition for all the three growing media is reported in Section 5 and the conditions are referred to as FBS, B27 and ACM, respectively. The comparison between the three protocols was carried out by maintaining the same experimental parameters (cell density, animal age and functional tests). Therefore, the differences in morphology and electrical activity are attributed to the effect of the different media.

## 2. Results

### 2.1. Setting of the plating protocol

We analyzed the morphology, electrical activity and long-term survival of our cell cultures grown in the three different media. All other parameters such as coverslip coating, plating medium and cells density were the same in the three cases. Briefly, after dissociation, the cells were suspended in plating medium (Neuronal medium supplemented with 10% FBS, see Section 5 and Supplementary Table S1 for the complete formulation), seeded at a density of 100,000 cells/sample and incubated at 37 °C for half an hour in order to allow the cell's attachment on the coverslips previously coated with polyornithine (see Section 5). After that, the sample was divided in three groups – in this work referred to as FBS, B27 and ACM – and added to the appropriate growing medium. We used the same plating medium in the three cases because when cells were plated in serum-free Neurobasal/B27 medium, cells death increased and no electrical activity was detectable. Interestingly, when plated in ACM medium, the cells were able to survive for more than one month with consistent electrical activity (Supplementary Video S1).

### 2.2. Growth cones' morphology

Twenty-four hours after plating, we analyzed the cell morphology by immunocytochemistry. Cells were fixed and stained for filamentous actin (F-actin) and for β-tubulin III, a marker for post-mitotic neurons. At a first inspection, we observed a higher cell growth in Neurobasal/B27-based media, compared to FBS at DIV1. In particular, neuronal growth cones (GCs) were larger, thicker, richer in F-actin and had a more elaborated morphology with many filopodia (Fig. 1**A–C**). To quantify those differences, we measured and compared the surface of GCs among the three conditions. Confocal images were acquired with slice spacing of 0.2 μm, up to 5 μm z-stack thickness, and for each GC a maximum intensity projection of the stacks for F-actin was used. The contours of each GCs were manually traced and the surface was measured using ImageJ/Fiji. At least 20 GCs for each condition were analyzed (see Section 5). The GCs in Neurobasal/B27-based media were significantly larger comparing to FBS. GCs in ACM, in particular, showed the biggest size; however, the difference between ACM and B27 was not statistically significant ($36.27 \pm 1{,}69\ \mu m^2$ in FBS, $86.27 \pm 10.63\ \mu m^2$ in B27 and $102.19 \pm 8.60\ \mu m^2$ in ACM; Fig. 1**D**).

A similar analysis was done by counting the number of filopodia in each GC (Fig. 1**F**): GCs in FBS-based medium had on average $9.48 \pm 0.62$ filopodia, B27 $19.72 \pm 1$ while ACM $24.24 \pm 1.76$, matching the most complex morphology observed in B27-based media (examples of elaborated forms – never observed in FBS – are shown in Supplementary Fig. S1).

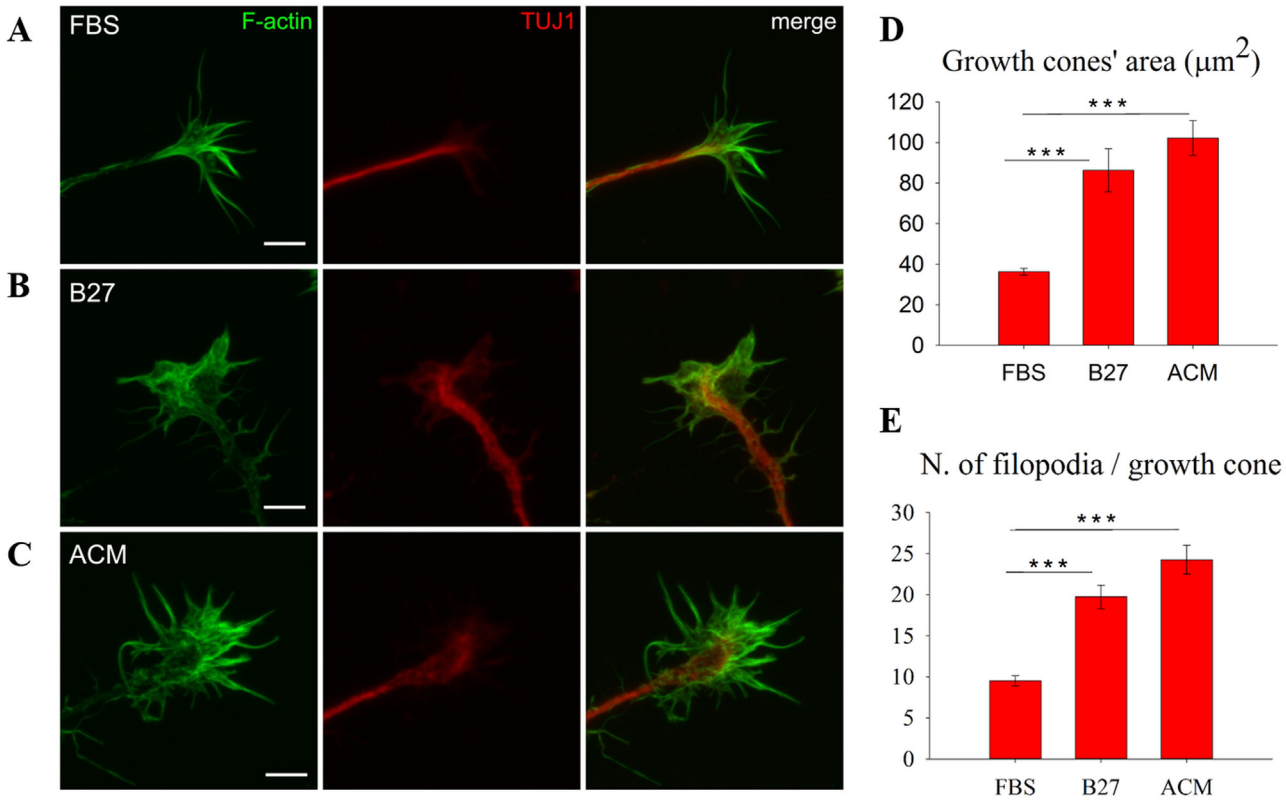


**Fig. 1.** Neuronal growth cones at DIV1 for FBS (**A**), B27 (**B**) and ACM (**C**). Cells were stained for F-actin (left), β-tubulin III (TUJ1, middle) and merged (right). (**D**) Growth cone surfaces for the three conditions tested. (**E**) Number of filopodia per growth cone for FBS, B27 and ACM respectively. Scale bar, 5 μm. n = 25 growth cones for FBS, n = 29 growth cones for B27, n = 25 growth cones for ACM. *** $p < 0.001$ One – Way ANOVA, Tukey *post – hoc* test.

**Table 1**
Number of neurites per cell at DIV1 in FBS, B27 and ACM represented as mean ± standard error of the mean. Significantly higher values were observed in B27 and ACM comparing to FBS.

| | Neurites/cell | Cells analyzed | Max number of neurites/cells |
|---|---|---|---|
| FBS | 2,87 ± 0,10 | 205 | 9 |
| B27 | 5,30 ± 0,18* | 214 | 13 |
| ACM | 5,44 ± 0,22* | 202 | 19 |

* $p < 0,001$. One – Way ANOVA, Tukey post – hoc test.

**Table 2**
Percentage of glia in the neuronal culture ± standard error of the mean in the three conditions at DIV7, with the corresponding number of cells analyzed.

| | % glia | N. cells analyzed |
|---|---|---|
| FBS | 31,92 ± 2,48 | 704 |
| B27 | 23,02 ± 2,02 | 648 |
| ACM | 29,16 ± 3,11 | 506 |

### 2.3. Neurite outgrowth

Next, we analyzed the neurite outgrowth/branching. At DIV1, the overall morphology of neurons in Neurobasal/B27-based media was more elaborated and neurites in particular were thicker and had more spines (Fig. 2**A–C**). On the other hand, neurons in FBS had thinner neurites, simpler morphology, tended to grow straight and to cluster. To quantify the differences in the three conditions we considered, the same procedure was used: at DIV1, cells were fixed, stained and confocal images were acquired using a tubulin marker to calculate the average number of neurites per each neuron. FBS cultures had the lowest number (2.87 ± 1.45, n = 205 neurons analyzed) comparing to the Neurobasal/B27-based media (5.30 ± 2.61 for B27 and 5.44 ± 3.06 for ACM, respectively; n = 214 neurons in B27 and n = 202 neurons in ACM, Table 1). As for GCs, the ACM condition resulted in higher branching (up to 19 neurites per neuron, compared to maximal numbers of 9 and 13 for FBS and B27, respectively; Table 1) although not significantly different when compared to B27. These results confirmed that Neurobasal/B27-based media promote extensive neurite outgrowth resulting in higher branching of neurons.

### 2.4. Astrocytes morphology and percentage

We did not observe significant differences in glial cells' morphology at this early developmental stage (DIV1, Supplementary Fig. S2). At DIV7, astrocytes grown in FBS and stained for glial fibrillary acidic protein (GFAP) assumed a flattened morphology (Fig. 3**A**). In Neurobasal/B27 media instead, complex shapes were observed with several cellular processes closely associated with neurons (Fig. 3**B** and **C**). Moreover, we compared the proportion of astrocytes between the three protocols. At DIV7, the percentage of glia in the neuronal cultures was estimated by counting GFAP – positive cells and observed to be around 32% in FBS, 23% in B27 and 29% in ACM (Table 2). As expected, because of the presence of several growth factors (Hassanpoor et al., 2013; Mauch et al., 2001), FBS and ACM resulted in higher percentages, despite the addition of the proliferation blocker cytosine-β-D-arabinofuranoside (Ara-C) at DIV2 (see Section 5). The morphological differences were progressively more pronounced with the extension of the culturing time required for glial maturation. Astrocytes in ACM and B27 develop long and branched processes typical of a more mature morphology compared to the astrocytes in FBS at DIV14 (Supplementary Fig. S3).

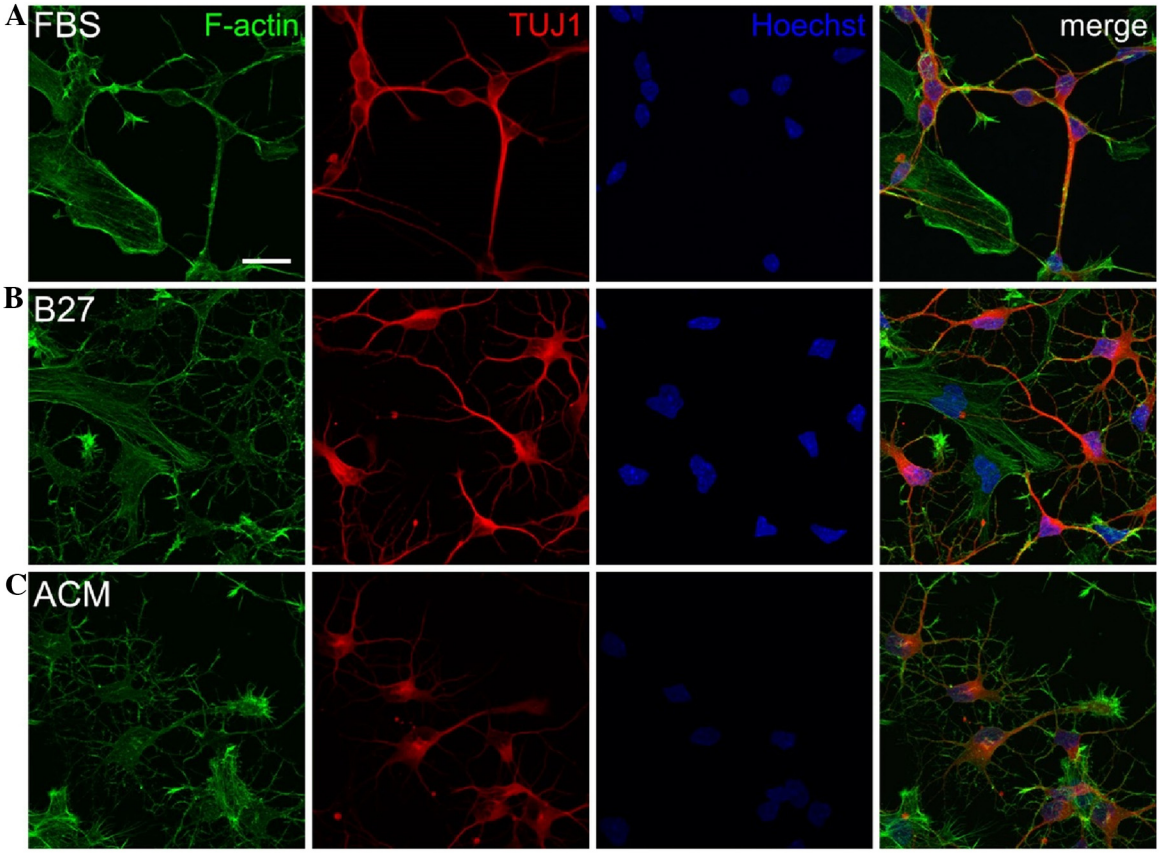


**Fig. 2.** Neuronal branching at DIV1 for FBS (**A**), B27 (**B**) and ACM (**C**). From left to right: cells were stained for F-actin (green), β-tubulin III (TUJ1, red), Hoechst nuclear marker (blue) and then merged (right). Z-stacks of about 10 μm with 0.2 μm step size were acquired and maximum intensity projections of confocal images are here shown. Scale bar, 20 μm. (For interpretation of the references to colour in this figure legend, the reader is referred to the web version of this article.)

### 2.5. Functional properties of neuronal networks

Next we investigated the functional differences among neuronal networks. The spontaneous electrical activity of the neurons was analyzed by measuring their calcium transients ($DF/F_0$) (Berridge, 1998), obtained by acquiring fluorescence images at 3–10 Hz for 10 min in every field of view. The onset time of calcium transients was defined by detecting those events in the fluorescence signal that exceeded at least by three times the standard deviation of the noise (about 0.01 $DF/F_0$, see Section 5). Moreover, we added tetrodotoxin (TTX) to the dish at the end of the recording (Supplementary Fig. S4) and verified the disappearance of calcium signals in the majority of cells in the culture, that were identified as neurons. The remaining cells were identified as astrocytes and excluded from the analysis, since they were showing calcium signals after TTX addition in the typical form of calcium waves (Scemes and Giaume, 2006).

Fluorescent images of the three cultures at DIV7, loaded with Oregon Green 488 BAPTA $-1^{®}$ cell-permeable calcium dye, and their representative traces are shown in Fig. 4**A–C**. The frequency of calcium peaks (Fig. 4**D**) showed an increasing trend from FBS ($0.020 \pm 0.002$ peaks/s) to B27 ($0.026 \pm 0.002$ peaks/s) and ACM ($0.0322 \pm 0.0004$ peaks/s) with significant differences between FBS and ACM. Moreover, the mean time interval between calcium peaks (Inter Event Interval, IEI, Fig. 4**E**) was measured for every neuronal trace in order to analyze not only the frequency but also the distribution of peaks over time: the lowest value was observed in the ACM condition, with significant differences compared to FBS; an increase in the IEI was observed in B27 compared to ACM, although not significant ($63.99 \pm 4.73$ s for FBS; $57.06 \pm 9.53$ s for B27; $37.88 \pm 2.80$ s for ACM). Neurons grown in ACM showed a more homogeneous distribution of IEI comparing to the other conditions, as shown in Fig. 4**G**. Finally, the average correlation index (Fig. 4**F**) between the calcium peaks of different cells was calculated from cross correlation raster plots (see Section 5) and showed a significantly higher value in ACM ($0.684 \pm 0.004$) when compared to both FBS ($0.430 \pm 0.005$) and B27 ($0.614 \pm 0.012$); a significantly higher value was also found in B27 compared to FBS (n = 157(5) couples of neurons (cultures) for FBS; n = 647(4) couples of neurons (cultures) for B27; n = 1680(4) couples of neurons (cultures) for ACM). Taken together, these data show that ACM cultures have higher frequency and synchronous activity compared to both FBS and B27.

Subsequently, we performed the same experiment with neuronal cultures at mature stages, *i.e.* 2 months growth (Fig. 5). The overall pattern of spontaneous electrical activity was found to be similar to the previously examined time point. The average frequency of calcium peaks (Fig. 5**D**) was still significantly increased in ACM when compared to the other two conditions, while a difference between B27 and FBS was no longer observed ($0.063 \pm 0.006$ peaks/s in FBS; $0.058 \pm 0.005$ peaks/s in B27; $0.091 \pm 0.005$ peaks/s in ACM). An increased IEI (Fig. 5**E**) was found in FBS compared to both B27–based media ($24.45 \pm 2.49$ s in FBS; $23.03 \pm 2.67$ s in B27; $17.35 \pm 1.45$ s in ACM). The distribution of IEI at this point was instead similar in the three conditions (Fig. 5**G**). Finally, a significantly higher cross correlation index (Fig. 5**F**) was measured in both B27–based media compared to FBS, and in ACM compared to B27 (0.62 for 363(4) couples of neurons (cultures) in FBS; 0.77 for 504(4) couples of neurons (cultures) in B27; 0.83 for 844(4) couples of neurons (cultures) in ACM). Thus, the neuronal cultures grown

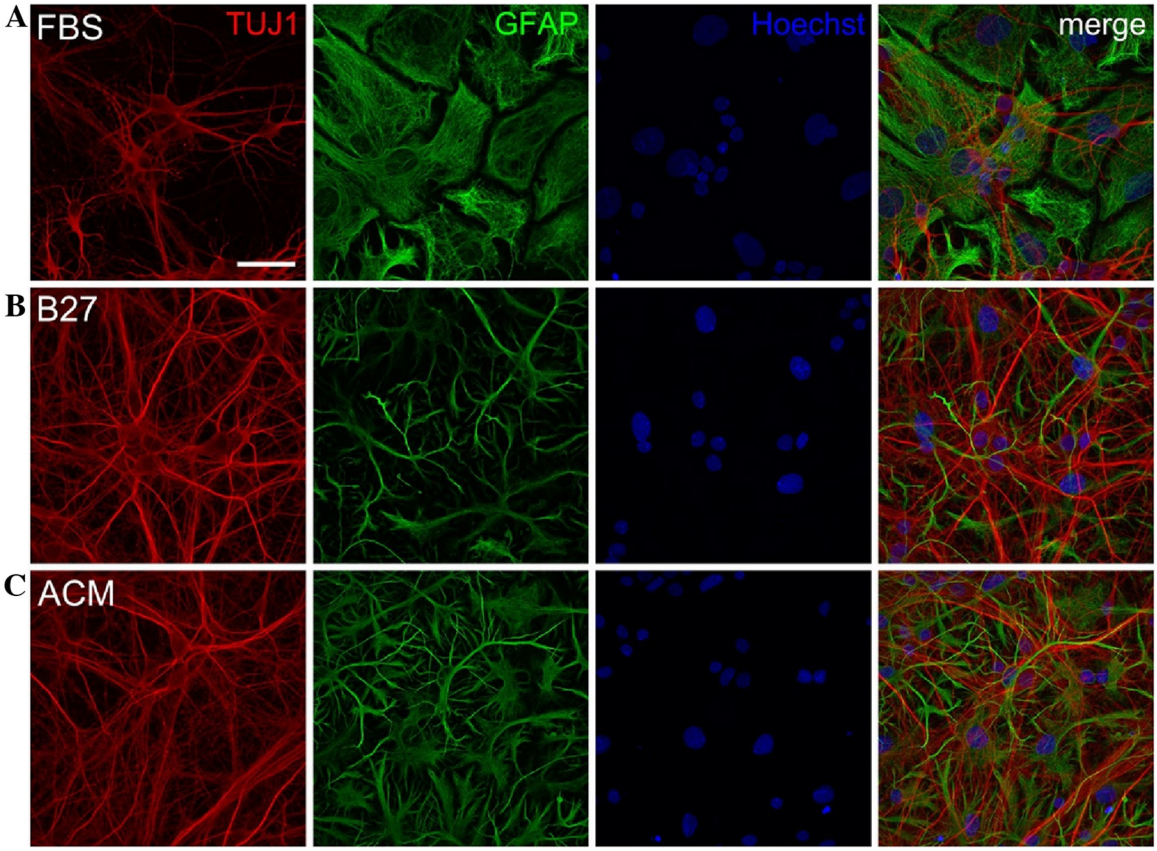


**Fig. 3.** Neurons and glial cells morphology at DIV7 for FBS (**A**), B27 (**B**) and ACM (**C**). From left to right: cells were stained for β-tubulin III (TUJ1, red), GFAP (green), Hoechst nuclear staining (blue), and then merged. Confocal maximum intensity projections images of about 15 μm-thick z stacks acquired with 0,5 μm step size are here shown. Scale bar, 50 μm. (For interpretation of the references to colour in this figure legend, the reader is referred to the web version of this article.)

in ACM maintain an overall higher spontaneous electrical activity and higher degree of synchrony over time compared to the cultures grown in traditional media. These results are consistent with previous works that demonstrate the advantage of using ACM for growing long – term cell cultures (Todd et al., 2013).

### 2.6. Cell survival and morphology in the long – term cultures

Finally, we investigated the cell morphology of the three different cultures by immunocytochemistry. Neurons were stained with microtubule associated protein (MAP) 2 and astrocytes with GFAP (Fig. 6**A–B**). After 2 months, ACM cultures showed a denser neuronal network with higher cell survival, while in both FBS and B27 we observed a progressive increase of cell-free surface, most probably due to the loss of neurons. Astrocytes in FBS maintained a relatively simple, undifferentiated morphology with low degree of arborization. In contrast, GFAP staining in B27 revealed thin and long astrocytes processes. ACM cultures maintained a highly branched and complex phenotype, similar to mature astrocytes observed *in vivo* (Puschmann et al., 2013).

## 3. Discussion

Our aim is to establish a reproducible and easy – to – use protocol for growing long – term neuronal cultures with healthy and almost physiological functional properties. For this purpose, we produced a serum – free, Neurobasal/B27 – based ACM for growing primary hippocampal neurons directly after plating, unlike other methods in which neurons are first grown in serum – enriched media (Zhu et al., 2006). Unlike commercially available astrocyte – conditioned media, our ACM is derived from the same animal species and strain used for primary neuronal preparations and contains no additives. We harvested ACM as a growing medium, which allows a controlled percentage of glia in the culture. In this way, we preserved the physiological crosstalk between neurons and glia cells without using the glial feeder layer.

The resulting hippocampal cultures in ACM showed more robust neuronal outgrowth and branching compared to those grown in a serum – enriched medium, which makes them suitable for developmental studies as they provide an *in vitro* model reminiscent of the physiological CNS. Even though little is known about the *in vivo* morphology of axonal and dendritic growth cones, some works report evidence that the structure of neuronal growth cones is elaborated with numerous filopodia, especially at early developmental stages (Hossain et al., 2012). Astrocytes grown in serum – free conditions show a complex morphology that better represents *in vivo* systems (Puschmann et al., 2013; Wolfes et al., 2017) comparing to the flat astrocytic cell's bodies observed in FBS (compare astrocytes morphology between ACM and FBS in Fig. 3 and Supplementary Fig. S3). Indeed, the fibroblast-like morphology of astrocytes is known as an artifact due to the presence of serum in the culturing medium (Landis et al., 1990; Foo et al., 2011). Astrocytes in the hippocampus of adult rats show instead numerous branches and processes as previously demonstrated (Cerbai et al., 2012).

In addition to the improved short-term cultures, we obtained long-term neuronal cultures with preserved functional connectivity up to two months, as demonstrated by calcium imaging experiments. Different culturing conditions, i. e. physical properties and chemical composition of the medium used, may affect the affinity of the dye for calcium ions and the fluorescence intensity itself

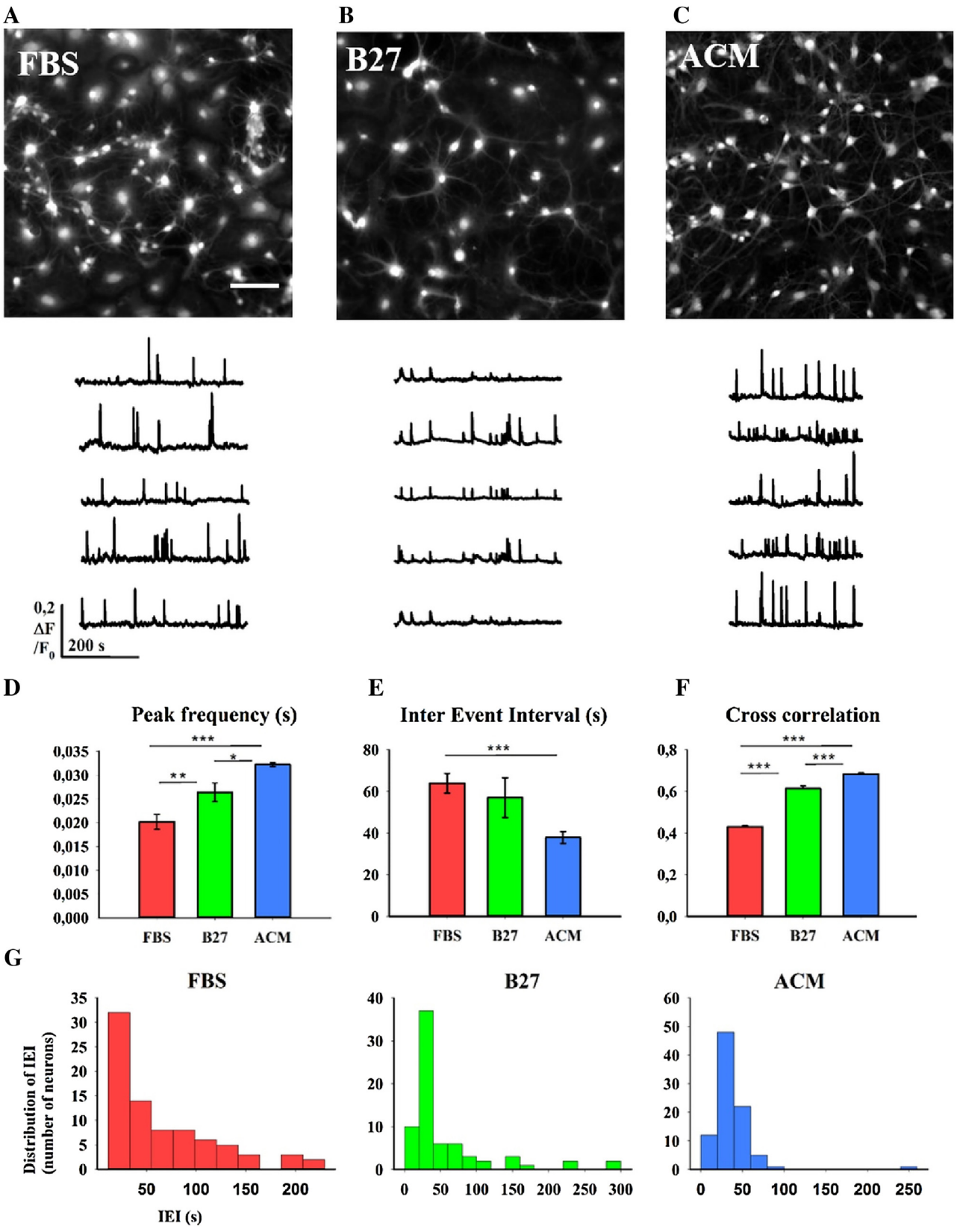


**Fig. 4.** Fluorescent images of neuronal cultures at DIV7 in FBS (**A**), B27 (**B**) and ACM (**C**) loaded with 4 μM Oregon Green 488 BAPTA – 1® and corresponding calcium traces of 5 representative neurons simultaneously recorded. Average frequency (D), Inter Event Interval (**E**) and cross correlation index (**F**) of neuronal calcium peaks in the three conditions. Distribution of Inter Event Interval (IEI) in the three conditions (**G**). Scale bar, 100 μm. n = 121 neurons for FBS; n = 71 neurons for B27; n = 98 neurons for ACM. $^{*}p < 0.05$ $^{**}p < 0.01$ $^{***}p < 0.001$ One-way ANOVA, Tukey post-hoc test). (For interpretation of the references to colour in this figure legend, the reader is referred to the web version of this article.)

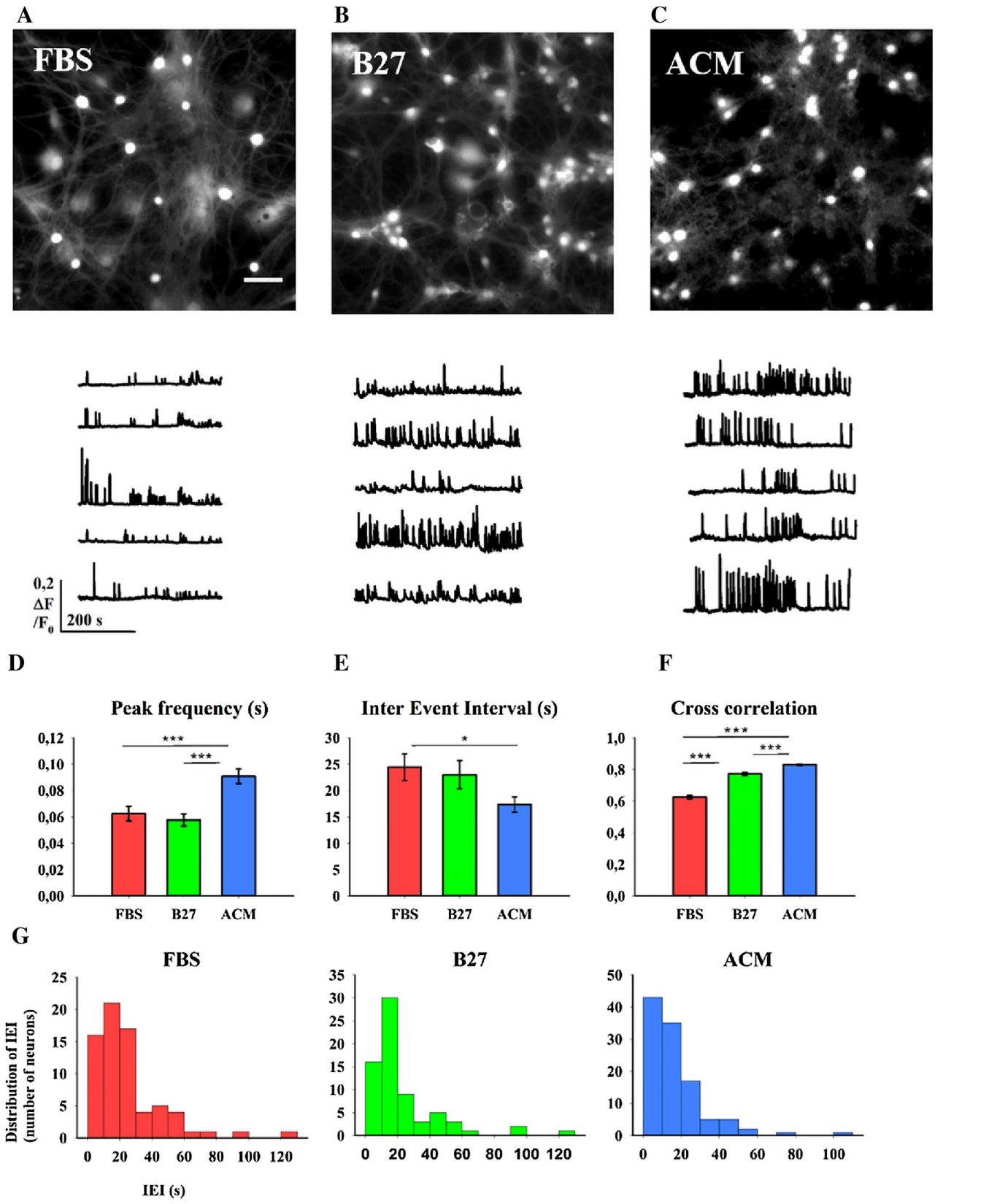


**Fig. 5.** Fluorescent images of neuronal cultures grown for 2 months in FBS (**A**), B27 (**B**) and ACM (**C**) loaded with 4 μM Oregon Green 488 BAPTA – 1, AM® and corresponding calcium traces of 5 representative neurons simultaneously recorded. Average frequency (**D**), Inter Event Interval (**E**) and cross correlation index (**F**) of neuronal calcium peaks in the three conditions. Distribution of Inter Event Interval (IEI) in the three conditions (**G**). Scale bar, 100 μm. n = 71 neurons for FBS; n = 70 neurons for B27; n = 110 neurons for ACM. *$p < 0.05$ **$p < 0.001$ One-way ANOVA, Tukey post-hoc test. (For interpretation of the references to colour in this figure legend, the reader is referred to the web version of this article.)

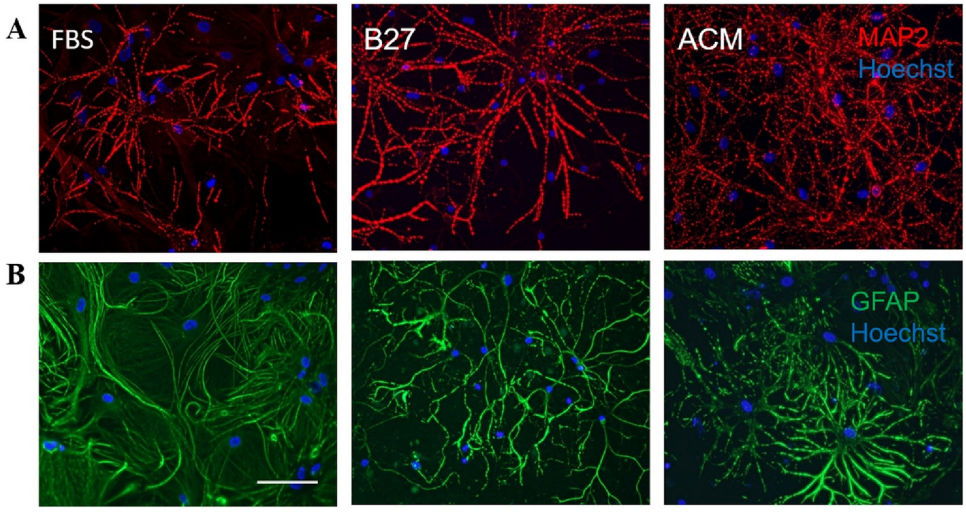


**Fig. 6.** Morphology of neurons (**A**) and astrocytes (**B**) grown for 2 months in FBS (left), B27 (middle) and ACM (right). Cells were stained for MAP2 (red), GFAP (green) and Hoechst nuclear staining (blue). Scale bar, 100 μm. (For interpretation of the references to colour in this figure legend, the reader is referred to the web version of this article.)

(Oliver et al., 2000). In order to minimize these effects, we chose Oregon Green® 488 BAPTA-1, AM calcium dye because of its high-affinity and high signal-to-noise ratio (Grienberger and Konnerth, 2012). Moreover, the same experimental conditions such as dye concentration, temperature and incubation time were maintained for all the three protocols tested. A similar level of baseline fluorescence intensity was observed by visual inspection when recording cells grown in the three culturing media. Therefore, we assume that the uptake of the calcium sensitive dye from both neurons and astrocytes was similar in the three protocols, mainly dependent on the hydrophobicity of the AM – conjugated molecule (Paredes et al., 2008). However, further investigations are required to explain the role of astrocytes secreted factors in modulation of calcium-mediated neuronal processes (Bazargani and Attwell, 2016).

The presence of the differentiating factor B27 leads to an overall increase of the network's electrical activity when compared to what happens in the serum – based medium. However, the addition of ACM to the Neurobasal/B27 medium resulted in a further amplification of the overall spontaneous activity compared to both traditional methods (see Figs. 4 and 5). In particular, neurons grown in ACM showed significantly higher degree of correlation both in the short – and in the long – term compared to FBS and B27, suggesting that the synchronizing effect attributed to astrocytes may reside in their soluble factors (Amiri et al., 2012; Sasaki et al., 2014). Moreover, we demonstrated that ACM can totally replace the use of serum, even at the plating stage, while maintaining viability and functionality of the network (Supplementary Video S1). Although Neurobasal/B27 is the most commonly used serum-free medium for neuronal cultures (so called "maintenance medium" (Beaudoin et al., 2012)) it still requires the presence of FBS in the plating medium. Finally, since ACM alone is supposed to provide all the nutrients for long – term neuronal survival (e.g. lipids, BDNF and thrombospondins (Hassanpoor et al., 2013; Ebrahimi et al., 2016; Mauch et al., 2001)), the use of additional growth factors in the culturing medium is not necessary.

## 4. Conclusions

We conclude that our ACM method is an improved and more suitable culture protocol for both short – and long – term studies, resulting in cell cultures that represent a realistic model of the CNS, useful for investigating the mechanisms of neuronal maturation and degeneration.

## 5. Materials and methods

### 5.1. Hippocampal cultures

Hippocampal neurons from Wistar rats (P2-P3) were prepared in accordance with the guidelines of the Italian Animal Welfare Act, and their use was approved by the Local Veterinary Service, the SISSA Ethics Committee board and the National Ministry of Health (Permit Number: 630-III/14) in accordance with the European Union guidelines for animal care (d.1.116/92; 86/609/C.E.). The animals were anaesthetized with $CO_2$ and sacrificed by decapitation, and all efforts were made to minimize suffering. Glass coverslips (15 mm diameter) were coated with 50 μg/ml poly-L-ornithine (Sigma-Aldrich, St. Louis, MO, USA) overnight, and just before cells' seeding, a thin layer of Matrigel® (diluted 1:50 with culture medium; Corning, Tewksbury MA, USA) was applied. Dissociated cells were resuspended in Neuronal medium with the following composition: minimum essential medium (MEM) with GlutaMAX™ supplemented with 10% dialyzed fetal bovine serum (FBS, all from Thermo Fisher Scientific, Waltham, MA, USA), 0.6% D-glucose, 15 mM Hepes, 0.1 mg/ml apo-transferrin, 30 μg/ml insulin, 0.1 μg/ml D-biotin, 1 μM vitamin B12 and 2.5 μg/ml gentamycin (all from Sigma-Aldrich). A drop containing 100,000 cells was deposited per each 15 mm diameter coverslip and incubated for 30 min at 37 °C. For each coverslip, placed in a 12-well tissue culture plate, 1.5 ml of culture medium was then added. Three sets of media were used: **I** – Neuronal medium with 10% FBS (the same used for resuspending cells, see above), **II** – Neurobasal medium supplemented with B27 and GlutaMAX™ according to the manufacturer's instructions (all from Thermo Fisher) and 2.5 μg/ml gentamycin, **III** – ACM (see below) in 1:1 ratio with Neurobasal/B27 medium. Half of the medium was changed after 48 h and 2 μM cytosine-β-D-arabinofuranoside (Ara-C; Sigma-Aldrich) was added to all culture media. The concentration of FBS (in medium containing 10% FBS) was decreased to 5%. Half of the medium was changed then twice per week. The neuronal cultures were maintained in an incubator at 37 °C, 5% $CO_2$ and 95% relative humidity. For a detailed description of the chemical composition of Neuronal vs Neurobasal medium, see Supplementary data.

### 5.2. Glia and ACM preparation

Glial cells were prepared as described in Kaech and Baker (Allen and Barres, 2009) with some modifications. Cortices from P2-P3 Wistar rats were dissociated as described for hippocampal cultures. Cells were plated in 15 μg/ml poly-L-ornithine (Sigma-Aldrich) coated tissue-culture flasks at the density of $7.5 \times 10^6$ cells per 75 $cm^2$ flask in Dulbecco's minimum essential medium (DMEM) with GlutaMAX™ (Thermo Fisher Scientific) supplemented with 10% fetal bovine serum (FBS) and Penicillin/Streptomycin (all from Euroclone, Pero, Italy). The next day the medium was changed in order to remove cell debris and loosely attached cells. Cells were cultured for ~1 week and medium was changed every 2–3 days. When almost confluent, cells were replated in 10 cm diameter Petri dishes at the density of $5 \times 10^5$ cells per dish and expanded until they reached 75% confluence. The medium was then replaced with Neurobasal medium supplemented with B27 and GlutaMAX™ (all from ThermoFisher) and 2.5 μg/ml gentamycin (Sigma-Aldrich). After 48 h ACM was collected, filtered and stored at 4 °C.

### 5.3. Immunocytochemistry and imaging

Cells were fixed in 4% paraformaldehyde containing 0.15% picric acid in phosphate-buffered saline (PBS), saturated with 0.1 M glycine, permeabilized with 0.1% Triton X-100, saturated with 0.5% BSA (all from Sigma-Aldrich) in PBS and then incubated for 1 h with primary mouse monoclonal antibodies: glial fibrillary acidic protein (GFAP, Sigma-Aldrich), anti-β-tubulin III (TUJ1, Covance, Berkeley, CA) and mouse monoclonal anti-microtubule associated protein 2 (MAP2, Sigma-Aldrich). The secondary antibodies were goat anti-mouse Alexa Fluor® 594, goat anti-mouse immunoglobulin (Ig) $G_1$ Alexa Fluor® 488 and goat anti-mouse $IgG_{2a}$ Alexa Fluor® 594. F-actin was marked with Alexa Fluor 488® phalloidin (all from Thermo Fisher Scientific) and the incubation time was 30 min. Nuclei were stained with 2 μg/ml in PBS Hoechst 33342 (Sigma-Aldrich) for 5 min. All the incubations were performed at room temperature (20–22 °C). The cells were examined using a Leica DMIRE2 confocal microscope (Leica Microsystems GmbH, Wetzlar, Germany) equipped with DIC and fluorescence optics, diode laser 405 nm, Ar/ArKr 488 nm and He/Ne 543/594 nm lasers. 63× magnification and a 1.4 NA objective was used. Images were acquired at 1024 × 1024 pixels resolution and z stacks with 200–250 nm steps. In addition, Leica DM6000 fluorescent microscope equipped with DIC and fluorescence optics, CCD camera and Volocity 5.4 3D imaging software (PerkinElmer, Coventry, UK) were used for cell counting experiments. The fluorescence images were collected with a 20× magnification and 0.5 NA objective. For each image at least 30 slices were acquired with slice spacing of 0.5 μm. Image J by W. Rasband (developed at the U.S. National Institutes of Health and available at http://rsbweb.nih.gov/ij/) was used for image processing.

### 5.4. Calcium imaging

The cells were incubated with the non-ratiometric calcium dye Oregon Green® 488 BAPTA-1, AM, (Thermo Fisher Scientific) dissolved in anhydrous DMSO (Sigma-Aldrich) at a concentration of 4 mM (stock solution), with the addition of Pluronic F-127 20% solution in dimethyl sulfoxide (DMSO, Thermo Fisher Scientific) for increasing the cell's permeability. The two components were dissolved at a ratio of 1:1 in Ringer's solution (145 mM NaCl, 3 mM KCl, 1.5 mM $CaCl_2$, 1 mM $MgCl_2$, 10 mM glucose and 10 mM Hepes, pH 7.4) to give a final dye concentration of 4 μM, and incubated at 37 °C for 30 min. The cultures were then transferred to a glass-bottom Petri dish in order to allow visualization in a Nikon Eclipse Ti-U inverted microscope equipped with an HBO 103 W/2 mercury short arc lamp (Osram, Munich, Germany), a mirror unit (exciter filter BP 465–495 nm, dichroic 505 nm, emission filter BP 515–555) and an Electron Multiplier CCD Camera C9100-13 (Hamamatsu Photonics, Japan). The experiments were performed at RT for 20 min/sample. At the end of each registration, the antagonist of voltage – gated sodium channels tetrodotoxin (TTX, Sigma–Aldrich) was added to the culture at a concentration of 1 μM and the sample was recorded for additional 5 min.

Images were acquired using the NIS Element software (Nikon, Japan) with an S-Fluor 20×/0.75 NA objective at a sampling rate of 3–10 Hz. The spatial resolution was 256 × 256 pixels. To avoid saturation of the signals, excitation light intensity was attenuated by ND4 and ND8 neutral density filters (Nikon).

### 5.5. Data analysis

#### 5.5.1. Morphometric analysis, neurite and cell counting

At least three different preparations were used. For neurite counting, nuclear stain was used to acquire randomly 3–5 fields with comparable cell densities (approx. 30 cells/field). TUJ1-stained neurites were counted and a mean number of neurites per neuron was calculated for all three tested conditions.

#### 5.5.2. $Ca^{2+}$ imaging processing and analysis

As described in our previous work (Ulloa Severino et al., 2016; Moshtagh-Khorasani et al., 2013), the initial video was processed with the ImageJ (U. S. National Institutes of Health, Bethesda, MA) software. Briefly, neurons were localized by selecting the cells bodies with a region of interest (ROI), and an additional ROI was selected to subtract the background. The fluorescence intensity over time, If(t), of every selected ROI was displayed and the extent of its decay – consequence of dye bleaching – was evaluated. To compensate photo bleaching, the decay of If(t) was fitted with a cubic or polynomial spline (Y($t$)) interpolating If($t$) at 10 or 20 points. The function Y($t$) fitting If($t$) was then added to the original optical signal – to compensate dye bleaching – and the fractional optical signal was taken as $DF/F_0 = Y(t) + If(t))/If(0)$, where If(0) is the fluorescence intensity at the beginning of the recording.

#### 5.5.3. Computation of raster plot and correlation coefficient of $Ca^{2+}$ transient occurrence

The times, $t_i$, at which transient peaks occurred are presented in a conventional raster plot.

The correlation coefficient of the calcium transients for neuron $i$ and neuron $j$ ($s_{CTij}$) was computed as follows: the total recording time, $T_{tot}$, was divided into $N$ intervals (1,. . .,n,. . .,N) of a duration $Dt$, that was fixed at 20 s. Thus, if $f_{in}$ and $f_{jn}$ are the number of calcium transients of neuron $i$ and neuron $j$ in the time interval $Dt_n$, then

$$\sigma_{CT_{ij}} = \frac{\Sigma_n f_{in} f_{jn}}{\sqrt{(\Sigma_n f_{in}^2)(\Sigma_n f_{jn}^2)}}$$

so that $s_{CTij}$ depends on $Dt$ and varies between 0 and 1.

#### 5.5.4. Statistical analysis

Data are shown as the mean ± standard error of the mean (s.e.m.) from the number of samples indicated in each experiment (see Section 2). The mean values of both morphological and activity parameters were compared among the three different conditions with One-way ANOVA test followed by Tukey post-hoc comparison, using the software SigmaPlot 10.0. Significant differences were set with p values inferior to 0.05 ($^*p < 0.05$, $^{**}p < 0.01$, $^{***}p < 0.001$).

## Acknowledgements

The research leading to these results has received funding from the European Union's Seventh Framework Programme, the NEUROSCAFFOLDS Project no. 604263. The authors would like to recognize the financial support from the 3315 Innovative Teams Program of Ningbo – China. We thank Beatrice Pastore for technical assistance, Francesco Paolo Ulloa Severino for his help with calcium imaging and Manuela Schipizza Lough for carefully reading the manuscript.

## Appendix A. Supplementary data

Supplementary data associated with this article can be found, in the online version, at http://dx.doi.org/10.1016/j.jneumeth.2017.01.013.

## References

Allen, N.J., Barres, B.A., 2009. Neuroscience: glia — more than just brain glue. Nature 457, 675–677.
Amiri, M., Bahrami, F., Janahmadi, M., 2012. Functional contributions of astrocytes in synchronization of a neuronal network model. J. Theor. Biol. 292, 60–70.
Araque, A., Navarrete, M., 2010. Glial cells in neuronal network function. Philos. Trans R. Soc. Lond. B Biol. Sci. 365, 2375–2381.
Arigony, A.L.V., et al., 2013. The influence of micronutrients in cell culture: a reflection on viability and genomic stability. BioMed Res. Int. 2013, 597282.
Banker, G.A., 1980. Trophic interactions between astroglial cells and hippocampal neurons in culture. Science 209, 809–810.
Barker, A.J., Ullian, E.M., 2008. New roles for astrocytes in developing synaptic circuits. Commun. Integr. Biol. 1, 207–211.
Bazargani, N., Attwell, D., 2016. Astrocyte calcium signaling: the third wave. Nat. Neurosci. 19, 182–189.
Beaudoin, G.M.J., et al., 2012. Culturing pyramidal neurons from the early postnatal mouse hippocampus and cortex. Nat. Protoc. 7, 1741–1754.
Berridge, M.J., 1998. Neuronal calcium signaling. Neuron 21, 13–26.
Brewer, G.J., Torricelli, J.R., Evege, E.K., Price, P.J., 1993. Optimized survival of hippocampal neurons in B27-supplemented Neurobasal, a new serum-free medium combination. J. Neurosci. Res. 35, 567–576.
Brewer, G.J., Boehler, M.D., Jones, T.T., Wheeler, B.C., 2008. NbActiv4 medium improvement to Neurobasal/B27 increases neuron synapse densities and network spike rates on multielectrode arrays. J. Neurosci. Methods 170, 181–187.
Cerbai, F., et al., 2012. The neuron-astrocyte-microglia triad in normal brain ageing and in a model of neuroinflammation in the rat hippocampus. PLoS One 7, e45250.
Chen, Y., et al., 2008. NS21: re-defined and modified supplement B27 for neuronal cultures. J. Neurosci. Methods 171, 239–247.
Cohen, E., Ivenshitz, M., Amor-Baroukh, V., Greenberger, V., Segal, M., 2008. Determinants of spontaneous activity in networks of cultured hippocampus. Brain Res. 1235, 21–30.
Cullen, D.K., Gilroy, M.E., Irons, H.R., Laplaca, M.C., 2010. Synapse-to-neuron ratio is inversely related to neuronal density in mature neuronal cultures. Brain Res. 1359, 44–55.
da Silva, J.S., Dotti, C.G., 2002. Breaking the neuronal sphere: regulation of the actin cytoskeleton in neuritogenesis. Nat. Rev. Neurosci. 3, 694–704.
Dotti, C.G., Sullivan, C.A., Banker, G.A., 1988. The establishment of polarity by hippocampal neurons in culture. J. Neurosci. Off. J. Soc. Neurosci. 8, 1454–1468.
Ebrahimi, M., et al., 2016. Astrocyte-expressed FABP7 regulates dendritic morphology and excitatory synaptic function of cortical neurons. Glia 64, 48–62.
Foo, L.C., et al., 2011. Development of a method for the purification and culture of rodent astrocytes. Neuron 71, 799–811.
Grienberger, C., Konnerth, A., 2012. Imaging calcium in neurons. Neuron 73, 862–885.
Hassanpoor, H., Fallah, A., Raza, M., 2013. Effect of BDNF Secretion by Astrocyte on Learning and Memory: A Modeling Approach., pp. 73–76, http://dx.doi.org/10.1109/ICABME.2013.6648850.
Hossain, S., Hewapathirane, D.S., Haas, K., 2012. Dynamic morphometrics reveals contributions of dendritic growth cones and filopodia to dendritogenesis in the intact and awake embryonic brain. Dev. Neurobiol. 72, 615–627.
Hughes, E.G., Elmariah, S.B., Balice-Gordon, R.J., 2010. Astrocyte secreted proteins selectively increase hippocampal GABAergic axon length, branching, and synaptogenesis. Mol. Cell. Neurosci. 43, 136–145.
Ivenshitz, M., Segal, M., 2010. Neuronal density determines network connectivity and spontaneous activity in cultured hippocampus. J. Neurophysiol. 104, 1052–1060.
Kaech, S., Banker, G., 2006. Culturing hippocampal neurons. Nat. Protoc. 1, 2406–2415.
Kivell, B.M., McDonald, F.J., Miller, J.H., 2000. Serum-free culture of rat post-natal and fetal brainstem neurons. Brain Res. Dev. Brain Res. 120, 199–210.
Landis, D.M., Weinstein, L.A., Skordeles, C.J., 1990. Serum influences the differentiation of membrane structure in cultured astrocytes. Glia 3, 212–221.
Mauch, D.H., et al., 2001. CNS synaptogenesis promoted by glia-derived cholesterol. Science 294, 1354–1357.
Moshtagh-Khorasani, M., Miller, E.W., Torre, V., 2013. The spontaneous electrical activity of neurons in leech ganglia. Physiol. Rep. 1, n/a–n/a.
Nakayama, T., Momoki-Soga, T., Inoue, N., 2003. Astrocyte-derived factors instruct differentiation of embryonic stem cells into neurons. Neurosci. Res. 46, 241–249.
Nedergaard, M., Ransom, B., Goldman, S.A., 2003. New roles for astrocytes: redefining the functional architecture of the brain. Trends Neurosci. 26, 523–530.
Oliver, A.E., Baker, G.A., Fugate, R.D., Tablin, F., Crowe, J.H., 2000. Effects of temperature on calcium-sensitive fluorescent probes. Biophys. J. 78, 2116–2126.
Paredes, R.M., Etzler, J.C., Watts, L.T., Zheng, W., Lechleiter, J.D., 2008. Chemical calcium indicators. Methods 46, 143–151.
Puschmann, T.B., et al., 2013. Bioactive 3D cell culture system minimizes cellular stress and maintains the in vivo-like morphological complexity of astroglial cells. Glia 61, 432–440.
Roth, S., Zhang, S., Chiu, J., Wirth, E.K., Schweizer, U., 2010. Development of a serum-free supplement for primary neuron culture reveals the interplay of selenium and vitamin E in neuronal survival. J. Trace Elem. Med. Biol. Organ Soc. Miner. Trace Elem. GMS 24, 130–137.
Sasaki, T., et al., 2014. Astrocyte calcium signalling orchestrates neuronal synchronization in organotypic hippocampal slices. J. Physiol. 592, 2771–2783.
Scemes, E., Giaume, C., 2006. Astrocyte calcium waves: what they are and what they do. Glia 54, 716–725.
Todd, G.K., et al., 2013. Towards neuronal organoids: a method for long-term culturing of high-density hippocampal neurons. PLoS One 8, e58996.
Ulloa Severino, F.P., et al., 2016. The role of dimensionality in neuronal network dynamics. Sci. Rep. 6, 29640.
Wolfes, A.C., et al., 2017. A novel method for culturing stellate astrocytes reveals spatially distinct Ca 2+ signaling and vesicle recycling in astrocytic processes. J. Gen. Physiol. 149, 149–170.
Yamashita, N., Nishiyama, N., Abe, K., Saito, H., Fukuda, J., 1992. Primary culture of postnatal rat hypothalamic neurons in astrocyte-conditioned medium. Brain Res. 594, 215–220.
Yan, J., Tan, T., Huang, Q., 2013. Protective effect of astrocyte-conditioned medium on neurons following hypoxia and mechanical injury. Chin. J. Traumatol. Zhonghua Chuang Shang Za Zhi Chin. Med. Assoc. 16, 3–9.
Zheng, X., et al., 2006. Proteomic analysis for the assessment of different lots of fetal bovine serum as a raw material for cell culture. Part IV. Application of proteomics to the manufacture of biological drugs. Biotechnol. Prog. 22, 1294–1300.
Zhu, Z.-H., Yang, R., Fu, X., Wang, Y.-Q., Wu, G.-C., 2006. Astrocyte-conditioned medium protecting hippocampal neurons in primary cultures against corticosterone-induced damages via PI3-K/Akt signal pathway. Brain Res. 1114, 1–10.

Microelectronic Engineering 175 (2017) 67–72

Contents lists available at ScienceDirect

Microelectronic Engineering

journal homepage: www.elsevier.com/locate/mee

Research paper

# Fabrication of PLGA nanofibers on PDMS micropillars for neuron culture studies

Jin Wei [a,1], Diletta Pozzi [b,1], Francesco Paolo Ulloa Severino [b], Vincent Torre [b,*], Yong Chen [a,c,d,**]

[a] Ecole Normale Supérieure, PSL Research University, Département de Chimie, CNRS UMR 8640 PASTEUR, 75005 Paris, France
[b] International School for Advanced Studies (SISSA),34100 Trieste, Italy
[c] Institute for Integrated Cell-Material Sciences, Kyoto University, Kyoto 606-8507, Japan
[d] Institute for Interdisciplinary Research, Jianghan University, Wuhan 430056, China

ARTICLE INFO

*Article history:*
Received 11 October 2016
Received in revised form 9 January 2017
Accepted 13 January 2017
Available online 22 January 2017

*Keywords:*
Micropillars array
Nanofiber
Neuron culture

ABSTRACT

We fabricated a nanocomposite substrate made of nanofibers on micropillar arrays by photolithography, soft lithography and electrospinning for cell culture studies. This nanocomposite substrate combines the advantage of the extra-cellular matrix (ECM)-like surface morphology and high porosity and low stiffness of underneath supporting material. For neuronal culture studies, we used nanofibers of poly (lactic-*co*-glycolic acid) (PLGA) on high aspect ratio micropillars of polydimethylsiloxane (PDMS). Our results showed that primary hippocampal neurons on such a nanocomposite substrate have different cell morphology than on flat surfaces and they showed more electric activities. Thus, the nanofiber-micropillar composite substrates were shown to be useful for neuron culture studies.



## 1. Introduction

Improvement of cell culture conditions is important for biomedical research as well as advanced applications such as tissue engineering, disease modeling and cancer treatment [1–3]. Among many others, the physical and biochemical properties of the culture substrate are critical issues in cell culture studies [4–5]. While cell adhesion and migration are dictated by topographical cues [6], the cell fate decision is clearly substrate stiffness dependent [7]. More specifically, the expression of neuronal markers and the formation of neural networks are both affected by the stiffness and the surface morphology of the culture substrate [8–10], in addition to the influence of the substrate surface coatings [11,12].

In order to simultaneously modulate the stiffness and the surface morphology of the substrate for primary neuron culture, we developed a new type of nanocomposite substrates by electrospinning poly-lactic-*co*-glycolic acid (PLGA) on polydimethylsiloxane (PDMS) pillars of high aspect ratio and small diameters. Previously, PDMS pillars have been repeatedly used for measurements of cell contracile forces [13]. PDMS pillars have also been used to facilitate stem cell differentiation toward neurons [14,15]. On the other hand, the morphology of electrospun nanofibers can be in-vivo extracellular matrix (ECM)-like so that they are prominent to cell culture studies [16,17]. While PDMS pillars of high aspect ratio and small feature sizes can serve as supporting structure with low effective Young's modules, PLGA nanofibers are highly biocompatible [18] so that such a nanocomposite substrate provides unique characteristic to guide neuronal growth and to enhance cell-medium exchange due to large free spaces underneath the fibers. Preliminary results of neuron culture and calcium imaging will be shown to illustrate the high potential of this approach.

## 2. Fabrication of PLGA nanofibers on PDMS micropillars

### 2.1. Materials

Blank chromium mask (Nanofilm Inc) and resist developer AZ726 (AZ Electronic Materials) were purchased from Cipec (France). Chrome Etch N°1 was purchased from Technic Inc. (France). SU8 photoresists (SU8-3025) and SU8 developer were obtained from CTS (France). Polydimethylsiloxane (PDMS) was purchased from Eleco-EFD (France). Dimethylformamide (DMF), tetrahydrofuran (THF) and D,L-lactide-*co*-glycolide (PLGA) were obtained from Sigma (France). Trimethylsilylchloride (TMCS) was purchased from Sigma (France).

### 2.2. Fabrication of micropillars

Micropillar arrays used in this work were obtained by casting PDMS on a PDMS mold with holes, whereas the PDMS mold was initially

* Corresponding author.
** Correspondence to: Y. Chen, Ecole Normale Supérieure, PSL Research University, Département de Chimie, CNRS UMR 8640 PASTEUR, 75005 Paris, France.
*E-mail addresses:* vincent.torre@sissa.it (V. Torre), yong.chen@ens.fr (Y. Chen).
[1] These authors contributed equally to this work.

http://dx.doi.org/10.1016/j.mee.2017.01.015
0167-9317/

obtained by PDMS casting on a photoresist mold (master) fabricated by photolithography (Fig. 1). Firstly, micro-hole arrays were patterned on the Cr mask using a micro pattern generator (μPG101, Heidelberg, Germany). Then, a 25-μm-thick negative resist layer (SU8-3025) was spin-coated on the mask and back-side ultraviolet (UV) exposed. After development, SU8 pillars of 25 μm height, 5 μm diameter and 20 μm spacing were obtained (Fig. 2a) and used as mold features to cast a mixture of PDMS pre-polymer and crosslink agent at ratio of 10:1. Before casting, the mold was treated in oxygen plasma for 2 min and then in TMSC vapor for 30 min. After PDMS casting and curing at 80 °C for 2 h, the PDMS layer was peeled-off, resulted in a negative replica of the mold features. Next, 0.2-μm thick Parylene C was deposited on the PDMS layer with a vacuum deposition system (SCS Labcoter 2, SCS ltd, UK). Afterward, a positive-tone replica of the master was finally obtained by casting PDMS on the PDMS mold using the same casting process. Comparing to the other fabrication processes, the present double casting technique is advantageous to achieve high quality PDMS pillar arrays, since it is relatively easy to obtain high resolution, high density and high aspect ratio SU8 pillars. It is also relatively easy to peel-off the PDMS layer from the fabricated resist pillars and then to replicate the same feature of the master due to the relative low Young's modules of PDMS. Previously, we have shown that it was convenient to use PDMS mold for replication of pillar structures with different types of polymers such as PDMS, PLGA and T-Flex [19]. Here, the PDMS mold was coated with a thin film of Parylene C, which further facilitated the replication due to the low surface energy of Parylene C. As results, this double casting procedure allowed us producing reproducibly high density and high aspect ratio PDMS pillar arrays (Fig. 2b).

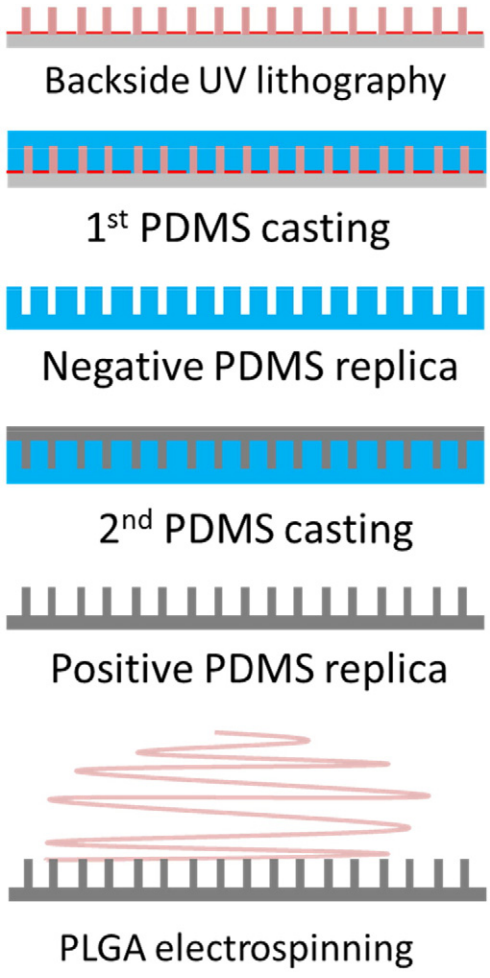


**Fig. 1.** Schematic diagram of the fabrication process of electrospun nanofibers on elastomer micropillars.

### 2.3. Electrospinning of nanofibers

Solution of PLGA (Mw 76,000–115,000) at lactide to glycolide ratio 75:25 were prepared by dissolving PLGA in THF (with higher volatility) and DMF mixed solvent with ratio 2:3. The concentration of PLGA solution was 20 wt%. For deposition of smooth and beads-free nanofibers, ionic surfactant sodium dodecyl sulphate (SDS, Sigma, France) dissolved in ethanol was admixed into the polymer solution to a final concentration of 1 mg/ml.

The PLGA solution was kept in a 1-ml-syringe and spinneret tip that connected to the anode of a high voltage (Heinzinger, Germany) of 12 kV. The cathode was connected to the grounded aluminum wafer collector. The solution was supplied by a syringe pump (KD Scientific, USA) at a rate of 0.2 ml/h. The vertical distance between spinneret tip and the collector was 10 cm. Random PLGA nanofibers were collected for 3 min on the aluminum wafer, on which the micro pillar supporter was attached. After electrospinning, the sample was put into a vacuum chamber to volatilize the solvent overnight. As expected, we obtained a new type of culture substrate made of PLGA nanofibers on PDMS pillar arrays (Fig. 2c). By using freeware Image-J and SEM images of the fabricated samples, the diameter of the nanofibers could be measured, showing that 84.0% fibers have diameters in the range of 500–900 nm (Fig. 2d) and <0.2% (2.5%) fibers have diameters smaller (larger) than100 nm (1000 nm).

## 3. Cell culture

### 3.1. Substrate preparation

One day before cells seeding, the PLGA/PDMS and PDMS (control) microarrays were exposed to plasma treatment for 2 min and sterilized with UV light for 20 min. Subsequently, the substrates were left in ethanol 70% for 1 h and rinsed with sterile water. For the conventional and two-dimensional culture, glass coverslips (15 mm diameter) were used and dry-heat sterilized. For U87 cells, all the substrates were coated with fibronectin at 25 °C for 2 h in a fume hood, in order to improve the adhesion of cells. For hippocampal cells, all the samples were coated with 50 μg/ml poly-L-ornithine (Sigma-Aldrich, St. Louis, MO, USA) for overnight incubation at 37 °C. An additional coating with Matrigel (diluted 1:50 with culture medium; Corning, Tewksbury MA, USA) was performed on the substrates 20 min before cells plating.

### 3.2. U87 culture

U87 cells were prepared in Dulbecco's modified eagle medium (DMEM) with 10% fetal bovine serum (FBS) and 1% penicillin/streptomycin. The cells prepared in flasks were trypsinized, centrifuged and re-suspended with cell density ~104 cell/ml. 50-μl solution (cells in medium) was dropped on each substrate. After 1 h incubation for cell attachment, fresh culture medium was added and the samples were placed in an incubator (37 °C, 5% CO2).

### 3.3. Hippocampal culture

Hippocampal neurons from Wistar rats (P2–P3) were prepared in accordance with the guidelines of the Italian Animal Welfare Act, and their use was approved by the Local Veterinary Service, the SISSA Ethics Committee board and the National Ministry of Health (Permit Number: 630-III/14) in accordance with the European Union guidelines for animal care (d.1.116/92; 86/609/C.E.). The animals were anaesthetized with $CO_2$ and sacrificed by decapitation, and all efforts were made to minimize suffering. After isolation of the hippocampi, cells were enzymatically dissociated and resuspended in minimum essential medium

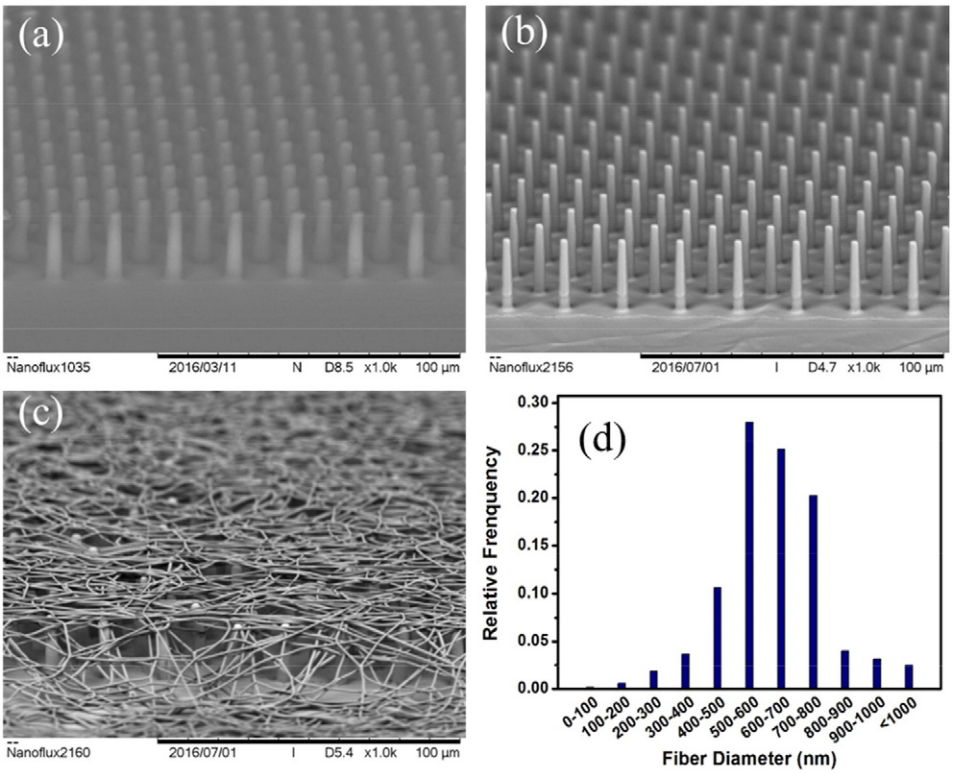


**Fig. 2.** SEM images of SU8 mold with a micropillar array (a), positive replica of the mold into PDMS (b), PLGA nanofibers electrospun on PDMS pillars (c). Statistic distribution of the PLGA nanofibers (d).

(MEM) with GlutaMAX™ supplemented with 10% dialyzed fetal bovine serum (FBS, all from Thermo Fisher Scientific, Waltham, MA, USA), 0.6% D-glucose, 15 mM Hepes, 0.1 mg/ml apo-transferrin, 30 µg/ml insulin, 0.1 µg/ml D-biotin, 1 µM vitamin B12 and 2.5 µg/ml gentamycin (all from Sigma-Aldrich). 48 h after cells' plating, half of the medium was changed with the addition of 2 µM cytosine-β-D-arabinofuranoside (Ara-C; Sigma-Aldrich). Subsequently, half of the medium was changed twice per week. The neuronal cultures were maintained in an incubator at 37 °C, 5% $CO_2$ and 95% relative humidity.

### 3.4. Immunocytochemistry and imaging

Cells were fixed in 4% paraformaldehyde containing 0.15% picric acid in phosphate-buffered saline (PBS), saturated with 0.1 M glycine, permeabilized with 0.1% Triton X-100, saturated with 0.5% BSA (all from Sigma-Aldrich) in PBS and then incubated for 1 h with primary mouse monoclonal antibodies: glial fibrillary acidic protein (GFAP, Sigma-Aldrich) and anti-β-tubulin III (TUJ1, Covance, Berkeley, CA). The secondary antibodies were goat anti-mouse Alexa Fluor® 594, goat anti-mouse immunoglobulin (Ig) $G_1$ Alexa Fluor® 488 and goat anti-mouse $IgG_{2a}$ Alexa Fluor® 594. F-actin was marked with Alexa Fluor 488® phalloidin (all from Thermo Fisher Scientific) and the incubation time was 30 min. Nuclei were stained with 2 µg/ml in PBS Hoechst 33342 (Sigma-Aldrich) for 5 min. All the incubation steps were performed at room temperature (20–22 °C). Images were acquired using a Leica DM6000 fluorescent microscope equipped with differential interference contrast (DIC) and fluorescence optics, charge-coupled device (CCD) camera and Volocity 5.4 3D imaging software (PerkinElmer, Coventry, UK). The fluorescence images were collected with a 20× and a 40× magnification (0.5 NA) objective. Image J by W. Rasband (developed at the U.S. National Institutes of Health and available at http://rsbweb.nih.gov/ij/) was used for image processing.

### 3.5. Calcium imaging

The cells were incubated with the non-ratiometric calcium dye Oregon Green® 488 BAPTA-1, AM, (Thermo Fisher Scientific) dissolved in anhydrous dimethyl sulfoxide (DMSO) (Sigma-Aldrich) at a concentration of 4 mM (stock solution), with the addition of Pluronic F-127 20% solution in DMSO (Thermo Fisher Scientific) for increasing the cell's permeability. The two components were dissolved at a ratio of 1:1 in Ringer's solution (145 mM NaCl, 3 mM KCl, 1.5 mM $CaCl_2$, 1 mM $MgCl_2$, 10 mM glucose and 10 mM Hepes, pH 7.4) to give a final dye concentration of 4 µM, and incubated at 37 °C for 1 h. The cultures were then transferred to a glass-bottom Petri dish to allow visualization in a Nikon Eclipse Ti-U inverted microscope equipped with an HBO 103 W/2 mercury short arc lamp (Osram, Munich, Germany), a mirror unit (exciter filter BP 465–495 nm, dichroic 505 nm, emission filter BP 515–555) and an Electron Multiplier CCD Camera C9100-13 (Hamamatsu Photonics, Japan). The experiments were performed at room temperature for maximally 20 min/sample. Images were acquired using the NIS Element software (Nikon, Japan) with an S-Fluor 20×/0.75 NA objective at a sampling rate of 3–10 Hz. The spatial resolution was 256 × 256 pixels. To avoid saturation of the signals, excitation light intensity was attenuated by ND4 and ND8 neutral density filters (Nikon).

As described in our previous work [20,21], the initial video was processed with the ImageJ (U. S. National Institutes of Health, Bethesda, MA) software. Briefly, neurons were localized, and an appropriate region of interest (ROI) was selected to subtract the background. Appropriate ROIs around the cells bodies were then selected and the fluorescence intensity was measured for each ROI and expressed as a function of time or If(t). Then, the dye bleaching decay was evaluated. The $Ca^{2+}$ transients of each cell signal were extracted in a semi-automatic manner by selecting a threshold for the smallest detectable peak that was equal three times the standard deviation of the baseline. Subsequently, the decay of If(t) was fitted to a cubic spline interpolating If(t) at 10 or

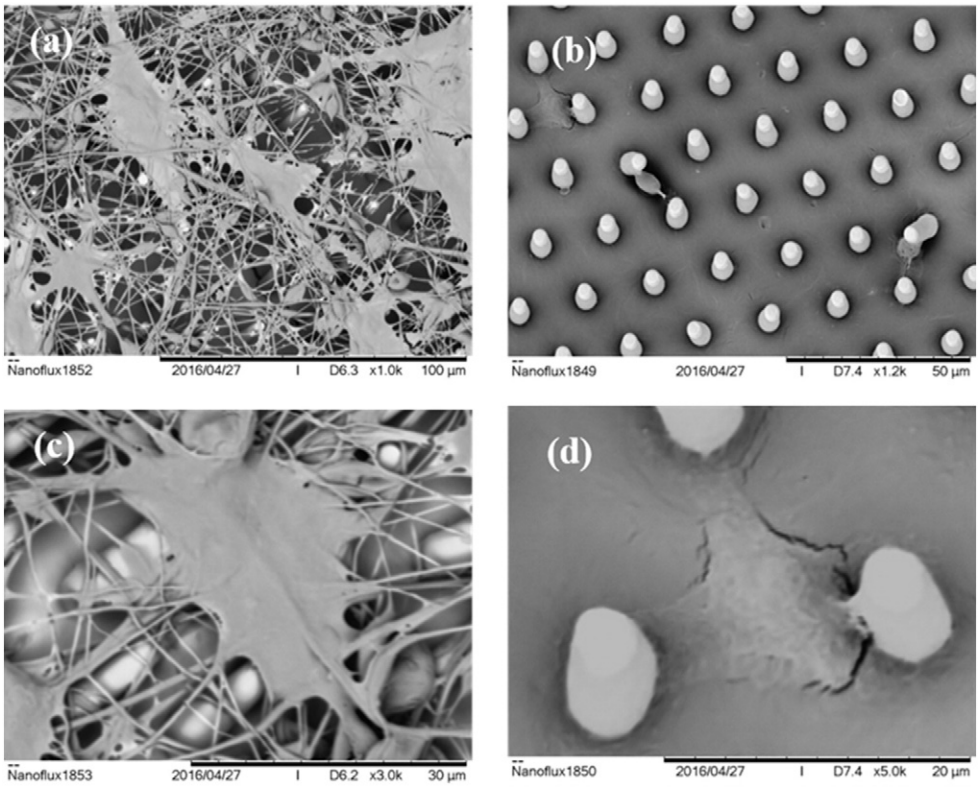


**Fig. 3.** SEM images of U87 cells cultured on a nanocomposite substrate of PLGA nanofibers on PDMS pillars (a and c) and PDMS flat layer (b and d) after 48 h incubation.

20 points. If(t) was then fitted to the original optical signal to compensate for dye bleaching, and the fractional optical signal was calculated as follows: $DF/F = (If(t) - If(t_0)) / If(t_0)$, where $If(t_0)$ is the fluorescence intensity at the beginning of the recording.

## 4. Results and discussion

As a preliminary test, the proposed substrate was used for culture of U87, a human glioblastoma cell line. Fixation of U87 cells were performed 48 h after cell seeding. Fig. 3a and c show SEM images of low and high magnitudes of U87 cells on a nanocomposite substrate of PLGA nanofibers on PDMS pillars, which are significant different from that on a substrate made of PDMS pillars alone. Clearly, cells spread over a large area on the fibers and fall down onto the bottom of pillar substrate due to relative large spacing between pillars (Fig. 3b and d). Due to the differences in supporting material, cells exhibited different behaviors in adhesion and spreading. In addition, the both sides of the cells were exposed to the culture medium in the suspended areas of the nanofibers, allowing more efficient exchange of the nutrients and metabolites of cells.

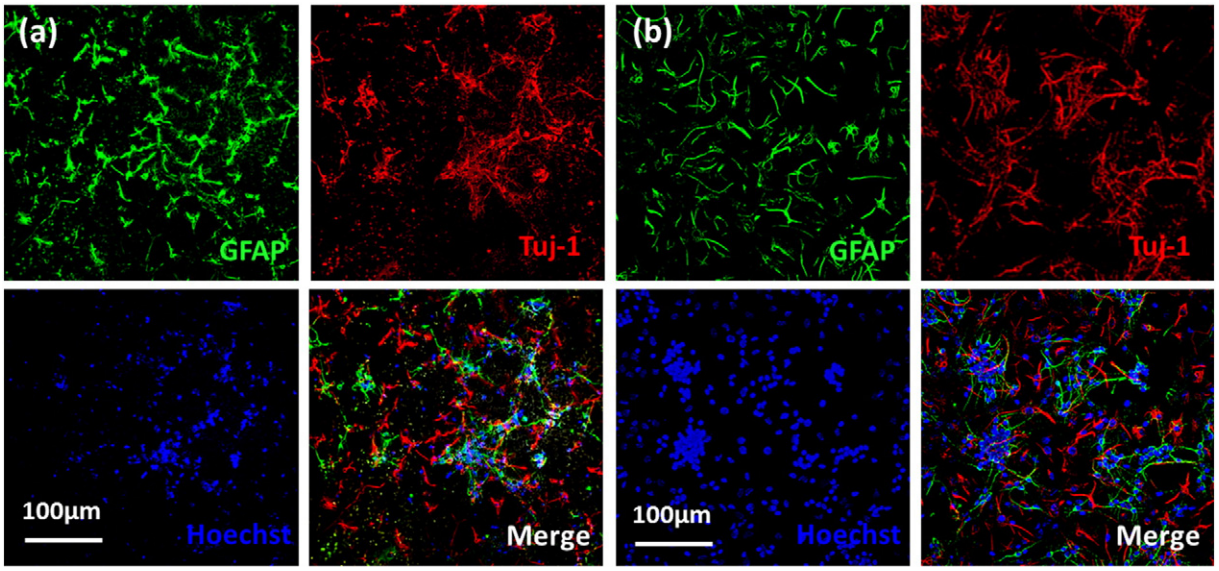


**Fig. 4.** Immunofluorescence images of neurons and astrocytes on a nanocomposite substrate of PLGA nanofibers on PDMS pillars (a) and a glass coverslip (b) after 48 h incubation. Astrocytes related glial fibrillary acidic protein is stained by GFAP (green). Neuron-specific class III β-tubulin is stained by TUJ1 (red). Cell nuclei were stained by Hoechst (blue). (For interpretation of the references to color in this figure legend, the reader is referred to the web version of this article.)

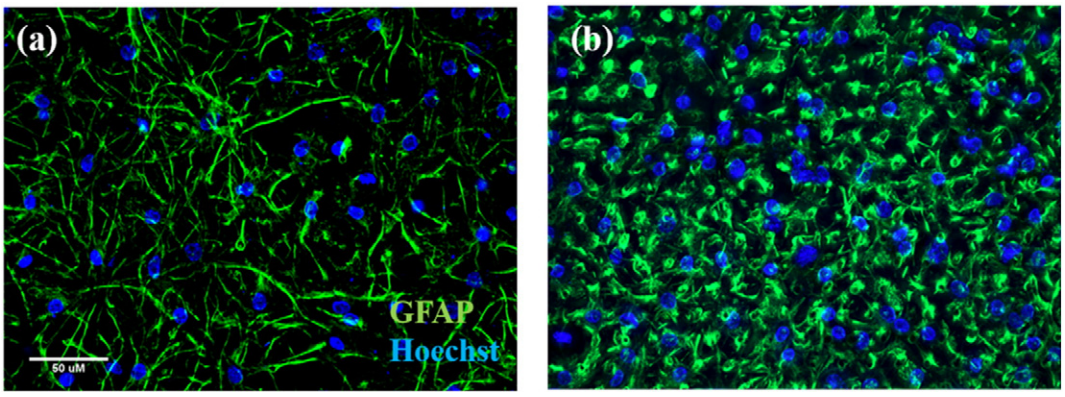


**Fig. 5.** Immunofluorescence images of astrocytes (green) on a nanocomposite substrate of PLGA nanofibers on PDMS pillars (a) and a glass coverslip (b) after one week incubation. (For interpretation of the references to color in this figure legend, the reader is referred to the web version of this article.)

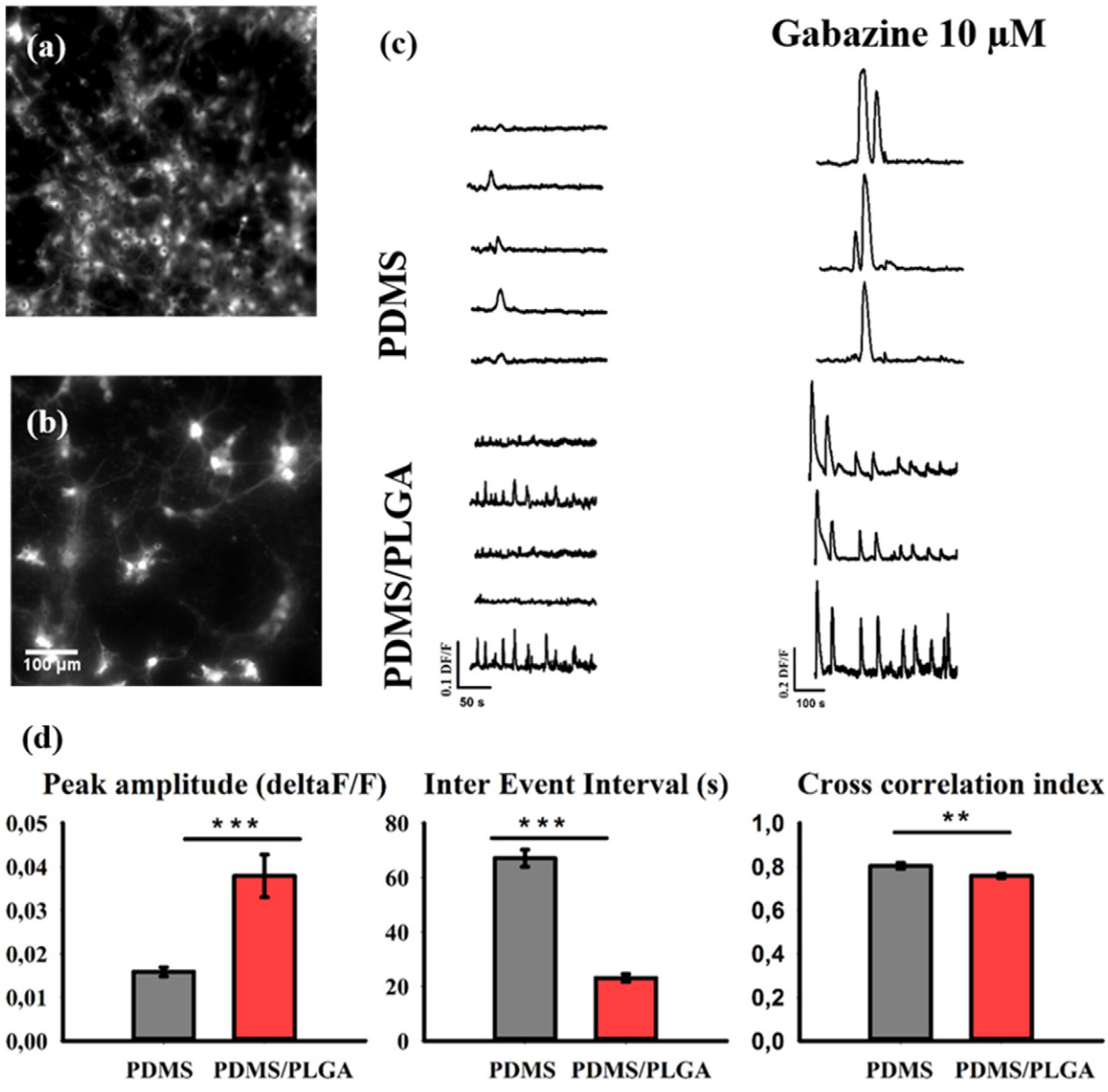


**Fig. 6.** Hippocampal neurons loaded with Oregon Green® 488 BAPTA-1, AM after two weeks of growth on PDMS (a) and PLGA/PDMS (b) substrates. Images of spontaneous and Gabazine induced calcium transients over time are also shown (c). Average amplitude, inter event interval and cross correlation index of spontaneous calcium transients on PLGA/PDMS vs PDMS substrates (n = 12 neurons for PLGA/PDMS, n = 16 neurons for PDMS - control; **p < 0.01 ***p < 0.001 One-way ANOVA, Tukey post-hoc test).

Next, primary hippocampal neurons were plated on the nanocomposite substrate of PLGA nanofibers on PDMS micropillars at a density of 300,000 cells/sample. Fixation and staining with the neuronal marker α-tubulin I, astrocytic marker GFAP and nuclear marker Hoechst were performed 48 h after cell seeding. At this stage, attachment and survival of neurons (red) and astrocytes (green) on PLGA/PDMS nanocomposite substrate (Fig. 4a) were found to be similar to that on a glass coverslip (Fig. 4b). However, after one week culture, the morphology of astrocytes plated on different types of substrates became significantly different. On the PLGA/PDMS substrate, the astrocytes showed a complex morphology with many cellular protrusions (Fig. 5a), similar to that of in vivo systems [22], whereas a flattened shape was observed for the cells on flat PDMS (Fig. 5b) [23]. This would suggest the importance of both surface morphology of the PLGA nanofibers and elastomeric material supporting and the PDMS pillars.

Once verified the neuronal attachment and survival, a functional test was performed on primary hippocampal cell cultures grown on the microarrays. The spontaneous and pharmacologically induced electrical activity of neurons was measured after two weeks of culture. At this time point, the neuronal network grown in vitro represents a mature stage of development. We chose an optical recording technique that allows the simultaneous imaging of many neurons. Specifically, we measured the fluctuations in the concentration of intracellular calcium ions by use of fluorescent calcium binding dye. Calcium ions are intracellular signals that regulate a large variety of cellular functions, such as genetic expression, neurotransmitter release and neuron-to-glia communication. The analysis of spontaneous calcium transients optically recorded from single cells allows comparing the functionality of the neuronal network grown on the PLGA/PDMS nanocomposite vs PDMS (control) substrates (Fig. 6).

On PDMS, we observed a few active neurons similar to the PLGA/PDMS substrates. Moreover, the calcium signals from glial cells were clearly visible on the micropillars, and distinguishable from neuronal signals because of their slower rates of rise and decay (Supplementary Video 1).

The average amplitude of neuronal calcium transients was significantly increased on the nanocomposite substrate vs control while the inter event interval was decreased, meaning that the neurons grown on nanofibers have more frequent and more homogeneously distributed calcium signals over time comparing to controls. The synchronization of calcium transients over time, measured as average cross correlation index, was slightly increased on PDMS (control) comparing to PLGA/PDMS as shown in Fig. 6d.

The average amplitude of neuronal calcium transients was significantly increased on the nanocomposite substrate ($0.038 \pm 0.004$ DF/F) vs control ($0.016 \pm 0.001$ DF/F); an elevation of intracellular calcium above a certain threshold is known to induce long-term potentiation of neuronal synapses [24]. The Inter Event Interval was instead decreased on the nanocomposite substrate vs control ($23.13 \pm 1.45$ vs $67.07 \pm 3.14$ s), meaning that the neurons grown on nanofibers have more frequent and more homogeneously distributed calcium signals over time comparing to controls. The synchronization of calcium transients over time, measured as average cross correlation index between all the neuronal signals in the same field of view, was slightly increased on PDMS ($0.80 \pm 0.01$) comparing to PLGA/PDMS ($0.76 \pm 0.01$) as shown in Fig. 6g.

In addition, we stimulated the neuronal cultures with Gabazine 10 μM (Sigma-Aldrich), a specific GABAA receptor antagonist, and observed an increase in the amplitude and synchronization of calcium transients in both PLGA/PDMS and PDMS (control) substrates (Fig. 6c), as expected by neuronal physiology.

## 5. Conclusion

We proposed a new type of culture substrates made of electrospun nanofibers on elastomeric micropillars. The advantage of such an approach relies on the ECM-like surface morphology and the low effective Young's module of the under layer as well as the high porosity of the fiber-pillar assembly. Our preliminary results on culture of neurons and glial cells have shown improved cell morphology and electric activity compared to other types of substrates. Our further goal is to optimize the density and the stiffness of the nanofibers for improved culture of neurons as well as control stem cell differentiation toward functional neural networks.

Supplementary data to this article can be found online at http://dx.doi.org/10.1016/j.mee.2017.01.015.

## Acknowledgements

This work was supported by Agence de Recherche Nationale under contract No. ANR-13-NANO-0011-01 (Pillarcell). J. Wei is grateful to China Scholarship Council (CSC) for grant.

## References

[1] M.P. Lutolf, J.A. Hubbell, Nat. Biotechnol. 23 (1) (2005) 47–55.
[2] P. Friedl, K. Wolf, Nat. Rev. Cancer 3 (5) (2003) 362–374.
[3] F.B. Kai, H. Laklai, V.M. Weaver, Trends Cell Biol. 26 (7) (2016) 486–497.
[4] D.A. Lauffenburger, A.F. Horwitz, Cell 84 (3) (1996) 359–369.
[5] A.D. Doyle, M.L. Kutys, M.A. Conti, et al., J. Cell Sci. 125 (9) (2012) 2244–2256.
[6] D.H. Kim, C.H. Seo, K. Han, et al., Adv. Funct. Mater. 19 (10) (2009) 1579–1586.
[7] M. Gupta, B.R. Sarangi, J. Deschamps, et al., Nat. Commun. 6 (2015) 7525.
[8] S. Megelski, J.S. Stephens, D.B. Chase, et al., Macromolecules 35 (22) (2002) 8456–8466.
[9] E.K.F. Yim, S.W. Pang, K.W. Leong, Exp. Cell Res. 313 (9) (2007) 1820–1829.
[10] J. Xie, W. Liu, M.R. MacEwan, et al., Small 7 (2011) 293.
[11] S.H. Ku, J. Ryu, S.K. Hong, et al., Biomaterials 31 (9) (2010) 2535–2541.
[12] M.A. Cole, N.H. Voelcker, H. Thissen, et al., Biomaterials 30 (9) (2009) 1827–1850.
[13] J. Fu, Y.K. Wang, M.T. Yang, et al., Nat. Methods 7 (2010) 733.
[14] A. Higuchi, Q.D. Ling, Y. Chang, et al., Chem. Rev. 113 (5) (2013) 3297–3328.
[15] Y. Sun, K.M.A. Yong, L.G. Villa-Diaz, et al., Nat. Mater. 13 (6) (2014) 599–604.
[16] Y. Tang, L. Liu, J. Li, et al., J. Mater. Chem. B 4 (19) (2016) 3305–3312.
[17] M. Schindler, I. Ahmed, J. Kamal, et al., Biomaterials 26 (28) (2005) 5624–5631.
[18] J.Y. Lee, C.A. Bashur, A.S. Goldstein, et al., Biomaterials 30 (26) (2009) 4325–4335.
[19] J. Wei, J. Shi, et al., Microelectron. Eng. 158 (2016) 22–25.
[20] M. Moshtagh-Khorasani, E.W. Miller, V. Torre, Physiol. Rep. 1 (5) (2013) e00089.
[21] F.P. Ulloa Severino, et al., Sci. Rep. 6 (2016) 29640.
[22] T.B. Puschmann, et al., Glia 61 (2013) 432.
[23] D.M. Landis, L.A. Weinstein, C.J. Skordeles, Glia 3 (1990) 212.
[24] R.A. Zalutsky, R.A. Nicoll, Science 248 (4963) (1990) 1619–1624.

# The role of network architecture in the onset of Local and Global Up states

**Diletta Pozzi [1], Nicolo Meneghetti[2], Anjan Roy[3], Beatrice Pastore[1], Alberto Mazzoni[2], Matteo Marsili[3] and Vincent Torre[1,4,5]**

[1]Neurobiology Sector, International School for Advanced Studies (SISSA), via Bonomea 265, 34136 Trieste, Italy.

[2] Computational Neuroengineering Lab, The Biorobotics Institute, Scuola Superiore Sant'Anna, Viale Rinaldo Piaggio 34, 56125, Pontedera (PI), Italy.

[3] Abdus Salam International Center for Theoretical Physics (ICTP), Strada Costiera 11, 34014 Trieste, Italy.

[4] Cixi Institute of Biomedical Engineering (CNITECH), Ningbo Institute of Materials Technology and Engineering, Chinese Academy of Sciences, Zhejiang, 315201, P. R. China.

[5] Center of Systems Medicine, Chinese Academy of Medical Sciences, Suzhou Institute of Systems Medicine (ISM), Suzhou Industrial Park, Suzhou, Jiangsu, 215123 P.R. China.

**Running Title**

Network architecture influences Up states

**Key words**

Neuronal network, calcium imaging, GABAergic neurons

**Corresponding author:**

Prof. Vincent Torre

Mail address: International School for Advanced Studies (SISSA),

via Bonomea 256,

34136 Trieste (Italy).

Email: torre@sissa.it

**Table of Contents category:** Neuroscience – Computational Physiology and Modelling

**Key point summary:**

- The spontaneous activity in cortical and hippocampal slices is dominated by the intermittency between a regime characterized by sparse and confined calcium transients, identified as the Up states, and a regime where almost the entire visualized network is simultaneously activated, referred to as the Global Up states.
- The distribution of maximal area and duration of spontaneous calcium transients follows a power law behavior, where Global Up states appear as resonances.
- The emergence of Global Up states was observed also in dissociated neuronal cultures from the same brain regions, but occurring with a shorter duration.

- Modelling with single and multi-layers neural networks suggests that the differences between native and dissociated networks are due to the peculiar cyto-architectural organization of slices, and that Global Up states could originate from long-tailed distributions of few biophysical parameters such as connectivity and the firing threshold.


## Abstract

The analysis of the spontaneous activity of neuronal networks, both in native conformation and after dissociation, clarifies the role of architecture in shaping its dynamical properties. We used calcium imaging to identify clusters of neurons co-activated in hippocampal and cortical slices, as well as in dissociated neuronal cultures, from GAD67-GFP mice. In slices, we observed intermittency between silent states (Down states), synchronous localized states (Up states), and synchronous diffused states (Global Up states). Up and Global Up states were detected as confined optical transients (COTs) in areas ranging from few tens up to 11.000 $\mu m^2$ and diffused optical transients (DOTs) invading almost the entire visualized slice. A statistical analysis indicated that Global Up states in the cortex were preferentially triggered by the activity of neurons located in layer III-IV, poorly coincident with GABAergic neurons. Global Up States had a duration of 10.2±0.3 and 8.2±0.4 seconds in cortical and hippocampal slices, respectively, and were blocked by tetrodotoxin, indicating their neuronal origin. The amplitude and duration of Global Up states were controlled by NMDA and GABA-A receptors. We next investigated calcium transients in dissociated cultures, and we observed an increased synchrony in GABAergic neurons and the presence of Global Up states but with a duration shorter than that seen in the native tissue before dissociation. We conclude that controllable Global Up States, which are likely to be a basic mechanism of information processing in the nervous system, are shaped by network architecture and balance between inhibition and excitation.


## 1. Introduction

The spontaneous electrical activity of several brain regions – and in particular of the cortex – shows rapid transitions between periods of intense and synchronous firing (Up states) and of reduced or almost absent electrical activity (Down states) (Steriade *et al.*, 1993; Timofeev *et al.*, 2001; Luczak *et al.*, 2007). These transitions have also been observed in rodents performing a variety of tasks (Petersen *et al.*, 2003; Luczak *et al.*, 2007; Vyazovskiy *et al.*, 2011; Sachidhanandam *et al.*, 2013), in monkeys (Engel *et al.*, 2016), in cortical slices (Sanchez-Vives & McCormick, 2000; Timofeev *et al.*, 2000; Cossart *et al.*, 2003; Fanselow & Connors, 2010) and when afferent cortical inputs were destroyed. These observations show that this intermittent behavior is intrinsic to the neuronal network and is not caused by the modulation of external inputs (Compte *et al.*, 2008). These transitions occur at different frequency ranges depending on the brain region: in the cerebral cortex in the range of slow oscillations (0.5 – 1 Hz) (Steriade *et al.*, 1993) whereas in the hippocampus mainly in the theta frequency range (4 – 8 Hz) (Buzsáki, 2002), and some slow oscillations are observed in the presence of a coordinated firing between the hippocampus and the cortex (Sirota & Buzsáki, 2005). In order

to explain these transitions, several models of interacting excitatory and inhibitory neurons have been proposed (Markram *et al.*, 2015) in which intermittency is explained as originating primarily from synaptic noise (Scarpetta & de Candia, 2014). In alternative models, based on simple sets of differential equations, intermittency has a more deterministic origin (Curto *et al.*, 2009; Goodfellow & Glendinning, 2013) in a way reminiscent of what observed in chaotic systems.

Spontaneous electrical activity represents the existent noise in the nervous system that affects its operation (Faisal *et al.*, 2008). Artificial computing elements, such as electronic components and devices, have a very low intrinsic noise and are almost noise-free, while the nervous system is characterized by a lot of on-going activity that constitutes the background noise in which it operates. How the brain copes with this background noise is a major issue of computational neuroscience.

In this manuscript, we aim to characterize the spontaneous electrical activity of cortical and hippocampal slices from GAD67-GFP mice (Tamamaki *et al.*, 2003) using conventional calcium imaging (Petersen *et al.*, 2003; Cossart *et al.*, 2005). In this transgenic mouse line, inhibitory GABAergic (GABA+) neurons are labeled with the green fluorescent protein (GFP) so it is possible to identify these neurons and to characterize their role. Here we aim to recover global dynamical properties of cortical and hippocampal networks and a single neuron resolution is not necessary. Therefore, we used calcium imaging with conventional wide-field fluorescence microscopy and not two-photon imaging (Yang & Yuste, 2017). In these experimental conditions, we obtained an optical trace averaged along the z-axis from which we could identify the onset of Global Up states, characterized by a diffuse synchronous activation extending in all directions.

In addition to the spontaneous activity of slices preserving their original connectivity, we analyzed calcium transients from neuronal cultures obtained after dissociation of the native cortical tissue. In these experiments, given the single layer organization of the networks under investigation, calcium transients originating from individual neurons (either GABA+ or GABA-) were unequivocally identified. Modelling with simplified neural networks shows that the dynamical differences of the spontaneous activity between slices and dissociated cultures are due to the multilayer organization of the native tissue.

## 2. Methods

*Ethical approval*

All procedures were in accordance with the guidelines of the Italian Animal Welfare Act, and their use was approved by the Local Veterinary Service, the SISSA Ethics Committee board and the National Ministry of Health (Permit Number: 2848 - III/15) in accordance with the European Union guidelines for animal care (d.1.116/92; 86/609/C.E.). The animals were anaesthetized with $CO_2$ and sacrificed by decapitation, and all efforts were made to minimize suffering.

### *2.1 Slice preparation*

Slices formed by organotypic cultures were prepared from hippocampal and cortical region of GAD67-GFP mice brain, according to the Gähwiler method (Gähwiler *et al.*, 1997). Hippocampus together with entorhinal cortex was isolated from 4-6-day-old (P4-P6) postnatal animals. The isolated tissue was cut into 350 μm thick transverse slices by means of a tissue

chopper (McIlwain, UK). The slices were placed in GBSS solution (g/l: $CaCl_2$*2H2O 0.22; KCl 0.37; $KH_2PO4$ 0.03; $MgCl_2$*6H2O 0.21; $MgSO_{4x}$*7H2O 0.07; NaCl 8; $NaHCO_3$ 0.227; $Na_2HPO4$ 0.12) added with Kynurenic acid (final concentration 1mM) and D-glucose (final concentration 28 mM), and kept at 4 degrees for 1 hour. Slices were then attached on a glass coverslip 12x24 mm (OrsaTec) with reconstituted chicken plasma (Sigma) coagulated by thrombin (200 U/ml - Merck). After coagulation the coverslips were inserted into plastic-one side flat tubes (Nunc) with 0.75 ml of medium containing 25% horse serum (Gibco), 50% basal medium Eagle (Gibco) added with L-glutamine, and 25% Hanks balanced salt solution (Gibco), enriched with glucose to a concentration of 28 mM. The tubes were kept in a roller drum rotating (10 revolutions per h), in incubator at 37 °C.
In a separate set of experiments, organotypic cultures were prepared according to the Stoppini method (Stoppini *et al.*, 1991). The procedure was identical to the Gähwiler method until the cutting and incubation in GBSS solution at 4 degrees. Slices were then placed on sterile, transparent semiporous membranes in six well multiwell (Falcon), with 1 ml of Neurobasal medium added of B27 supplement (ThermoFisher), the same medium that was used for dissociated cell cultures. The multiwell were kept in an incubator at 37 °C, with 5% of $CO_2$. In both protocols, the culture medium was changed every five days.

### *2.2 Dissociated cell cultures preparation*

Cortical and hippocampal dissociated cell cultures were prepared from GAD67-GFP mice (P0-P1). Glass coverslips (15mm diameter) were coated with 50 µg/ml poly-L-ornithine (Sigma-Aldrich, St. Louis, MO, USA) overnight, and just before cells' seeding, a thin layer of Matrigel (diluted 1:50 with culture medium; Corning, Tewksbury MA, USA) was applied. The cortex and hippocampus were isolated and dissected separately. In both cases, the cultures were prepared at two different cell's concentrations. After enzymatic and mechanical dissociation, cells were resuspended at a concentration of $1(2)*10^6$ cells/ml in minimum essential medium (MEM) with GlutaMAX$^{TM}$ supplemented with 10% dialyzed fetal bovine serum (FBS, all from Thermo Fisher Scientific, Waltham, MA, USA), 0.6% D-glucose, 15 mM Hepes, 0.1 mg/ml apo-transferrin, 30 µg/ml insulin, 0.1 µg/ml D-biotin, 1 µM vitamin B12 and 2.5 µg/ml gentamycin (all from Sigma-Aldrich). Cells were then plated at a density of 500(1000) cells/mm$^2$ on glass coverslips. After incubation for 30 min at 37°C, the growing medium was added consisting of Neurobasal medium supplemented with B27, GlutaMAX$^{TM}$ and 2.5 µg/ml gentamycin (all from ThermoFisher). Half of the medium was changed after 48 h adding 2 µM cytosine-β-D-arabinofuranoside (Ara-C; Sigma-Aldrich). The neuronal cultures were maintained in an incubator at 37°C, 5% $CO_2$ and 95% relative humidity. Half of the medium was again changed once per week.

### *2.3 Calcium imaging*

Calcium imaging experiments on organotypic slices were performed using the Rhod-3 Calcium Imaging Kit (Thermo Fisher) for non-ratiometric analysis. According to the manufacturer's instructions, the samples were incubated for 45' at r.t. in Ringer solution (145 mM NaCl, 3 mM KCl, 1.5 mM $CaCl_2$, 1 mM $MgCl_2$, 10 mM glucose and 10 mM Hepes, pH 7.4) containing the red-fluorescent dye at a concentration of 10 µM.
Calcium imaging experiments on dissociated cell cultures were performed using the non-ratiometric calcium-binding dye Fura Red, AM (Thermo Fisher), since we observed frequent cells' toxicity when incubating dissociated neurons with Rhod-3. The samples were incubated for 45' at r.t. in Ringer solution (145 mM NaCl, 3 mM KCl, 1.5 mM $CaCl_2$, 1 mM $MgCl_2$, 10 mM glucose and 10 mM Hepes, pH 7.4) containing the red-fluorescent dye at a concentration

of 5 μM. Pluronic F-127 20% solution in dimethyl-sulfoxide (Thermo Fisher Scientific) was added at a ratio 1:1 with the dye for increasing cells' permeability.
After incubation, both type of samples were transferred to a glass-bottom Petri dish in order to allow visualization in a Nikon Eclipse Ti-U inverted microscope equipped with an HBO 103 W/2 mercury short arc lamp (Osram, Munich, Germany), a mirror unit (exciter filter BP 465-495 nm, dichroic 505 nm, emission filter BP 515-555) and an Electron Multiplier CCD Camera C9100-13 (Hamamatsu Photonics, Japan). Images were acquired using the NIS Element software (Nikon, Japan) with an S-Fluor 20x/0.75 NA objective and 512x512 spatial resolution. To avoid saturation of the signals, excitation light intensity was attenuated by ND4 and ND8 neutral density filters (Nikon).
Cortex and hippocampus of a same slice were imaged subsequently. Given the slow time course of measured calcium transients, an acquisition rate of 3 - 10 Hz was found to be adequate. In some control experiments, we reached an acquisition rate of 50 Hz by increasing the intensity of the illuminating light and the binning of pixels; in this case, the total recording time was 5 minutes. During our optical recordings some dye bleaching occurred and the exponential decline of the basal fluorescence was corrected with our custom-made software.

### *2.4 Data Analysis*

#### *2.4.1 Preprocessing of image sequences*
The pre-processing of the acquired videos consisted in two steps. First, we removed the bleaching – driven drift in the z-profile's baseline via linear de-trending. The drift has been corrected by interpolating the points belonging to the baseline in order to get a function $z_{(t)}$: then every i-th frame has been multiplied by $z_{(0)}/z_{(i)}$. This operation was performed image-wise (i.e., the videos' z-profile has been computed as the mean intensity value of each frame) for control recordings and pixel-wise (i.e., the bleaching has been corrected considering the intensity profile of each pixel separately) for TTX-APV recordings. Second, we measured the changes in fluorescence intensity over time ($\Delta F/F_{(0)}$) using the open source ImageJ plugin dFoFmovie-CatFullAutoSave.ijm (https://gist.github.com/ackman678/11155761).

#### *2.4.2 Image sequence analysis*
We identified the activity *events* as follows. The first step was to binarize each image with a thresholding procedure defining the active pixels in each image. Thresholds were manually set by the experimenter. Then we defined as event a region of contiguous active pixels larger than 16 $\mu m^2$.
Two events sharing pixels in consecutives frames are considered to be the same event propagating through time. We define event-splitting when in the *n+1* frame there are two (or more) "descendants" events whose areas overlap with the area of a single event in the *n* frame. We define events-merging when, in the when in the *n+1* frame, there is one event whose area has an overlap with the area of two (or more) "ancestors" events in the *n* frame.
Once the events were identified, we computed and analyzed two features: the events duration and the maximal area reached by the event during its lifetime. The event duration is the time from the birth and the death of the event, i.e., the first and last frame in which its area was above threshold. In case of splitting, death is defined as the frame in which the last sub-event dies, and in case of merging birth is the frame in which the first of the two originating events was born. The maximal of the area is the maximum value (as number of $\mu m^2$ occupied) reached by an event, considering all ancestor and descendants. We define at this stage "Global up states" the events whose maximal area exceeds half of the area of the slice under investigation, and all

the other events as "Local up states". Probability distribution of duration and area of Local up states are defined with an exponential binning and fit with a power law distribution. We used n_bins=12 for the events duration distribution, and n_bins=42 for the events area distribution, but the number of bins has a minimal effect on duration power law and no effect on area power law (see **Supplementary Figure 2**, for review only, *ndr*).
The TTX-related image sequences have undergone an additional frequency analysis step, in order to test whether their activity time scales slowed down compared to controls. Using a binary grid of Regions Of Interest, the intensity profile of every region across frames was extracted, and we computed the fast Fourier transform of each profile. After averaging over the FFT-transforms of the profiles of different ROIs, the result has been filtered with a Moving Average Filter of order n=5 using the Matlab built-in function *filtfilt*.

### *2.4.3 Computation of correlation coefficient of optical signals*

The correlation coefficient $\rho(t)_{Peak}$ between peaks of calcium transients was computed as follows. The times, $t_i$, at which transient peaks occurred are presented in a conventional raster plot. The raster plot for neuron *i* and neuron *j* ($\rho(t_{ij})_{Peak}$) was computed by dividing the total recording time into intervals of 1 or 10 s. Thus, if $f_{in}$ and $f_{jn}$ are the number of calcium transients of neuron *i* and neuron *j* in the time interval $\Delta t_n$ , $\rho(t_{ij})_{Peak}$ is computed as follows:

$$\rho(t_{ij})_{Peak} = \frac{\sum_n f_{in} f_{in}}{\sqrt{(\sum_n {f_{in}}^2)(\sum_n {f_{in}}^2)}}$$

### *2.4.4 Statistical analysis*

Data are shown as the mean ± standard error of the mean from the number of samples indicated in each experiment (see **Results** and figures captions). Distributions of data from two different data series were compared using the nonparametric Kruskal-Wallis test. The distance between experimental distributions and the corresponding theoretical binomial distributions was calculated using the nonparametric Kolmogorov-Smirnov test. The mean values from two data series were compared with One-Way ANOVA test. All statistical tests were performed using Matlab software.

## *2.5 Neural modelling*

We have developed highly simplified models of neural networks interacting in a single layer. From these models, we extended the modelling to multilayer networks. One key ingredient of these models is the presence of long-tailed distributions - more precisely, distributions with a power law behaviour. Let us discuss the technicalities of these models.

### *2.5.1 Single Layer models*

We model the system as a network of N neurons, where each neuron is connected to NC neighboring neurons (**Fig. 10A**). At each simulation time step, one unit of charge is added to a randomly selected neuron. Every neuron is assigned a threshold potential for firing $V_{th}$, drawn from a probability distribution $\rho(V_{th})$. As long as the total charge in the neuron is less than its threshold, the neuron remains silent. However, as soon as the threshold is reached the neuron "fires". We have studied two classes of models, characterized by the way the firing neuron

perturbs its neighbours. In Model 1, the firing neuron distributes all its charge randomly among its NC neighbours, while in Model 2 the firing neuron gives the same fraction of its charge $\varphi$ to its NC neighbours and resets its own charge to zero. Upon firing, its threshold is reset by drawing it at random from $\rho(V_{th})$. In turn, if some of these neighbours reach their corresponding threshold as a result of the input from the firing neuron, they fire as well, which means that they transfer charge to their neighbours as per Model 1 or Model 2 and reset their charge and thresholds. This continues untill no neuron remains which has charge above its threshold. Hence firing of a given neuron may start an avalanche of firings which propagates through the network. All these relaxations happen instantaneously in the simulation time frame. At the next time step, a new attempt to add a charge to another randomly chosen neuron is made and the process goes on. In order to have a stationary state we also introduce dissipation of the charge: With probability $\lambda$ all of the charge of the firing neuron is removed from the network, instead of being distributed to its neighbours. Since dissipation reduces the amount of excitation, we can consider it as a simplified form of inhibition, caused either by the network inhibition or by an intrinsic adaptation/inactivation.

We define the size of an avalanche (s) as the number of firing events involved in a given avalanche, and the volume of the avalanche (v) as the number of distinct neurons taking part in it. We find that if the threshold is constant or if $\rho(V_{th})$ is Gaussian, then the resulting distribution of size of avalanche follows a power law $s^{-\tau}$ with $\tau < 2$. In that case, avalanches of all sizes are possible in the network and the network can always distribute all its charge without requiring a global event involving the entire network. However, if $\rho(V_{th})$ has a long tailed distribution such as a power law ($\rho(V_{th}) \sim Vth^{-\alpha}$, with $\alpha < 2$), we again obtain a power law distribution for the size of avalanche, but now with $\tau > 2$. In this case, an average avalanche size for the network exists and if the dissipation $\lambda$ is very small then the network produces or needs a global event to relax. **Fig. 9C** shows these results for a network with N = 10.000 neurons and the global events appear as spikes at v = N for Model 1 while for Model 2 as a peak near the system size. The global event occurring in these models correspond to the experimentally observed diffuse optical transients, here referred as DOTs (see **Results**, **Fig. 1-4**).

For both models, we have also studied variations where NC is power law distributed or the number of neurons perturbed at each time step is random. These variations did not change the results as far as the power law and the resonance is concerned. However, as expected, adding charge to multiple neurons at each time step increases the frequency of the avalanches.

*2.5.2 Multilayer models*

In order to explore the reason for the broader width of the DOTs in the cortex, we extend the above model to a multilayer model. In the multilayer model, each layer has a similar structure as in the previous model, but now every neuron in each layer also has one connection to a neuron in the next layer (**Fig. 9E**). Following the same rules as for the single layer case, a neuron transfers its charge randomly among its NC neighbours in the same layer and one neighbour in the next layer. After the stability of all neurons in a layer is confirmed like in the single layer case, we check for unstable neurons in the next layer and continue this process. Note that all this sequence happens at the same simulation time step, before some charge is

added to another random neuron. However, we assume that the relaxation in subsequent layers happen with a time delay $\Delta\tau$ and we used it while plotting the time series. In **Fig. 10F** and **10I** we show that indeed a broad DOT, reminiscent of the structure observed in experiments, can appear in such a simple cyclic multi-layer model. This happens because of multiple simultaneous DOTs appearing in the different layers but with a time delay $\Delta\tau$. These DOTs appear in a cyclic fashion; a DOT appearing in any of the layer triggers a DOT in the next layer and it continues through the consecutive layers till all the unstable neurons relax, either by transferring their charge or by dissipating them. The quantity $\Delta\tau$ is ad-hoc in the current analysis and indicates the existence of functional layers interacting with each other with a time delay. In simulations, its exact value can be adjusted, along with the number of neurons perturbed at each time step, in order to obtain a time series reminiscent of the one observed in experiments.

## 3. Results

The mouse cortex is composed by 6 layers (LI-VI) and is approximately 500-1000 μm thick (**Fig. 1A**) depending on the region(Regad *et al.*, 2009). The most superficial layer (LI) is 50-80 μm thick and is primarily composed by GABA+ neurons, while excitatory neurons are located in layers II-VI (see for a review(Douglas & Martin, 2004)). The hippocampal system consists of the dentate gyrus (DG), the four regions of the cornu ammonis (CA1-3) fields and the subiculum (Sub) (**Fig. 4A**). Our imaging experiments were performed with a 20X objective in areas corresponding to cortical layers I-IV (**Fig. 1B**) and hippocampal CA1-3 (**Fig. 4B**), all of them expressing GABA+ neurons (**Fig. 1C**, **4C**).

The slices were prepared from the medial temporal lobe overlying the hippocampus, corresponding to the enthorinal cortex, maintaining the native connectivity between the two regions. In a separate set of experiments instead, the cortex and hippocampus from the same slice were mechanically separated. After 1 or 2 weeks of culture, a thickness of 70-100 μm was measured (see **Supplementary Figure 1**, for review only, *ndr*) corresponding to approximately 5-10 cellular layers. When imaging the slices with a conventional epi-fluorescence microscope, the identification of calcium transients at the single cell level was distorted – at some extent – by the light scattering from nearby focal planes. Nonetheless, we were able to identify the emergent collective properties of the cortical and hippocampal networks.

### *3.1 The spontaneous activity in cortical networks*

Slices were stained with the fluorescent Calcium indicator Rhod 3 – AM (**Fig. 1B**). The spontaneous activity was recorded by measuring optical transients using a high resolution and high sensitivity EM-CCD camera (**Supplementary Video 1**) acquiring images at 5-50 Hz. The total recording time for each session varied from 10 up to 40 minutes and, during this time, the emitted fluorescence $F_{(t)}$ could decrease by 10-30 %, because of dye bleaching. Following correction for the bleaching, the fractional optical signal $\Delta F/F_{(0)}$ was computed (**Supplementary Video 2**), assigning t=0 at the beginning of the recording, from the entire imaged slice (blue trace in **Fig. 1D**) and therefore referred as $\Delta F/F_{network}$. In addition, $\Delta F/F_{(0)}$ was computed from regions of interest (ROIs) corresponding to active cortical areas comprising both GABA+ and GABA- neurons (colored traces in **Fig. 1D**). We observed confined optical transients (COTs) in areas ranging from few tens (corresponding to 1-5 cells) up to 11.000 $\mu m^2$ (see areas inside red circles in **Fig. 1E**). Moreover, we observed diffused optical transients (DOTs) which invaded almost all layers of the visualized slice (**Fig. 1F**) with a frequency varying from 0.2 to 4 per minutes. After computing the $\Delta F/F_{network}$, DOTs appear as large peaks with a fast rising time, which was in the order or below our recording time resolution (20-200 ms).

The distribution of the maximal area of observed optical transients (COTs and DOTs) was broad and exhibited a power law behavior over almost 3 log units (**Fig. 1G**), with an average slope of -2.24 ± 0.27 (see **Table 1** in section 3.3). The power law behavior was observed also when the threshold for the detection of the COTs and the binwidth used to construct the distribution were varied (see **S2**). The duration of COTs had a power law distribution as well (**Fig. 1H**) but with a slightly lower slope (-1.87 ± 0.22, **Table 1**). In 22 out of 27 slices analyzed, the distribution of maximal areas had a resonance corresponding to the occurrence of DOTs (see the arrows in **Fig. 1G**). The number of distinct COTs observed in the same frame fluctuated in time around a mean value of 30 (**Fig. 1I**). During the appearance of a DOT the number of COTs drastically decreased and increased again at

the DOT termination, when the diffuse activation - invading almost the entire slice - broke in several smaller active regions (**Fig. 1I**, inset).

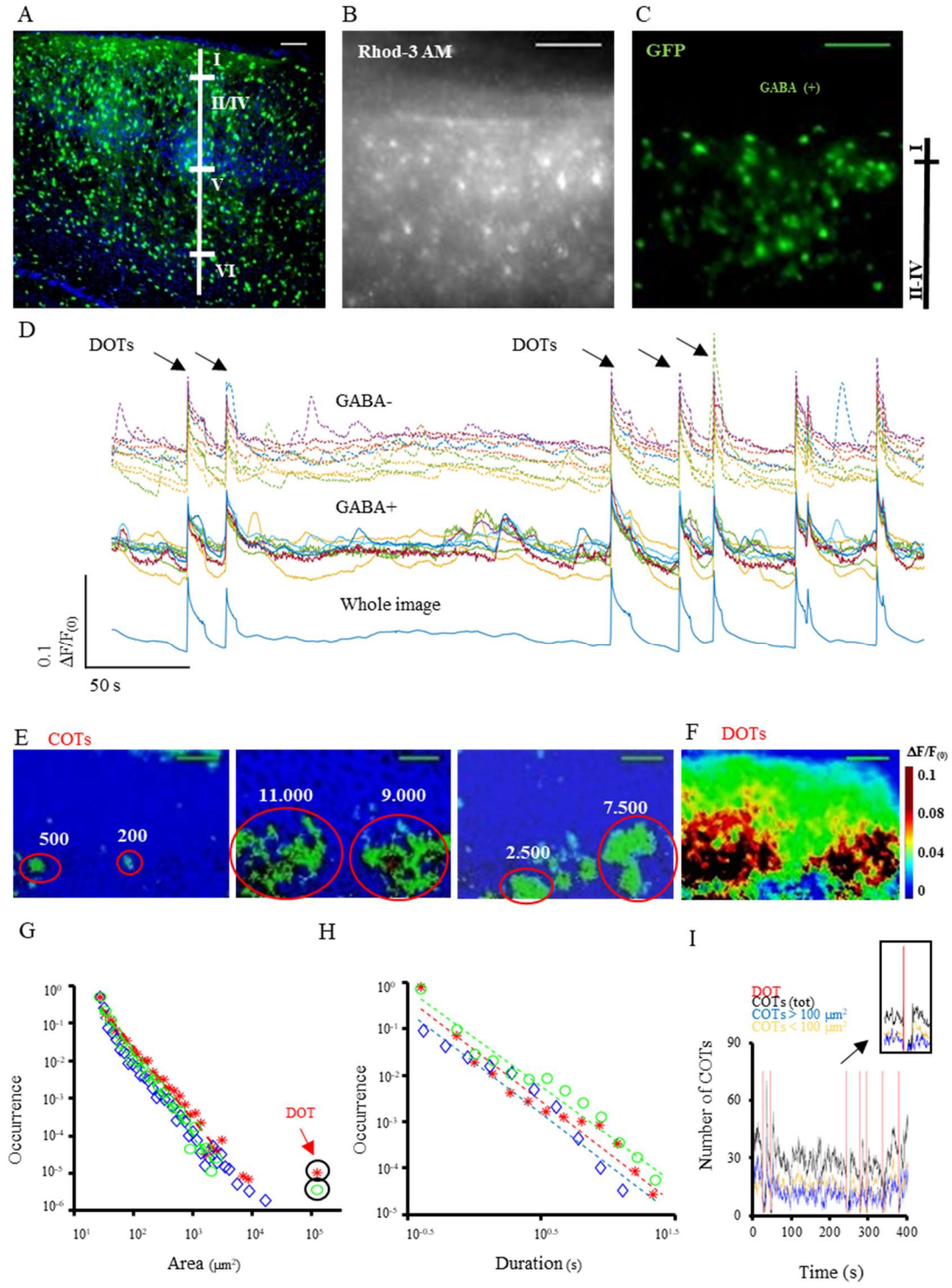


**Figure 1: Spontaneous calcium transients in the cortex. (A)** Fluorescent image of cerebral cortex from a GAD67-GFP mouse (P5) with DAPI nuclear staining; GABA+ neurons are labeled in green. The white vertical bar indicates the putative layers. **(B)** Organotypic slice from the same mouse line loaded with the fluorescent indicator Rhod-3 AM during calcium imaging, and corresponding GABA+ neurons **(C)** in the same field of view. The black vertical bar on the right indicates the approximate limits of cortical layers in this example. **(D)** $\Delta F/F_{(0)}$ traces from the whole image (blue trace at the bottom) and from selected GABA+ (colored traces in the middle) and GABA- neurons (colored traces on top) from a calcium imaging recording. **(E)** Examples of Confined Optical Transients (COTs) from the pseudo-color $\Delta F/F_{(0)}$ movie of the recording, showing isolated regions of variable sizes (see red circles; the rounded numbers are expressed in $\mu m^2$). **(F)**

Example of Diffuse Optical Transient (DOT), where the increase in $\Delta F/F_{network}$ involves more than 50% of the imaged slice. Color bar on the right. Scale bars: 80 μm in both fluorescence and pseudo-color images. **(G, H)** Probability distribution of area and duration of COTs in the cortex. Circles, rhombus and asterisks represent data from three representative experiments: the corresponding dotted lines in (H) show the linear fitting for each distribution. DOTs are visible as resonances outside the area's distributions (see black circles). **(I)** Density of COTs over time for different area sizes (COTs<100 $\mu m^2$ and COTs>100 $\mu m^2$, yellow and blue line respectively) and for all sizes (black line) with reference to DOTs occurrence (red vertical lines). The inset shows the decrease in COTs density corresponding to DOTs' occurrence.

### *3.2 Origin of COTs and DOTs*

Recorded optical transients (both COTs and DOTs) could originate from neurons and/or glial cells. In order to evaluate the contribution of glial cells, we compared optical transients before and after the addition of 1 μM tetrodotoxin (TTX), a well-known blocker of neuronal activity(Narahashi *et al.*, 1964; Gilbride, 2016). The application of TTX completely abolished DOTs in cortical slices (**Fig. 2A**), but residual optical transients could be still detected. However, these transients had a slower rising phase and time course, as demonstrated by the computation of the power spectrum density PSD: in the presence of TTX, the PSD did not extend above 0.15 Hz while in control the PSD had components above 0.4 Hz (**Fig. 2B**). Moreover, when the distribution of maximal areas of events in TTX was subtracted to that observed in control (Con) conditions, the resulting distribution was very similar to that seen prior to subtraction, as well as the number of events detected (**Fig. 2C**). For these reasons, we concluded that the large portion of calcium transients observed in control conditions originates primarily from firing neurons and only at a minor extend from glial cells. We cannot exclude, however, the contamination from slow calcium waves driven by metabotropic glutamate receptors present both in neurons and glial cellsv(Tamura *et al.*, 2014). COTs (**Fig. 1I**) are likely to originate from ensemble of neurons in a usual Up states and indeed their duration (**Fig. 1H**) varying from less than 1 sec up to 50 sec matches with that reported for Up states (Cossart *et al.*, 2005). Therefore, we identify COTs as the Up states observed in these electrophysiological investigations.
After application of the GABA-A receptors antagonist bicuculline 50 μM in cortical slices, the size and duration of DOTs visibly increased (**Fig. 2D**). As opposite, the amplitude and duration of DOTs were significantly reduced by the application of 50 μM APV (**Fig. 2E**, **F**), suggesting that DOTs originate primarily from the activation of NMDA receptors (Cossart *et al.*, 2003; Mazzoni *et al.*, 2007). The distribution of maximal areas of events (**Fig. 2G**) were similar in control conditions and in the presence of APV. Therefore, the activation of NMDA receptors is not the main mechanism causing COTs and that the activation of kainate and AMPA glutamate receptors, together with persistent sodium currents plays an important role (Mao *et al.*, 2001; Piet & Jahr, 2007; Rojas *et al.*, 2013). All these experimental observations show that DOTs exhibit a pharmacology very similar to that of usual Up states (Sanchez-Vives & McCormick, 2000; Sengupta & Thirumalai, 2015) and DOTs appear as resonances in the distribution of the maximal area of optical transients (See **Fig. 1G, H**). For these reasons, DOTs are referred as Global Up states.

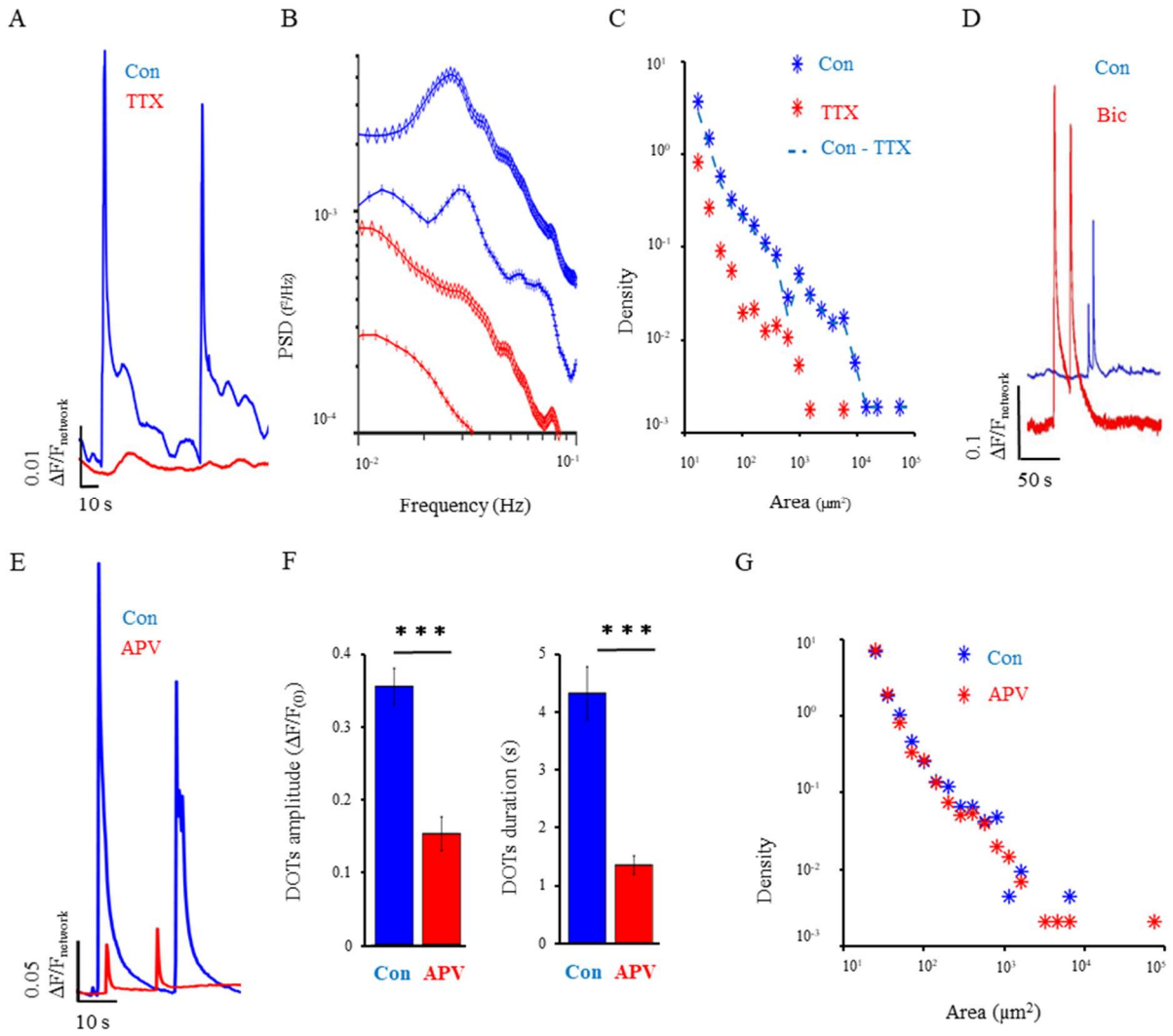


**Figure 2: Blockade of voltage – gated sodium channels (by TTX) and glutamate NMDA receptors (by APV) on cortical slices. (A)** DOTs observed in control conditions (blue trace) are abolished in the presence of 10 µM TTX (red trace), as shown by the computation of $\Delta F/F_{network}$. **(B)** Power Spectrum Density (PSD) computed as the average PSD of optical recordings from small regions corresponding to GABA+ neurons in control (blue traces) and in TTX (red traces) from two representative experiments (rhombus, 41 GABA+ neurons; crosses, 37 GABA+ neurons). **(C)** Density vs area of events in control (blue marks), in TTX (red marks) and in control-TTX (blue dotted line) in one experiment. From three representative experiments: n=16714 events detected in Con, n=14007 in Con-TTX; n=68948 in Con, n=53566 in Con-TTX; n=32312 in Con, n=21586 in Con-TTX ($p>0.05$ in all three cases, Kruskal-Wallis test). **(D)** $\Delta F/F_{network}$ in control conditions (blue trace) and after application of Bicuculline 50 µm (red trace). **(E)** $\Delta F/F_{network}$ in control conditions (blue trace) and after application of APV 50 µm (red trace). **(F)** Average amplitudes and duration of DOTs in control (blue bars) and in APV (red bars): $0.34 \pm 0.03$ $\Delta F/F_{(0)}$ and $4.33 \pm 0.49$ s for control, $0.15 \pm 0.02$ $\Delta F/F_{(0)}$ and $1.32 \pm 0.16$ s for APV. These average values were obtained from 3 experiments in control and APV conditions, subsequently: n = 32(3) DOTs(slices) for control, n=45(3) DOTs(slices) for APV.** $p < 0.001$ Kruskal Wallis test. **(G)** Density vs area of events in control (blue marks) and in APV (red marks) in a representative experiment.

Optical recordings of DOTs have a sharp rising phase, reminiscent of the rising phase of an action potential in a single neuron. An action potential in a neuron occurs when the summation of synaptic inputs reaches a threshold and a regenerative mechanism is activated. It is conceivable, therefore, that DOTs occur when the overall neuronal activity reaches a given threshold and a regenerative mechanism – operating at the network level – causes a Global Up state(Parga & Abbott, 2007). There is also a possible alternative possibility: the appearance of DOTs is favored or triggered when specific clusters or sets of neurons are activated. In order to test this possibility, we investigated whether DOTs are initiated by the *activation of privileged/specific regions* – which we refer as starters – or instead their appearance depends on the activation of enough neurons *randomly* distributed in the slice. In the first case, a statistical analysis could reveal the existence of "starters", i.e. of cortical regions whose activation is more likely to trigger or precede a DOT, in the latter case the appearance of a DOT is caused by the concomitant occurrence of a sufficient number of random events. In order to obtain an adequate statistical verification, we prolonged our imaging experiments to 30-40 minutes and occasionally up to 1 hour, so to observe several tens of DOTs. In experiments using two-photon microscopy, the temporal resolution and sensitivity are limited by the inverse relationship between the number of voxels scanned per second and the signal collected per voxel in the same time (Garaschuk *et al.*, 2000; Yang *et al.*, 2016), limiting a statistical characterization of events occurring with a frequency of less than 0.1- 1 s. In our long recordings, some bleaching occurred which was compensated and the stained slice exhibited optical transients with the same frequency and amplitude during the total observation time (**Fig. 3A**). All the frames before the occurrence of the DOT were analyzed, and each pixel was binarized with a threshold corresponding to the 30% of the maximal $\Delta F/F_{network}$, so to obtain a map of the seeds of the DOTs (**Fig. 3B**). If these seeds do not have any significant spatial correlation, than the origin of DOTs is random, but if these seeds exhibit some correlation than the existence of starters of DOTs finds some support.

We calculated the spatial overlap between these seeds and we colored the pixels according to their frequency of appearance in the seeds, with red and dark red indicating a high appearance (**Fig. 3C**). If a pixel participated to a seed in a random way, its statistics is expected to follow a binomial distribution $P(\pi,x,N)$ (Wadsworth & Bryan, 1960): in this case if $\pi$ is probability of pixel to be active, the probability P of $x$ occurrence in series of $N$ trials is:

$$P(x) = \frac{N!}{x!\,(N-x)!}\pi^x(1-\pi)^{N-x}$$

If the frequency of occurrence of pixels in the seeds follows the binomial distribution, than DOTs have a random origin, but if a given pixel occurs in the seeds more often than expected from the binomial distribution, then we can consider it as a starter. We found that red pixels in **Fig. 3C** occurred in seeds more often than expected by the binomial distribution in 6 out of 7 experiments (**Fig. 3D, E**; $p<0.001$ two-sample Kolmogorov-Smirnof test) and therefore are candidates to be starters of the DOTs. These starters had a minimal spatial overlap with GABA+ neurons (**Fig. 3F**). A preferential localization at 200-300 μm in depth from the outer most layer was observed, which corresponds approximately to layer III (**Fig. 3G**).

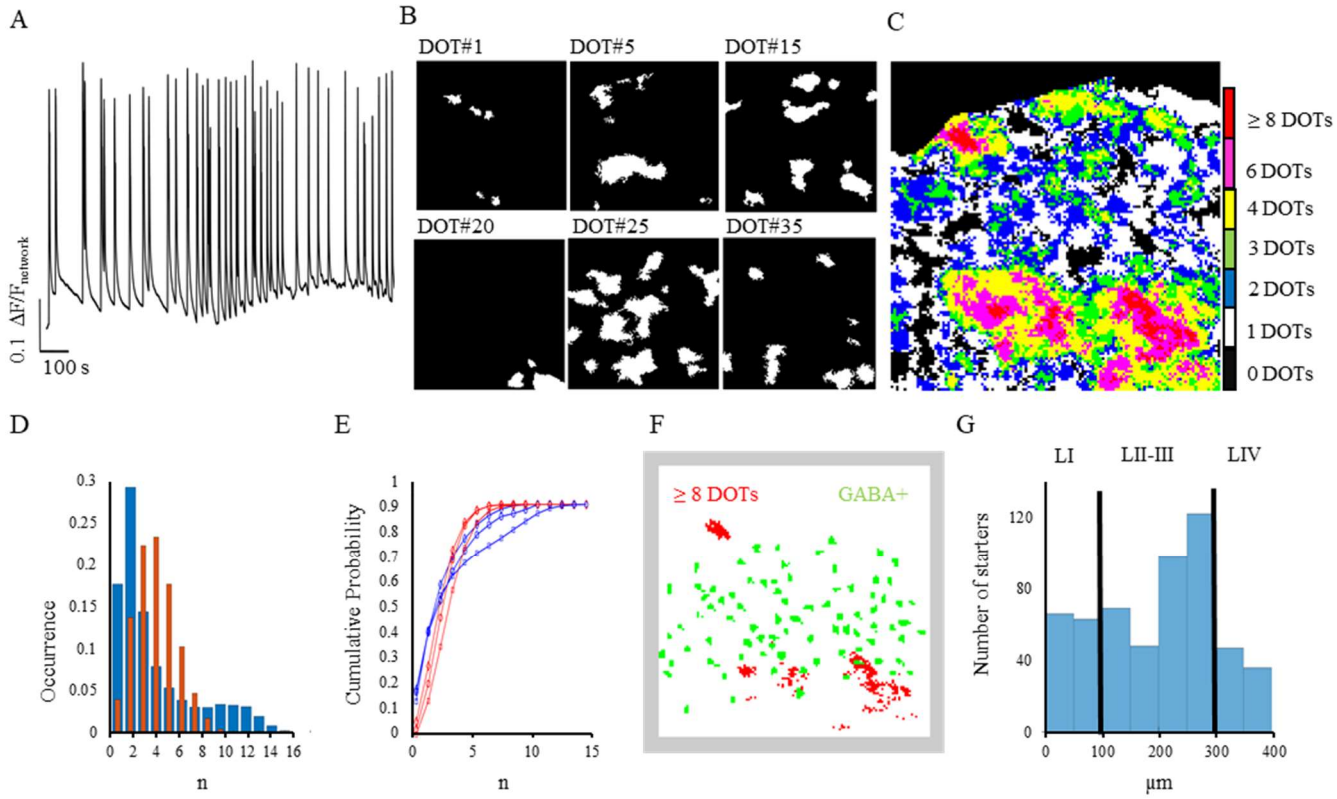


**Figure 3: Regions initiating DOTs in cortical slices**. **(A)** $\Delta F/F_{network}$ of a representative 20 min recording **(B)** Binary images of some representative seeds regions identified 200 ms before 6 randomly selected DOTs (out of a total of 35). The threshold selected was $\Delta F/F_{(0)}$ of the maximal intensity recorded. **(C)** Sum of all binary images corresponding to seeds; different colors indicate regions activated before multiple DOTs (see color bar on the right: red regions are activated before the onset of 8-11 DOTs). **(D)** Probability of activation of a pixel from experimental data compared to a binomial distribution in one experiment (blue and red bars, respectively). The x – axis represents the number of trials (frames) considered. **(E)** Cumulative probability of pixel activation from experimental data (blue lines) compared to the corresponding binomial distributions (red lines) in three representative experiments. The two distributions were significantly different ($p < 0.001$ two-sample Kolmogorov-Smirnof test). **(F)** Regions activated before the occurrence of 8-11 DOTs out of 35 (red pixels) with reference to the location of GABA+ neurons in the slice (green pixels). **(G)** Distribution of starters location among cortical layers. n = 7 slices. The density is higher between LII and LIII.

### *3.3 COTs and DOTs in hippocampal networks: origin and comparison with the cortex*

We analyzed the spontaneous activity in the hippocampal region of our slices, stained with Rhod-3 AM (**Fig. 4B**) and expressing GABA+ neurons (**Fig. 4C**). Similarly to what observed in cortical slices, calcium optical transients from hippocampal slices exhibited intermittency between DOTs and COTs (**Supplementary Video 3**, **4**; see optical traces in **Fig. 4D**). As in cortical slices, COTs had a variable area varying from few tens up to more than 10.000 $\mu m^2$ (**Fig. 4E**), while DOTs extended over more than half of the imaged field of view (**Fig. 4F**). The distribution of measured maximal areas had a power law distribution over 3 logarithmic units, with a resonance corresponding to the DOTs in 18 out 22 slices analyzed (**Fig. 4G**). The distribution of COTs durations followed a power law distribution (**Fig. 4H**) with a smaller slope (average slope = -2.04 ± 0.35 for area, -1.94 ± 0.21 for duration, see **Table 1**). The number of COTs detected simultaneously at each frame fluctuated in time in a way similar to what observed in the cortex (**Fig. 4I**).

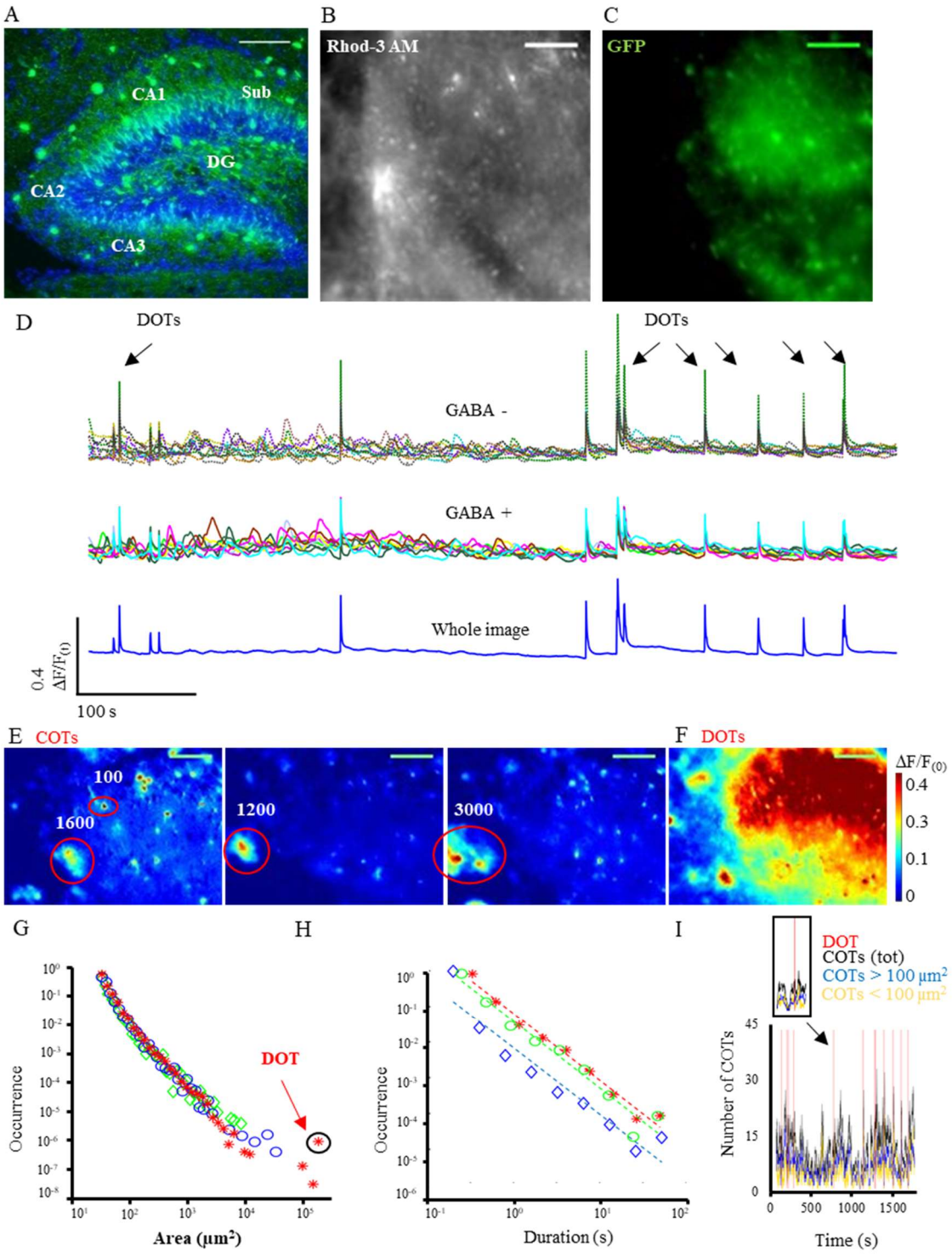


**Figure 4: Spontaneous events in the hippocampus. (A)** Fluorescent image of the hippocampus from a GAD67-GFP mouse (P5) with DAPI nuclear staining; GABA+ neurons are labeled in green. The anatomical regions corresponding to the cornu ammonis fields (CA1-3), subiculum (Sub) and dentate gyrus (DG) are shown. **(B)** Slice loaded with the fluorescent indicator Rhod -3 AM during calcium imaging and corresponding GABA+ neurons **(C)** in the same field of view. **(D)** $\Delta F/F_{(0)}$ traces extrapolated from the whole image (blue trace at the bottom), from GABA+ (colored traces in the middle) and GABA- neurons (colored traces on top). **(E)** Examples of Confined Optical Transients (COTs) from a pseudo-color $\Delta F/F_{(0)}$ movie, showing isolated regions of variable sizes (see red circles; the rounded numbers are expressed in $\mu m^2$). **(F)** example of a Diffuse Optical Transient (DOT), where the increase in $\Delta F/F_{network}$ involves more than 50% of the imaged slice. Color bar on the right. Scale bars: 80 µm in both fluorescence and pseudo-color images. **(G, H)** Probability distribution of area and duration of COTs in the hippocampus. Circles, rhombus and asterisks represent data

from three representative experiments: the corresponding dotted lines in (H) show the linear fitting for each distribution. DOTs are represented as resonances outside the area's distributions (see black circle). **(I)** Density of COTs over time for different area sizes (COTs<100 $\mu m^2$ and COTs>$\mu m^2$, yellow and blue lines respectively) and with reference to DOTs occurrence (red vertical lines). The inset shows the decrease in COTs density corresponding to DOTs' occurrence.

As COTs and DOTs were observed in both cortical and hippocampal slices, we asked whether it was possible to find starters also in hippocampal slices (see **Fig. 3**). Therefore, we analyzed optical recordings with tens of DOTs in a period of 20-40 minutes (**Fig. 5A**) and, in particular, the statistical properties of the seeds detected before DOTs occurrence (**Fig. 5B**). In the hippocampus, in contrast with what seen in cortical slices, the frequency of pixel activation was similar to a theoretical Binomial Distribution in 3 out of 5 experiments (**Fig. 5C, D**; $p>0.05$ two-sample Kolmogorov-Smirnof test). These results suggest that the existence of starters in hippocampal is less probable than in cortical slices, and the occurrence of a DOT in the hippocampus is more likely to originate when a sufficient number of neurons are activated.

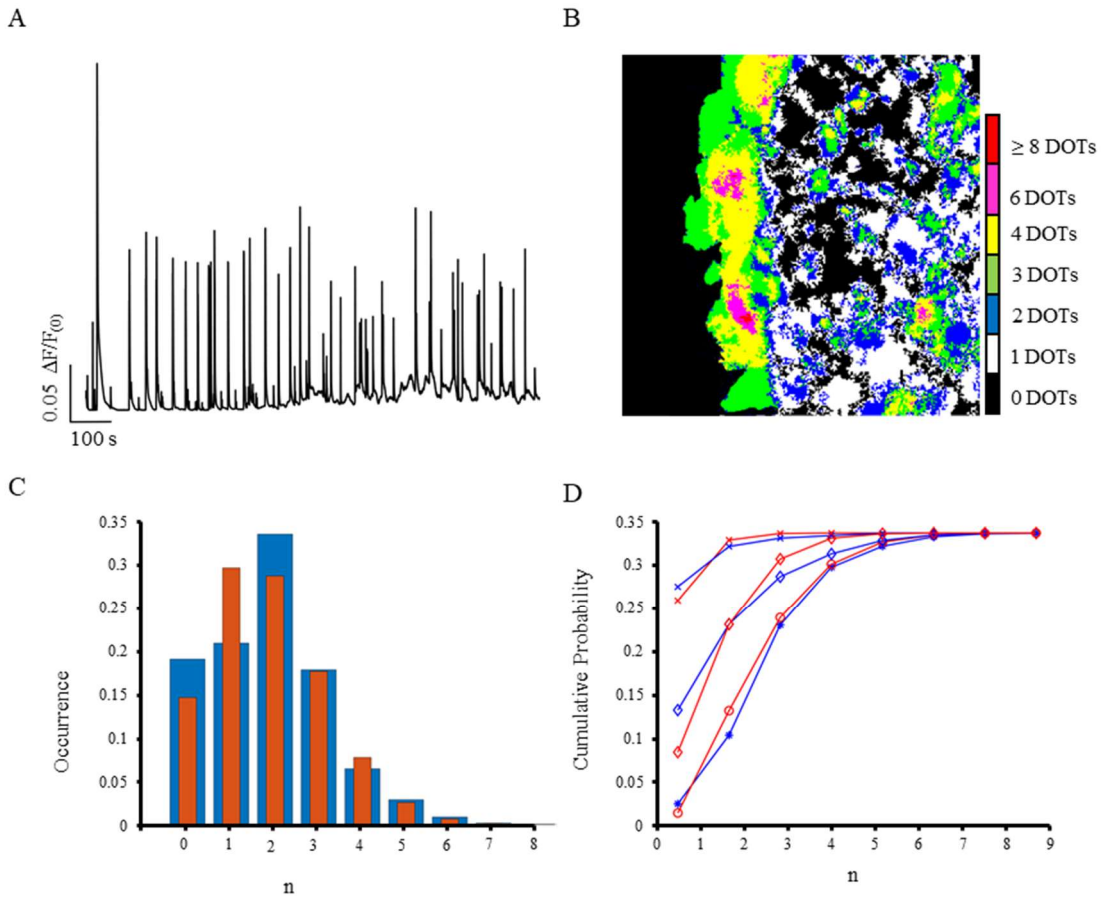


**Figure 5: Seeds of DOTs in hippocampal slices. (A)** Averaged optical trace of a representative 40 min recording. **(B)** Sum of all binary images corresponding to seeds; different colors indicate regions activated before multiple DOTs (see color bar on the right: red regions are activated before the onset of 8 or more DOTs). **(C)** Probability of activation of a pixel from experimental data compared to a binomial distribution in one experiment (blue and red bars, respectively). The x – axis represents the number of trials (frames) considered. **(D)** Cumulative probability of pixel activation from experimental data (blue lines) compared to the corresponding binomial distributions (red lines) in three representative experiments. n = 5 slices. The two distributions were not significantly different.

Comparing the distributions of area and duration of COTs in the cortex and hippocampus (**Fig. 6A, B**) and the corresponding power law's slopes (**Fig. 6C, D**), we did not observe significant differences.

In addition, very similar distributions and power law slopes of optical signals were obtained after mechanical truncation of the connections between hippocampus and cortex (see **Table 1**). We next analized the duration and frequency of DOTs separately, in 7 representative brain slices that showed a sufficient number of DOTs, and that we were able to record in the cortical and the hippocampal region for the same time (i.e. 10 min) without incurring into dye – and phototoxicity-driven tissue damage. The distribution of the duration of DOTs shows that they last longer in the cortex (**Fig. 6E**: 10.21 ± 0.32 s for cortex, 8.19 ± 0.43 s for hippocampus). On the other hand, the distribution of the Inter-DOTs- Intervals (IDI) shows that hippocampal DOTs are more frequent (**Fig. 6F**: 67.72 ± 4.88 s for cortex, 48.77 ± 6.23 s for hippocampus). These differences were statistically significant. Both distributions were fitted with appropriate exponential equations (see blue and red lines in **Fig. 6E, F**).

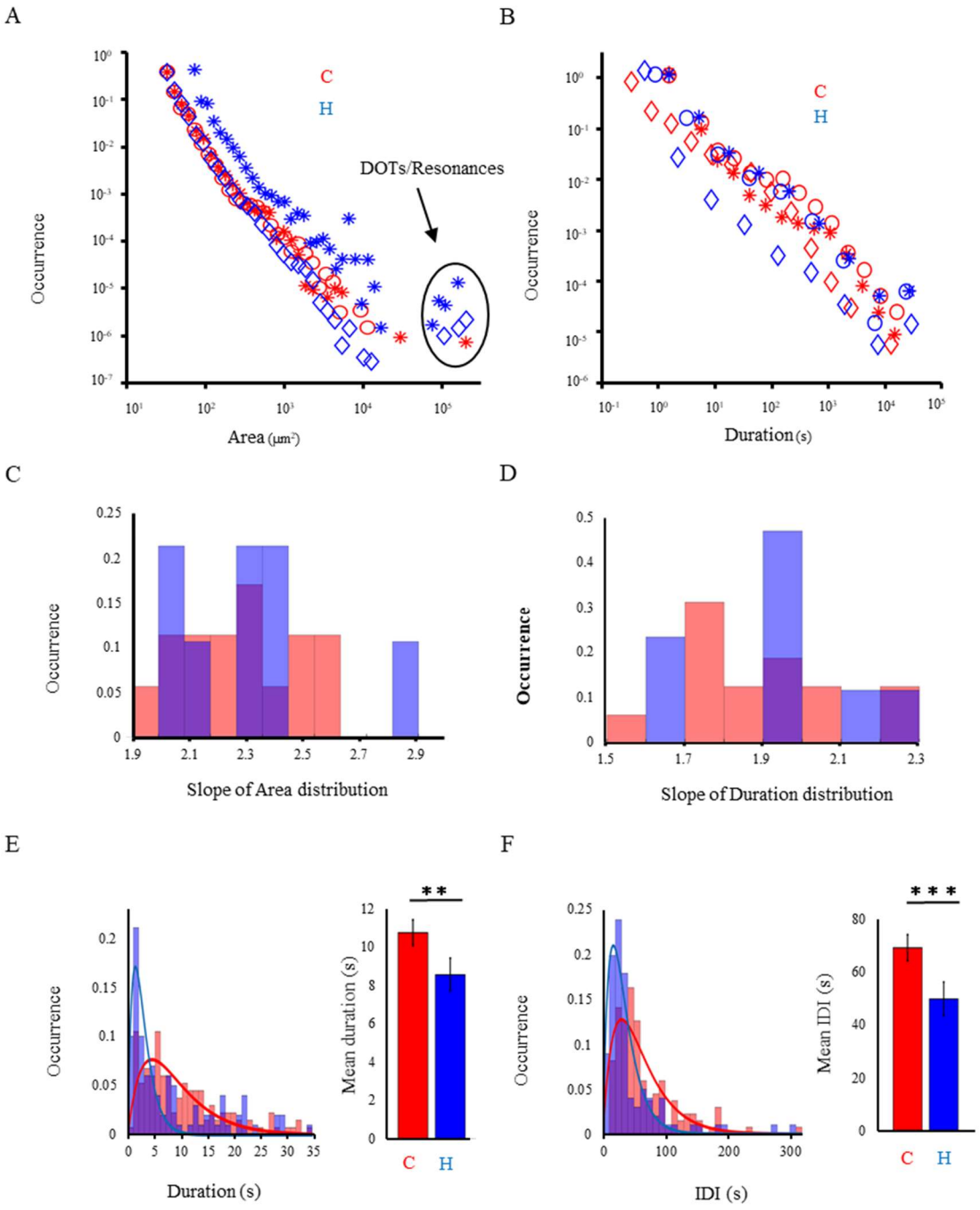


**Fig. 6. Dynamics of cortical and hippocampal events compared. (A, B)** Power law distribution of area and duration of COTs from three representative experiments (rhombus, circles and asterisks); cortical events are marked in red, while

hippocampal events are marked in blue. DOTs are represented as resonances outside the area's distributions (see black circle in A). **(C, D)** Probability distribution of power law slopes for area and duration in the cortex (red bars) and hippocampus (blue bars); n = 16 cortical recordings, n = 8 hippocampal recordings. **(E)** Distribution (left panel) and average values (right panel) of cortical (red bars) and hippocampal (blue bars) DOTs durations. The corresponding exponential fitting is **f(x)=0.05*x*exp(-x/4.54)** for the cortex, **f(x)=0.33*x*exp(-x/1.39)** for the hippocampus. **(F)** Distribution (left panel) and average values (right panel) of Inter – DOTs – Intervals (IDIs) in cortical (red bars) and hippocampal (blue bars) slices. The corresponding exponential fitting is **f(x)=0.011*x*exp(-x/33)** for the cortex, **f(x)=0.034*x*exp(-x/17)+0.58** for the hippocampus. n=102 cortical DOTs, n=137 hippocampal DOTs analyzed. $^{**}p < 0.01$, $^{***}p < 0.001$ Kruskal-Wallis test.

**Table 1: Average power laws slopes (binning = 42/12 for area/duration)**

| Conformation | Connected | Detached | Connected | Detached |
|---|---|---|---|---|
| | Area | | Duration | |
| Cortex | 2.24 ± 0.27 | 2.41 ± 0.56 | 1.87 ±0.22 | 1.88 ± 0.25 |
| Hippocampus | 2.28 ± 0.26 | 2.47 ± 0.34 | 1.94 ± 0.21 | 2.08 ± 0.26 |

Values are expressed as absolute values, mean ± standard deviation. n = 16/8 cortical/hippocampal recordings in connected tissues; n = 6/6 cortical/hippocampal recordings in detached condition.

### *3.4 Dissociated neuronal cultures*

The comparison of the spontaneous activity of the same neuronal population preserving the original cyto-architecture and after dissociation allows evaluating the role of the native connectivity. In dissociated cultures, formed by a single layer of cells, neuronal calcium transients have a typical sharp rising phase which is distinguished from those originating from glia cells (Charles *et al.*, 1991). Dissociated cell cultures are known to exhibit a degree of synchronization depending on the density of the culture (Ito *et al.*, 2010). In our experiments, we considered two culture density: 500/800 cells/mm$^2$ (medium density, MD; **Fig. 7A, B, E**) and 1000 cells/mm$^2$ or more (high density, HD; **Fig. 7C, D, F**). Figure 7 shows the results obtained from cortical cultures of GAD67-GFP mice, in which we could distinguish between GABA- and GABA+ neurons by comparing GFP-positive cells (**Fig. 7B, D**) to those stained with the calcium sensitive dye only (**Fig. 7A, C**), and separating the corresponding optical traces (**Fig. 7E, F**). GABA- and GABA+ neurons are representative, with a good approximation, of the excitatory and the inhibitory population respectively.

We found different degrees of synchrony among the peaks of calcium transients in MD and HD cultures. We computed the mean cross-correlation among pairs of neurons $\rho(t)_{Peak}$ in a time window of 1 sec and we found that $\rho(t)_{Peak}$ was higher in HD than in MD cultures (0.604 ± 0.002 vs 0.337 ± 0.002, **Fig. 7G**). However, in both cases the number of simultaneously active neurons over time showed periods of almost complete synchrony interspersed with epochs of very low coherent electrical activity (**Fig. 7H**). From these data, we computed the probability distribution of active neurons and found a power law behavior with slope -2 when the number of neurons were less than some tens (**Fig. 7I**). This distribution exhibited also resonances corresponding to the total number of neurons recorded that are very similar to those we referred as DOTs in slices (**Fig. 1G, 4G**). We obtained similar results from dissociated hippocampal cultures (see **Supplementary Fig. 3**, for review only, *ndr*). These results suggest that global events - here referred as Global Up states - are present both in native and in dissociated networks. A comparison of Global Up States in these different types of networks is shown in the **Discussion** section, **Fig. 10**. For this comparison, we used cortical slices cultured in the same medium (Neurobasal/B27) used for dissociated cells, in order to

avoid changes in neuronal synchronization due to the effect of different chemicals in the growing media (Pozzi *et al.*, 2017).

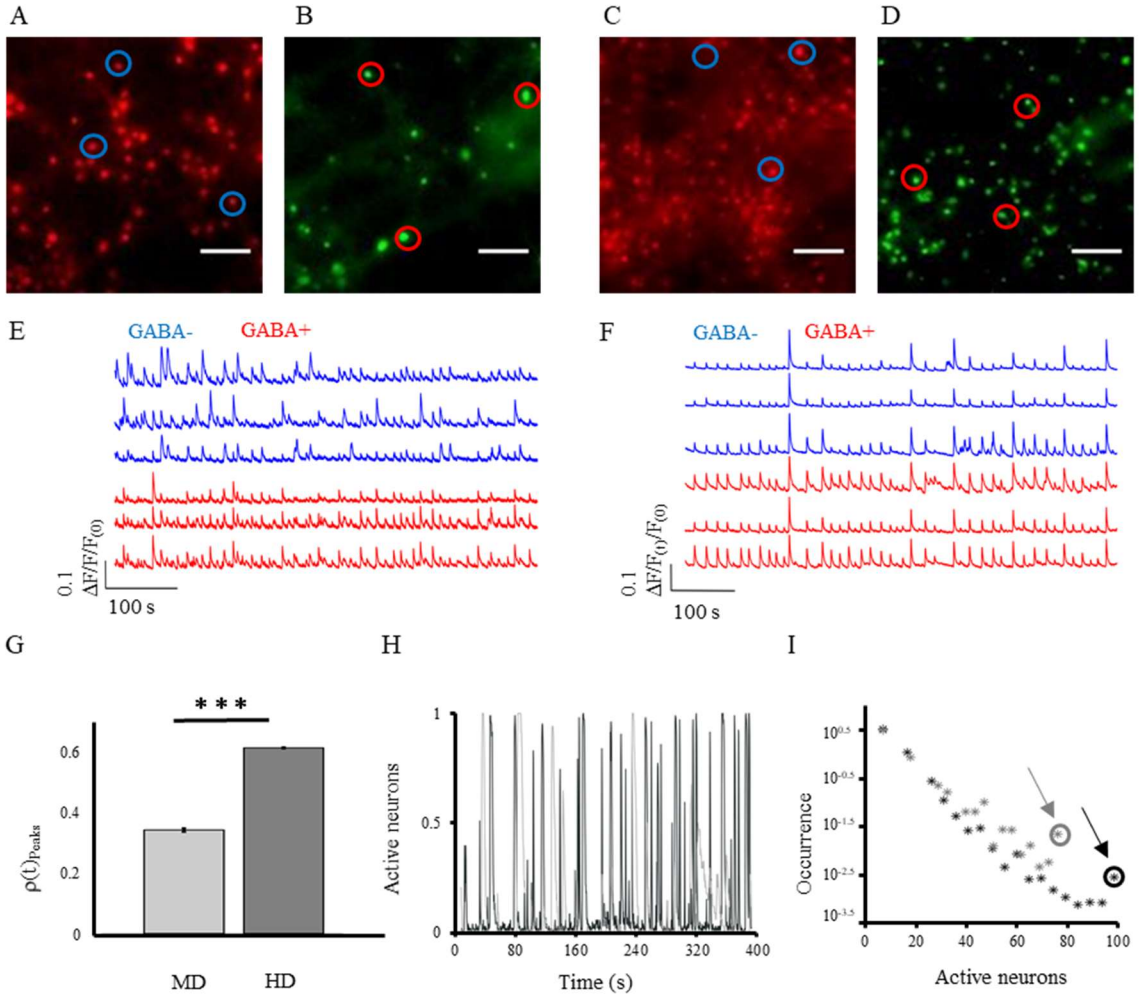


**Fig. 7. Dissociated cortical cultures plated at high (HD) and medium (MD) density. (A, C)** MD and HD cultures stained with Fura-Red calcium-sensitive dye. **(B, D)** Corresponding GABA+ neurons in the same field of view. From the neurons in the blue and red circles, the corresponding optical traces $\Delta F/F_{(0)}$ are shown in **(E, F)**: blue and red traces represent GABA- and GABA+ neurons respectively. **(G)** Average $\rho(t)_{Peak}$ in MD (light gray) and HD (dark gray) cultures; n = 9354(3) pairs of neurons(sample) for HD, n = 1211(3) pairs of neurons(sample) for MD. **(H)** Activation of neurons over time in MD (gray) and HD (black) cultures, normalized to the total number of neurons (105 and 34 for HD and MD cultures, in this representative experiment). **(I)** Probability distribution of the number of neurons simultaneously active in MD (gray marks) and HD (black marks) cultures, with corresponding resonances (see circles).

We found that an unequivocal distinction between GABA+ and GABA- neurons was possible only in dissociated MD cultures, in which neurons are not totally confluent. Thus, we compared calcium transients between GABA+ and GABA- neurons plated at a medium density and we found that the value of $\rho(t)_{Peak}$ - in a time window of 1 s - was higher in GABA+ than in GABA- neurons (**Fig. 8A**). We asked whether large calcium transients were more correlated than smaller transients (Ulloa Severino *et al.*, 2016) and indeed calcium transients larger than 30% of the maximal amplitude observed in each trace were more correlated than the smaller ones (**Fig. 8B**). After blockage of GABA-A receptors with 1 µM bicuculline, the amplitude of calcium transients became uniform in both populations (**Fig. 8C**), however both the rising and falling phase of these transients were slower. Therefore we compared $\rho(t)_{Peak}$ in a time window of 10 s, which was consistently higher in GABA+

neurons (**Fig. 8D**). The time interval between peaks was significantly lower in the GABA+ population (**Fig. 8E**), whereas the mean amplitude of $\Delta F/F_{(0)}$ was similar in GABA+ and GABA- neurons (**8F**). In order to identify possible delays in the transmission of excitatory and inhibitory signals, we repeated our imaging experiments using an acquisition rate of 50 Hz but we did not detect any consistent delay between GABA+ and GABA- neurons at the available temporal resolution of 20 msec. Our results suggest that inhibitory GABA+ neurons have more synchronized and frequent spontaneous activity, in agreement with previous observations (Gentet *et al.*, 2010).

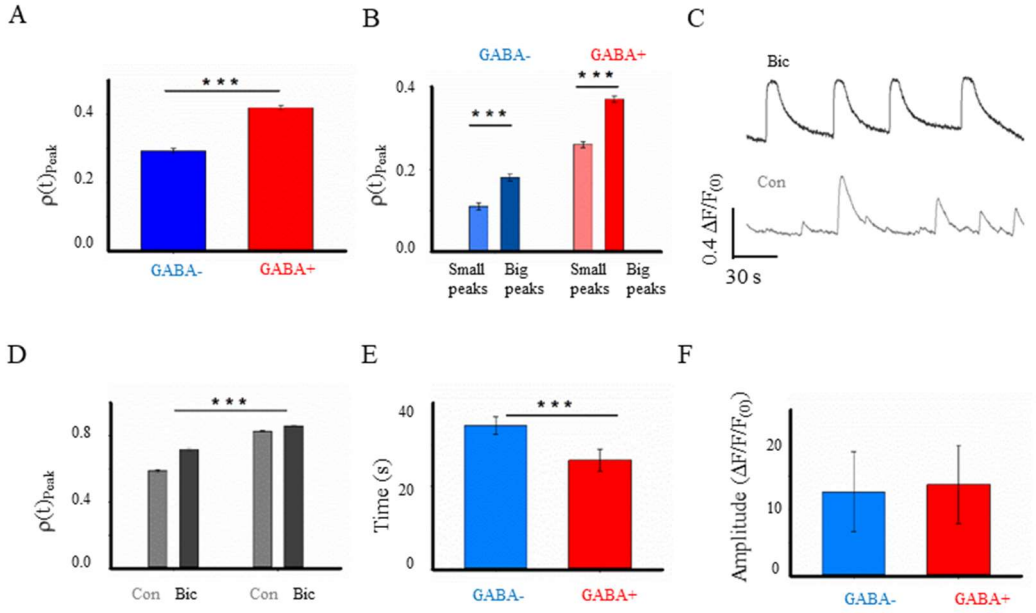


**Fig. 8. Calcium transients from dissociated GABA+ and GABA- neurons. (A)** Average $\rho(t)_{Peak}$, computed in 1 s time window, among pairs of GABA+ vs pairs of GABA- neurons in the network (0.42 ± 0.007 vs 0.294 ± 0.007, respectively). **(B)** Same as (A) distinguishing between small and big peaks (defined by a threshold equal to the 30% of the maximal amplitude observed in each trace: 0.37 ± 0.007 vs 0.181 ± 0.009 for GABA+ neurons; 0.263 ± 0.007 vs 0.110 ± 0.008 for GABA- neurons). n = 605(3) pairs of neurons(sample) for GABA+, n = 870(3) pairs of neurons(sample) for GABA-. **(C)** Representative $\Delta F/F_{(0)}$ traces in control and after application of bicuculline 1 µM. **(D)** Average $\rho(t)_{Peak}$ in control and after bicuculline application, in GABA+ and GABA- neurons, computed in a time window of 10 s (0.728 ± 0.006 and 0.865 ± 0.003 for GABA+ neurons in control and bicuculline conditions; 0.590 ± 0.007 and 0.828 ± 0.005 for GABA- neurons in control and bicuculline conditions ). **(E)** Average Inter Event Interval (s) between peaks of calcium transients in GABA+ and GABA- neurons (26.07 ± 2.13 vs 34.62 ± 2.62). **(F)** Average amplitude ($\Delta F/F_{(0)}$) in the two neuronal populations (0.14 ± 0.06 vs 0.13 ± 0.06). n = 73(3) neurons(sample) for GABA+, n = 105(3) neurons(sample) for GABA-). *** $p < 0.001$ One-Way ANOVA.

## 4. Discussion

Our results show that the spontaneous activity in cortical and hippocampal slices is dominated by the intermittency between a regime where optical signals are confined in several small regions (COTs, see **Fig. 1E, 4E**) and a regime where there is a global activation invading almost the entire visualized network (DOTs, see **Fig. 1F, 4F**), referred to as Global Up states. Global Up states appear as abrupt upward spikes when the overall emitted fluorescence $\Delta F/F_{network}$ is analyzed (**Fig. 1D, 4D**) and as a resonance when the distribution of maximal area of optical signals is computed (**Fig. 1G, 4G**). Global Up states were abolished by the application of TTX, powerfully reduced by APV and enhanced by Bicuculline (**Fig. 2**). In addition to this, they were longer and less frequent in the cortex (**Fig. 6E, F**) than in the hippocampus, and briefer when the original tissue was dissociated (**Fig. 7E, F**).

Taken together, these results show that resonances – i.e. Global Up states – are seen in all examined neuronal networks, in those preserving the original cyto-architecture and after dissociation of the native tissue as well. This observation suggests that the primary origin of resonances has to be found at the level of the biophysical properties of the neurons composing the network. Our results, however, demonstrate that the duration and intensity of the resonances depend on the original cyto-architecture of the cortex and of the hippocampus and on the overall balance between excitation and inhibition.

In order to understand the underlying mechanisms of the emergent dynamical properties, we explored highly simplified neural networks, which have just 2-4 free parameters (**Fig. 9**). These models are based on two major assumptions: firstly, dissociated neuronal cultures have a single layer organization, while cortical and hippocampal slices are multilayers; secondly some key factors, such as the threshold Vth and the number of connections per neurons NC, have a long-tailed distribution with a power law behavior (see **Methods** section). This approach is complementary to those developed in current large projects as the Blue Brain Project, Human Brain Project and Allen Brain Initiative where modelling involves an extremely large number of parameters, in the order $10^3 – 10^4$ times more than in our simplified models.

### *4.1 Simplified models of cortical, hippocampal and dissociated networks*

The power law behavior seen in the distribution of maximal areas and duration of spontaneous events is in agreement with the predictions of the theory of Self Organized Criticality (Bak *et al.*, 1987; Tang & Bak, 1988). This theory, however, assumes that the events under consideration are diluted in time and that only occasionally they occur simultaneously. Therefore, this central assumption of SOC does not hold for the optical transients observed in cortical and hippocampal slices, where we observed the simultaneous presence of tens of events at the same time (**Fig. 1I** and **Fig. 4I**).

The neural network we are considering consists of 1,…,*i*,…N neurons and each neuron *i* is connected to other NC neurons (**Fig. 9A** and **Methods** section). A unit of charge is injected into neuron i and is accumulated untill a threshold $V_{th}$ is reached and then the neuron *i* fires (**Fig. 9B**). The charge Q accumulated in each neuron is dissipated (decays) with a time constant λ. The charge Q in each neuron is injected randomly into each neuron *i* of the network and a random number of charges can also be injected at each time. These injected charges mimic random synaptic inputs received by the neurons present in the network. When the neuron *i* fires it either distributes the charge Q accumulated before reaching the threshold $V_{th}$ to all connected neurons (Model 1) or injects an equal and fixed fraction of its charge φ to all connected neurons (Model 2). Model 1 and Model 2 of a single layer network have just 3 and 4 free parameters, respectively: the threshold $V_{th}$, the degree of connectivity NC, the strength of connectivity φ (only in Model 2) and the rate of dissipation λ. The dissipation λ represents

all the biophysical processes reducing the excitation, such as the inhibitory inputs and all mechanisms associated to adaptation and desensitization. We have explored the behavior of Model 1 and 2 when these 3(4) parameters were varied, and when they were assumed random variables. We found that when $V_{th}$ is a random variable with a long tailed distribution, such as a power law of $\rho(V_{th}) = V_{th}^{-\alpha}$ ($\alpha < 2$), both Model 1 and Model 2 reproduce several of our experimental data. In fact, as experimentally observed (**Fig. 1** and **Fig. 4**), they reproduce a power law distribution of the number of simultaneously active neurons with a slope of about -2 (**Fig. 9C**). These models reproduce also the resonance corresponding to the experimentally observed DOTs, which is more pronounced in Model 1 than in Model 2 (see figure legend for more details). As we have a very limited number of parameters, we obtained state diagrams: in both models, resonances appear when NC increases and $\lambda$ decreases (**Fig. 9D**). In order to explore the possibility that some of the emergent dynamical properties of slices are due to their multilayer functional/anatomical organization, we constructed models of multilayer networks in which every neuron *i* has one connection to a neuron in the next layer (**Fig. 9E**). Increasing the number of layers, the duration and Inter DOT Intervals of the simulated DOTs increased (**Fig. 9F**).

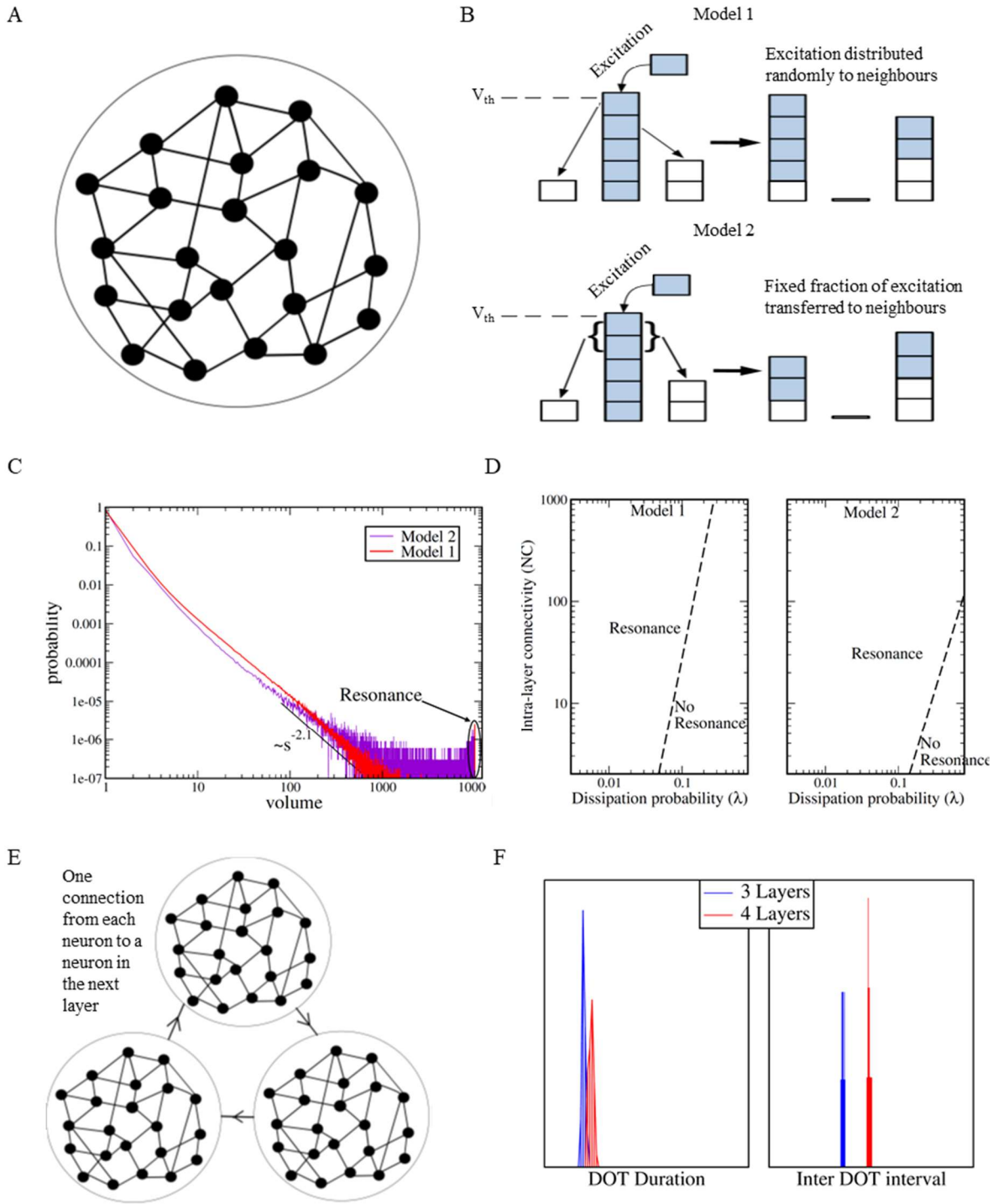


**Fig. 9. Simulation setup and results. (A)** Schematic diagram of the Single layer model of a network of N neurons with NC connections. **(B)** Schematic diagram of the mechanism of charge transfer in the two Models. **(C)** Distribution of avalanche volume for a network of N = 10,000 neurons in the two Models. **(D)** Phase diagram for the production of DOTs in terms of the dissipation and number of connections NC, for the two Models. The dashed line is indicative of the regime where DOTs disappear as one moves along either of the axis. **(E)** Schematic diagram of the multi-layer model. Each layer consists of N neurons with NC connections as before. However, now every neuron has one additional projection to the neurons in the next layer. **(F)** Distribution of DOT duration (defined in units of number of simultaneous DOTs in successive layers, which maps to number of DOTs times $\Delta\tau$) and inter-DOT interval (defined in units of number of perturbations, i.e., simulation time steps) in a multilayer model with 3 layers (blue bars) as compared to one with 4 layers (red bars).

We next compared the experimentally observed dynamical properties of native and dissociated networks with the corresponding simulated networks. The results are recapitulated in **Fig. 10** from the computation of optical traces $\Delta F/F_{network}$, and from the time series obtained with simulations. In both HD and MD cultures, $\Delta F/F_{network}$ has clear peaks but with a variable amplitude independently from the density of neurons (**Fig. 10A**). A similar variability was obtained simulating a single layer network with Model1 (**Fig. 10D**). Experimentally, in the presence of Bicuculline, the peaks of $\Delta F/F_{network}$ have a more similar amplitude (**Fig. 10B**), in line with the theoretical funding that decreasing $l$ enhances the probability of DOTs appearance (**Fig. 9D**, **10E**). In cortical slices, $\Delta F/F_{network}$ has less frequent peaks with a uniform amplitude and longer duration comparing to dissociated cultures (**Fig. 10C**) - a pattern that is reproduced by our multilayer network as shown in **Fig. 10F**. The DOTs experimentally observed in the cortex are longer than in the hippocampus (compare **Fig. 10G** and **H**) and have a specific time course during which the initial peak is followed by a longer plateau, with some oscillations not seen in dissociated cultures from the same tissue. This observation can be accounted by the presence of more anatomical/functional layers in cortical than hippocampal slices. Our models reproduce the occurrence of DOTs with a time course reminiscent of that seen in cortical slices (**Fig. 10I**).

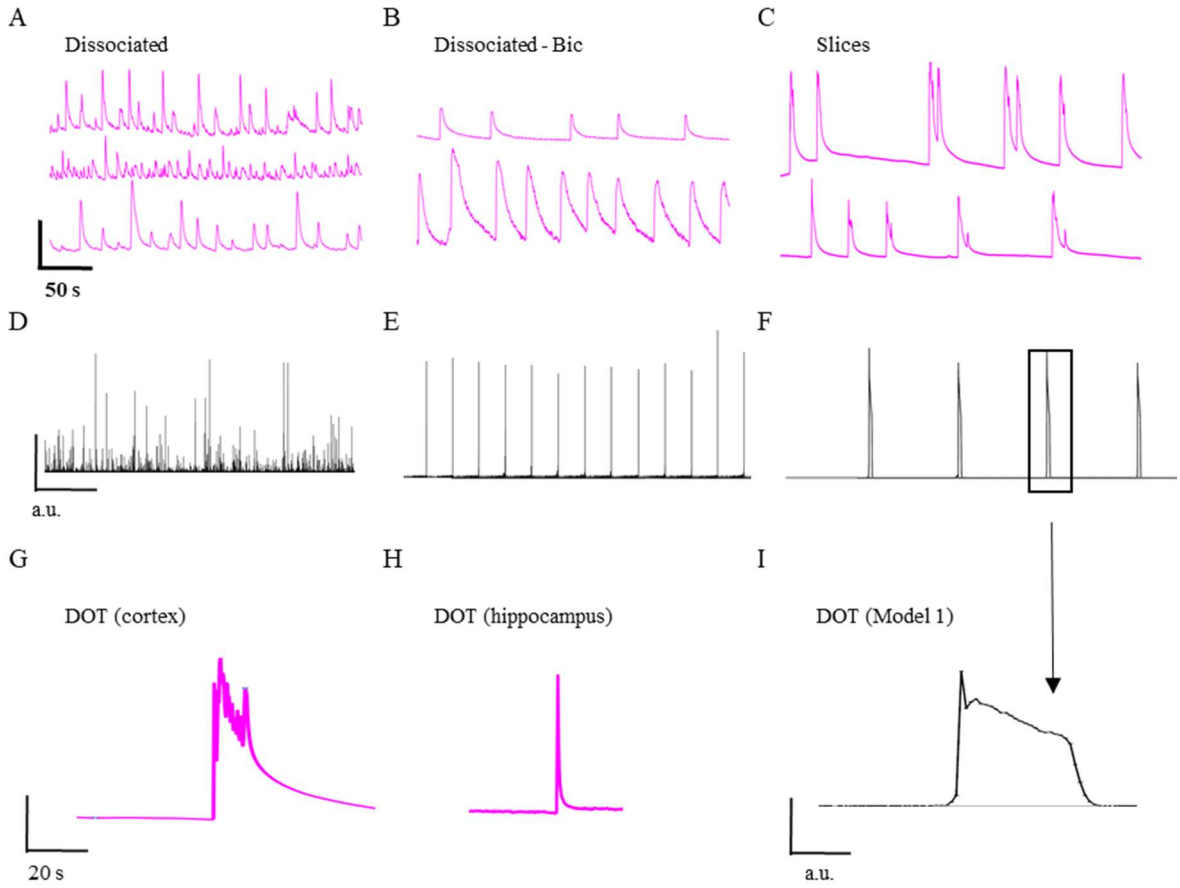


**Fig. 10. Intermittency in dissociated and native networks and corresponding simulations.** Experimental results are shown in purple, while time series obtained from the simulations are shown in black. **(A)** $\Delta F/F_{network}$ in dissociated MD/HD cultures. **(B)** $\Delta F/F_{network}$ in dissociated MD/HD cultures after application of Bicuculline 1 μM. **(C)** $\Delta F/F_{network}$ in some representative cortical slices. Scale bar, 0.1 $\Delta F/F_{network}$. **(D)** Time series of a single-layer network from Model1. **(E)** Time series from the same simulated network after decreasing λ. **(F)** Time series from a multilayer network from Model1. In these plots, the x-axis are in units of number of perturbations, i.e., simulation time steps Δτ (arbitrary units, a.u.). In the multilayer model, a Δτ of 50000 perturbation steps have been used. **(G, H)** Enlarged DOTs from $\Delta F/F_{network}$ of

experimental recordings in cortical and hippocampal slices, respectively. Scale bar, 0.1 $\Delta F/F_{network}$. **(I)** Enlarged Global event (DOT – like) from the simulation of the multilayer network.

The proposed modelling with simplified neural networks is based on the analysis of the interplay between different mechanisms at the basis of the dynamics of neural networks, such as the threshold $V_{th}$ for spike initiation, the degree of connectivity NC and the dissipation λ. Neurons in cortical and hippocampal networks experience a large amount of synaptic inputs leading to a fluctuation of their membrane potential (Hu & Bean, 2018). Therefore, in order to take these mechanisms into account, $V_{th}$ is not fixed and follows a power law distribution. Both fixed and power law distribution of NC, instead, produce similar results in our model. However, experimental results support long-tailed and lognormal distributions of NC and synaptic strength at the level of local circuits (see for review Schröter *et al.*, 2017). Our modelling introduces a rate of dissipation λ of the charge accumulated in each neuron which has been inspired by statistical mechanics approaches (Bak *et al.*, 1987; Marsili & Valleriani, 1998). This parameter is expected to describe in a lumped way some well-known mechanisms responsible for a time dependent decrease of the excitation, such as synaptic negative feedback, receptor desensitization and ionic channels inactivation.

In conclusion, the few parameters used in our models suffice to reproduce the observed intermittency and resonances at the single layer level. In particular, a resonance takes place when a neuron with a very high charge fires, thereby exciting its neighbours and triggering a global avalanche. These neurons are those present in the tail of the power law distribution of thresholds $V_{th}$. Moreover, resonances occur when a neuron highly connected to its neighbours fires: also in this case the neuron participates to the tail of the power law distribution of connectivity NC. Another important component required to observe resonance is the dissipation λ. If λ is high, it dissipates the excitation quickly and no resonance takes place. As opposite, if λ is weak, resonances occur. In order to obtain a broad peak of resonance like those seen in cortical/hippocampal slices, we need to introduce a multilayer architecture. The number of layers seems to determine the width and frequency of the resonances. We next explored an additional model where a firing neuron transfers not a fraction, but the same fixed amount of charge to its neighbours. In this way, the role of high threshold - neurons is eliminated. Also this model is in agreement with the experimental data. Therefore, we conclude that an interplay of these mechanisms together with the multilayer organization of the cortex and the hippocampus seem to be at the origin of their emergent collective properties.

### *4.2 Role of Global Up states in information processing in the nervous system*

It is well established that the spontaneous electrical activity represents the intrinsic noise with which the nervous system has to cope (Faisal *et al.*, 2008). The obvious question is whether and how Global Up states affect the efficiency of information processing in the brain. The present investigation clearly shows that the duration and the intensity of these Global Up states depend on the balance between excitation and inhibition as indicated by the action of APV – blocking NMDA glutamate receptors – and Bicuculine – blocking GABAergic receptors. Therefore, the nervous system has the means to control the duration and spatial spread of Global Up states.

Global Up states appear as strong and fast increase of $\Delta F/F_{network}$, in a way reminiscent of spike generation in a single neuron – that is triggered by a positive feedback due to the voltage-gated conductance. Thus, at the network level, Global Up states represent a positive feed-back which has been historically proposed to be a fundamental mechanism of information processing in the brain and to be at the basis of learning, memory and recognition (Fukushima, 1984; Rolls, 2016).

**References**


Bak P, Tang C & Wiesenfeld K (1987). Self-organized criticality: An explanation of the 1/f noise. *Phys Rev Lett* **59,** 381–384.

Buzsáki G (2002). Theta Oscillations in the Hippocampus. *Neuron* **33,** 325–340.

Charles AC, Merrill JE, Dirksen ER & Sanderson MJ (1991). Intercellular signaling in glial cells: calcium waves and oscillations in response to mechanical stimulation and glutamate. *Neuron* **6,** 983–992.

Compte A, Reig R, Descalzo VF, Harvey MA, Puccini GD & Sanchez-Vives MV (2008). Spontaneous High-Frequency (10-80 Hz) Oscillations during Up States in the Cerebral Cortex In Vitro. *J Neurosci* **28,** 13828–13844.

Cossart R, Aronov D & Yuste R (2003). Attractor dynamics of network UP states in the neocortex. *Nature* **423,** 283–288.

Cossart R, Ikegaya Y & Yuste R (2005). Calcium imaging of cortical networks dynamics. *Cell Calcium* **37,** 451–457.

Curto C, Sakata S, Marguet S, Itskov V & Harris KD (2009). A simple model of cortical dynamics explains variability and state dependence of sensory responses in urethane-anesthetized auditory cortex. *J Neurosci Off J Soc Neurosci* **29,** 10600–10612.

Douglas RJ & Martin KAC (2004). Neuronal circuits of the neocortex. *Annu Rev Neurosci* **27,** 419–451.

Engel TA, Steinmetz NA, Gieselmann MA, Thiele A, Moore T & Boahen K (2016). Selective modulation of cortical state during spatial attention. *Science* **354,** 1140–1144.

Faisal AA, Selen LPJ & Wolpert DM (2008). Noise in the nervous system. *Nat Rev Neurosci* **9,** 292–303.

Fanselow EE & Connors BW (2010). The roles of somatostatin-expressing (GIN) and fast-spiking inhibitory interneurons in UP-DOWN states of mouse neocortex. *J Neurophysiol* **104,** 596–606.

Fukushima K (1984). A hierarchical neural network model for associative memory. *Biol Cybern* **50,** 105–113.

Gähwiler BH, Capogna M, Debanne D, McKinney RA & Thompson SM (1997). Organotypic slice cultures: a technique has come of age. *Trends Neurosci* **20,** 471–477.

Garaschuk O, Linn J, Eilers J & Konnerth A (2000). Large-scale oscillatory calcium waves in the immature cortex. *Nat Neurosci* **3,** 452–459.

Gentet LJ, Avermann M, Matyas F, Staiger JF & Petersen CCH (2010). Membrane Potential Dynamics of GABAergic Neurons in the Barrel Cortex of Behaving Mice. *Neuron* **65,** 422–435.

Gilbride CJ (2016). The hyperexcitability of dentate granule neurons in organotypic hippocampal slice cultures is due to reorganization of synaptic inputs in vitro. *Physiol Rep* **4,** n/a-n/a.

Goodfellow M & Glendinning P (2013). Mechanisms of Intermittent State Transitions in a Coupled Heterogeneous Oscillator Model of Epilepsy. *J Math Neurosci* **3,** 17.

Hu W & Bean BP (2018). Differential Control of Axonal and Somatic Resting Potential by Voltage-Dependent Conductances in Cortical Layer 5 Pyramidal Neurons. *Neuron* **97,** 1315–1326.e3.

Ito D, Tamate H, Nagayama M, Uchida T, Kudoh SN & Gohara K (2010). Minimum neuron density for synchronized bursts in a rat cortical culture on multi-electrode arrays. *Neuroscience* **171,** 50–61.

Luczak A, Barthó P, Marguet SL, Buzsáki G & Harris KD (2007). Sequential structure of neocortical spontaneous activity in vivo. *Proc Natl Acad Sci U S A* **104,** 347–352.

Mao B-Q, Hamzei-Sichani F, Aronov D, Froemke RC & Yuste R (2001). Dynamics of Spontaneous Activity in Neocortical Slices. *Neuron* **32,** 883–898.

Markram H et al. (2015). Reconstruction and Simulation of Neocortical Microcircuitry. *Cell* **163,** 456–492.

Marsili M & Valleriani A (1998). Self Organization of Interacting Polya Urns. *Eur Phys J B* **3,** 417–420.

Mazzoni A, Broccard FD, Garcia-Perez E, Bonifazi P, Ruaro ME & Torre V (2007). On the Dynamics of the Spontaneous Activity in Neuronal Networks ed. Sporns O. *PLoS ONE* **2,** e439.

Narahashi T, Moore JW & Scott WR (1964). Tetrodotoxin Blockage of Sodium Conductance Increase in Lobster Giant Axons. *J Gen Physiol* **47,** 965–974.

Parga N & Abbott LF (2007). Network Model of Spontaneous Activity Exhibiting Synchronous Transitions Between Up and Down States. *Front Neurosci* **1,** 57–66.

Petersen CCH, Grinvald A & Sakmann B (2003). Spatiotemporal dynamics of sensory responses in layer 2/3 of rat barrel cortex measured in vivo by voltage-sensitive dye imaging combined with whole-cell voltage recordings and neuron reconstructions. *J Neurosci Off J Soc Neurosci* **23,** 1298–1309.

Piet R & Jahr CE (2007). Glutamatergic and Purinergic Receptor-Mediated Calcium Transients in Bergmann Glial Cells. *J Neurosci Off J Soc Neurosci* **27,** 4027–4035.

Pozzi D, Ban J, Iseppon F & Torre V (2017). An improved method for growing neurons: Comparison with standard protocols. *J Neurosci Methods* **280,** 1–10.

Regad T, Bellodi C, Nicotera P & Salomoni P (2009). The tumor suppressor Pml regulates cell fate in the developing neocortex. *Nat Neurosci* **12,** 132–140.

Rojas A, Wetherington J, Shaw R, Serrano G, Swanger S & Dingledine R (2013). Activation of Group I Metabotropic Glutamate Receptors Potentiates Heteromeric Kainate Receptors. *Mol Pharmacol* **83,** 106–121.

Rolls ET (2016). *Cerebral cortex: principles of operation*, First edition. Oxford University Press, Oxford New York, NY.

Sachidhanandam S, Sreenivasan V, Kyriakatos A, Kremer Y & Petersen CCH (2013). Membrane potential correlates of sensory perception in mouse barrel cortex. *Nat Neurosci* **16,** 1671–1677.

Sanchez-Vives MV & McCormick DA (2000). Cellular and network mechanisms of rhythmic recurrent activity in neocortex. *Nat Neurosci* **3,** 1027–1034.

Scarpetta S & de Candia A (2014). Alternation of up and down states at a dynamical phase-transition of a neural network with spatiotemporal attractors. *Front Syst Neurosci*; DOI: 10.3389/fnsys.2014.00088.

Schröter M, Paulsen O & Bullmore ET (2017). Micro-connectomics: probing the organization of neuronal networks at the cellular scale. *Nat Rev Neurosci* **18,** 131–146.

Sengupta M & Thirumalai V (2015). AMPA receptor mediated synaptic excitation drives state-dependent bursting in Purkinje neurons of zebrafish larvae. *eLife* **4,** e09158.

Sirota A & Buzsáki G (2005). Interaction between neocortical and hippocampal networks via slow oscillations. *Thalamus Relat Syst* **3,** 245.

Steriade M, Nuñez A & Amzica F (1993). A novel slow (< 1 Hz) oscillation of neocortical neurons in vivo: depolarizing and hyperpolarizing components. *J Neurosci Off J Soc Neurosci* **13,** 3252–3265.

Stoppini L, Buchs PA & Muller D (1991). A simple method for organotypic cultures of nervous tissue. *J Neurosci Methods* **37,** 173–182.

Tamamaki N, Yanagawa Y, Tomioka R, Miyazaki J-I, Obata K & Kaneko T (2003). Green fluorescent protein expression and colocalization with calretinin, parvalbumin, and somatostatin in the GAD67-GFP knock-in mouse. *J Comp Neurol* **467,** 60–79.

Tamura A, Yamada N, Yaguchi Y, Machida Y, Mori I & Osanai M (2014). Both Neurons and Astrocytes Exhibited Tetrodotoxin-Resistant Metabotropic Glutamate Receptor-Dependent Spontaneous Slow Ca2+ Oscillations in Striatum. *PLOS ONE* **9,** e85351.

Tang C & Bak P (1988). Critical Exponents and Scaling Relations for Self-Organized Critical Phenomena. *Phys Rev Lett* **60,** 2347–2350.

Timofeev I, Grenier F, Bazhenov M, Sejnowski TJ & Steriade M (2000). Origin of slow cortical oscillations in deafferented cortical slabs. *Cereb Cortex N Y N 1991* **10,** 1185–1199.

Timofeev I, Grenier F & Steriade M (2001). Disfacilitation and active inhibition in the neocortex during the natural sleep-wake cycle: an intracellular study. *Proc Natl Acad Sci U S A* **98,** 1924–1929.

Ulloa Severino FP, Ban J, Song Q, Tang M, Bianconi G, Cheng G & Torre V (2016). The role of dimensionality in neuronal network dynamics. *Sci Rep* **6,** 29640.

Vyazovskiy VV, Olcese U, Hanlon EC, Nir Y, Cirelli C & Tononi G (2011). Local sleep in awake rats. *Nature* **472,** 443–447.

Wadsworth GP & Bryan JG (1960). *Introduction to Probability and Random Variables*. McGraw-Hill.

Yang W, Miller J-EK, Carrillo-Reid L, Pnevmatikakis E, Paninski L, Yuste R & Peterka DS (2016). Simultaneous Multi-plane Imaging of Neural Circuits. *Neuron* **89,** 269–284.

Yang W & Yuste R (2017). In vivo imaging of neural activity. *Nat Methods* **14,** 349–359.

**Additional Information**

**Competing Interests**

Authors have no competing interests to declare.

**Author contributions**

DP designed experiments, acquired and analyzed data and drafted the article. BP prepared the brain slices for imaging experiments. NM and AM developed the algorithms for image processing and data analysis. AR and MM developed the simulations models. VT conceived experiments, interpreted data and drafted the article.

**Funding**

This work was supported by the 3315 project of Ningbo Institute of Materials Technology and Engineering, Chinese Academy of Sciences, Zhejiang province (China).

**Acknowledgements**

The authors would like to thank Prof. Michele Giugliano and Dr Paolo Bonifazi for their useful comments on the early version of the manuscript.

**Supporting Information**

Supplementary video available online:

**Supplementary Video 1. Calcium imaging recording from cortical slices.** Acquisition rate: 3 Hz. The video plays at increased speed (10x). Scale bar, 80 μm.

**Supplementary Video 2**. **Pseudo-color video reconstruction of $\Delta F/F_{network}$.** From the original Supplementary Video 1 (see color map in **Fig. 1E**). Scale bar, 80 μm.

**Supplementary Video 3**. **Calcium imaging recording from hippocampal slices**. Acquisition rate: 10 Hz. The video plays at increased speed (10x). Scale bar, 80 μm.

**Supplementary Video 4**. **Pseudo-color video reconstruction of $\Delta F/F_{network}$.** From the original Supplementary Video 3 (see color map in **Fig. 4E**). Scale bar, 80 μm.